ENHANCING THE PERFORMANCE OF HIGHLY FILLED POLYMER-BONDED Nd–Fe–B MAGNETS: INTEGRATED ADVANCED SURFACE TREATMENTS AND ADDITIVE MANUFACTURING

Ana Damnjanović

Doctoral Dissertation
Jožef Stefan International Postgraduate School
Ljubljana, Slovenia

Supervisor: Prof. Dr. Ingrid Milošev, Jožef Stefan International Postgraduate School and Jožef Stefan Institute, Ljubljana, Slovenia
Industrial Co-Supervisor: Dr. Nataša Kovačević, Kolektor Mobility d.o.o., Idrija, Slovenia

Evaluation Board:
Asst. Prof. Dr. Peter Rodič, Chair, Jožef Stefan International Postgraduate School and Jožef Stefan Institute, Ljubljana, Slovenia
Prof. Dr. Boštjan Markoli, Member, Faculty of Natural Sciences and Engineering, University of Ljubljana, Ljubljana, Slovenia
Prof. Dr. Spomenka Kobe, Member, Jožef Stefan International Postgraduate School and Jožef Stefan Institute, Ljubljana, Slovenia

MEDNARODNA PODIPLOMSKA ŠOLA JOŽEFA STEFANA
JOŽEF STEFAN INTERNATIONAL POSTGRADUATE SCHOOL

Ana Damnjanović

ENHANCING THE PERFORMANCE OF HIGHLY FILLED POLYMER-BONDED Nd–Fe–B MAGNETS: INTEGRATED ADVANCED SURFACE TREATMENTS AND ADDITIVE MANUFACTURING

Doctoral Dissertation

IZBOLJŠANJE ZMOGLJIVOSTI MOČNO NAPOLNJENIH POLIMERNO VEZANIH Nd–Fe–B MAGNETOV: INTEGRIRANE NAPREDNE POVRŠINSKE OBDELAVE IN ADITIVNA PROIZVODNJA

Doktorska disertacija

Supervisor: Prof. Dr. Ingrid Milošev

Industrial Co-Supervisor: Dr. Nataša Kovačević

Ljubljana, Slovenia, September 2024

To my family and friends

Acknowledgments

I would like to thank to the European Commission for supporting the research presented in this thesis with the Marie Skłodowska-Curie Actions (MSCA) Innovative Training Network (ITN) in the MaMi project – Magnetics and Microhydrodynamics (H2020 grant agreement No. 766007).

I am deeply grateful to my thesis supervisor, Prof. Dr. Ingrid Milošev, and my co-supervisor, Dr. Nataša Kovačević, for their invaluable guidance and support I got during my studies. Their insight and mentorship were crucial to the successful completion of this work.

I want to thank the members of the evaluation board: Prof. Dr. Spomenka Kobe, Prof. Dr. Boštjan Markoli, and Doc. Dr. Peter Rodič, for reviewing the manuscript and evaluating my thesis.

The research work for this thesis was conducted at Kolektor Mobility d.o.o., and I am extremely grateful to all its employees for providing me with assistance when needed. I am especially thankful to Dr. Boris Saje for our fruitful discussions, which greatly enriched my work. I would also like to thank my former colleagues, particularly Nevenka Rajnar, Rok Šinkovec, and Ana Dremelj, for making my time at Kolektor Mobility both educational and enjoyable.

My sincere thanks go to the staff at the K7 and K4 departments of the Jožef Stefan Institute for granting me access to analytical tools and labs when needed. Special thanks to Prof. Miran Mozetič, Dr. Gregor Primc, and Dr. Rok Zaplotnik from the F4 department for their invaluable help and assistance with plasma modifications and collaboration.

I would also like to acknowledge my high school English teacher, Sunčana Tadić. Without her dedication and teaching, my ability to pursue studies abroad and communicate effectively would not have been possible.

A heartfelt thank you to my parents and my family for their unshakeable support and for imparting strong values that have shaped who I am today.

To my friends, both near and far, thank you for your encouragement: Dunja, Martina, and Kiran for your remote support, and my Slovenia-based friends Dejana, Marija, Legro, Tamara, James, Zvezdan, Nebojša, and Kamel for being there during the emotional highs and lows of this PhD journey, and for always inspiring me to push forward.

Last but certainly not least, I would like to thank myself for working hard to reach this point.

Abstract

This doctoral dissertation present research aimed into enhancing polymer-bonded Nd–Fe–B magnets through innovative surface treatments and additive manufacturing techniques, focusing on improving their mechanical strength, magnetic characteristics, and environmental stability. This research is critical for broadening the applicability of these magnets in sectors like green technologies and motion control systems. The dissertation presents findings from three pivotal studies, each addressing different aspects of magnet production and treatment.

The first study explores surface modifications using a sequence of phosphatisation, tetraethyl orthosilicate (TEOS), and 3-aminopropyltriethoxysilane (APTES). This treatment significantly improved the mechanical properties and corrosion resistance of the magnets. Magnets subjected to these modifications showed enhancements in tensile strength by 62%, elongation at the break by 16.7%, and an elastic modulus increase of 19.9%. They also exhibited a remarkable corrosion resistance with less than 5% flux loss after exposure to harsh conditions.

The second study investigated the use of fused deposition modelling (FDM) for manufacturing polymer-bonded magnets with both melt-spun and gas-atomized Nd—Fe—B powders. It was found that using gas-atomized powders, which facilitated better flow and lower porosity, significantly improved the quality of printed magnets. These magnets demonstrated higher densities and enhanced magnetic properties with a remanence (B_r) of 426 mT, coercivity (H_{ci}) of 721 kA/m, and an energy product (BH_{max}) of 29 kJ/m^3, compared to their melt-spun counterparts. Additionally, these FDM-printed magnets exhibited excellent thermal stability and corrosion resistance, maintaining performance integrity after prolonged exposure to 85°C in air and water.

The third study details the application of plasma treatments to enhance the interface adhesion between Nd–Fe–B magnetic powders and the polymer matrix within FDM-printed magnets. The application of both radio frequency and low-pressure microwave plasma treatments significantly enhanced the mechanical properties and environmental stability of the magnets. Results showed that plasma-treated magnets achieved high densities (92-94% of theoretical values), optimal mechanical profiles with elastic modulus up to 578 MPa, and the highest ductility at 21%. The flexural strength reached up to 15 MPa with minimal flux loss, confirming the effectiveness of plasma treatments in maintaining the magnet's integrity under various conditions.

Together, these studies validate the dissertation's hypotheses and demonstrate that specialized surface treatments and additive manufacturing adjustments can substantially enhance the performance of Nd—Fe—B polymer-bonded magnets. The findings contribute to both the academic research and practical applications, promoting more sustainable and efficient use of rare earth magnets and fostering broader applications in essential technological fields.

Povzetek

Ta doktorska disertacija predstavlja raziskave, usmerjene v izboljšanje polimerno vezanih Nd– Fe–B magnetov z inovativnimi površinskimi obdelavami in tehnikami aditivne proizvodnje, s poudarkom na izboljšanju njihove mehanske trdnosti, magnetnih lastnosti in okoljske stabilnosti. Raziskava je ključnega pomena za širitev uporabnosti teh magnetov v sektorjih, kot so zelene tehnologije in sistemi za nadzor gibanja. Disertacija predstavlja ugotovitve iz treh ključnih študij, od katerih vsaka obravnava različne vidike proizvodnje in obdelave magnetov.

Prva študija raziskuje površinske modifikacije z uporabo fosfatizacije in nanosa tetraetil ortosilikata (TEOS) in 3-aminopropiltrietoksisilana (APTES). Ta obdelava je znatno izboljšala mehanske lastnosti in odpornost magnetov proti koroziji. Magneti, ki so bili podvrženi tem modifikacijam, so pokazali izboljšanje natezne trdnosti za 62 %, raztezka pri prelomu za 16.7 % in povečanje elastičnega modula za 19.9 %. Prav tako so izkazali izjemno odpornost proti koroziji, saj so izgubili manj kot 5 % magnetnega pretoka po izpostavitvi zahtevnim pogojem.

Druga študija je raziskovala uporabo modeliranja s taljenjem (3D tisk) za proizvodnjo polimerno vezanih magnetov z uporabo hitro ohlajenih in plinsko atomiziranih Nd−Fe−B prahov. Ugotovljeno je bilo, da uporaba plinsko atomiziranih prahov, ki so omogočali boljši pretok in manjšo poroznost, bistveno izboljša kakovost natisnjenih magnetov. Ti magneti so dosegli večje gostote in izboljšane magnetne lastnosti, z remanenco (B_r) 426 mT, koercitivnostjo (H_{ci}) 721 kA/m in energijskim produktom (BH_{max}) 29 kJ/m^3, v primerjavi z njihovimi hitro ohlajenimi različicami. Poleg tega so ti 3D-natisnjeni magneti izkazali odlično toplotno stabilnost in odpornost proti koroziji, saj so ohranili celovitost zmogljivosti po dolgotrajni izpostavljenosti 85 °C v zraku in vodi.

Tretja študija podrobno opisuje uporabo plazemskih obdelav za izboljšanje adhezije med Nd–Fe–B magnetnimi praški in polimerno matrico znotraj FDM-natisnjenih magnetov. Uporaba radiofrekvenčnih in nizkotlačnih mikrovalovnih plazemskih obdelav je znatno izboljšala mehanske lastnosti in okoljsko stabilnost magnetov. Rezultati so pokazali, da so plazemsko obdelani magneti dosegli visoke gostote (92–94 % teoretičnih vrednosti), optimalne mehanske profile z elastičnim modulom do 578 MPa in najvišjo duktilnost pri 21 %. Upogibna trdnost je dosegla do 15 MPa z minimalno izgubo magnetnega pretoka, kar potrjuje učinkovitost plazemskih obdelav pri ohranjanju celovitosti magnetov v različnih pogojih.

Te študije skupaj potrjujejo hipoteze disertacije in dokazujejo, da lahko specializirane površinske obdelave in prilagoditve aditivne proizvodnje bistveno izboljšajo zmogljivost polimerno vezanih Nd−Fe−B magnetov. Ugotovitve prispevajo k področju akademske raziskave in praktični uporabi, saj spodbujajo bolj trajnostno in učinkovito uporabo magnetov iz redkih zemelj ter omogočajo širšo uporabo na ključnih tehnoloških področjih.

Contents

List of Figures

List of Tables

Abbreviations

AM ... additive manufacturing
APTES ... 3-aminopropyltriethoxysilane
BCT ... bulk corrosion test
CLIP ... continuous liquid interface production
DI ... deionized water
DLP ... digital light processing
DSC ... differential scanning calorimetry
EDX ... energy dispersive X-ray spectroscopy
EVs ... electric vehicles
FDM ... fused deposition modelling
FTIR ... Fourier-transform infrared spectroscopy
IM ... injection moulded
IPA ... isopropyl alcohol
MFI ... melt flow index
MW ... microwave
PBF ... powder bed fusion
PM ... permanent magnet
PPS ... polyphenylene sulphide
RF ... radio-frequency
SEM ... scanning electron microscopy
SLA ... stereolithography
TEOS ... tetraethyl orthosilicate
TGA ... thermogravimetric analysis
UV ... ultraviolet light

Symbols

BH_{max} . . . maximum energy product
B_r . . . residual remanence
H_c . . . enthalpy after the cooling cycle
H_{ci} . . . coercivity
T_c . . . cold crystallisation temperature
T_{m1} . . . temperature after first heating
T_{m2} . . . temperature after second heating
w_f . . . weight fraction of filler
X_c . . . degree of crystallinity
ΔH_0 . . . melting enthalpy of 100% crystalline PA12
ΔH_m . . . melting enthalpy
ΔH_{m1} . . . enthalpy after first heating
ΔH_{m2} . . . enthalpy after second heating

Chapter 1

Introduction

1.1 Permanent Magnets: Background and Historical Perspectives

The journey of permanent magnets (PM) from natural lodestones to highly engineered materials spans centuries of discovery and innovation. The earliest known magnets, naturally magnetized stones known as lodestones, were utilized by ancient navigators for navigation. This early use of magnetic materials laid the foundation for profound explorations into magnetic phenomena, catalysing significant discoveries and advancements over the centuries [1].

The first half of the 1900s marked a significant advancement with the development of Alnico (aluminium, nickel, cobalt) magnets. The technological evolution of magnets began in 1917 with the development of KS steel (Kichizaemon Sumitomo steel), an iron alloy that included cobalt, tungsten, chromium, and carbon. Known for its strong magnetic properties, KS steel marked a significant advancement in magnetic technology. This was followed by the introduction of MK steel (Mischmetall-Kobalt steel) in 1932, a variant without carbon composed of iron, nickel, and aluminium. This alloy was further enhanced to create New KS steel by adding cobalt, titanium, and copper [2].

During the same period, the introduction of ferrite magnets, specifically OP magnets (orthoferrite permanent magnets) made from cobalt ferrite and iron ferrite, marked a shift towards materials offering good magnetic capabilities with improved corrosion resistance and lower costs. This innovation continued into 1952 with the development of barium ferrite magnets, which later evolved into strontium ferrite magnets [3].

Within second half of the 20th century, we have seen a revolution in magnetic materials with the discovery of rare-earth magnets. The era of samarium cobalt ($Sm_{C}o_{5}$ and $SmCo_{17}$) magnets started in the 1960s. More research was encouraged into intermetallic compounds of rare earth elements and iron due to the cobalt crisis of the 1970s, culminating in the 1980s with the groundbreaking discovery of neodymium-iron-boron magnets, Nd–Fe–B. These magnets were developed independently and almost simultaneously in Japan and the USA via different manufacturing routes—pressing and sintering in Japan and melt-spinning in the USA. The exceptional magnetic properties of Nd–Fe–B magnets significantly contributed to the miniaturisation and development of various technologies, making them invaluable in numerous high-demand applications today [4]. Despite these advancements, challenges such as susceptibility to corrosion and high production costs continued to drive research. In 1987, samarium-iron-nitride, $Sm_2Fe_{17}N_3$ was developed [5], although it declined in popularity due to difficulties in producing high-performance sintered magnets.

This historical perspective gives evidence of technological advancements and lays a basic understanding for the challenges and continuous need for innovations in magnet manufacturing. This development underlines the importance of continuous innovation in material science, particularly in enhancing the properties of Nd–Fe–B magnets through advanced manufacturing and surface treatment techniques.

1.2 Importance and Applications of Permanent Magnets

The key trait of permanent magnets is their ability to retain a constant magnetic field without needing an external power source. For these magnets to be effective in modern applications, they must meet several essential criteria. First, they need to produce a strong magnetic field, which is measured by three important values: magnetic remanence (B_r), coercivity (H_{ci}), and maximum energy product (BH_{max}). High B_r is the magnetic strength the magnet holds when in a closed circuit. A higher Br value indicates a stronger magnet capable of generating powerful magnetic fields. H_{ci} measures the resistance of a ferromagnetic material to becoming demagnetized. Nd–Fe–B magnets are highly resistant to demagnetisation, making them ideal for applications involving high temperatures or external magnetic fields that could otherwise demagnetize weaker materials. BH_{max} is the maximum energy density that the magnet can provide. Nd–Fe–B magnets offer the highest BH_{max} among all permanent magnets, which translates into superior performance in a smaller, lighter package. Another key property is that good permanent magnets must withstand high temperatures and resist demagnetisation due to external magnetic fields. This is often indicated by a high Curie temperature, Tc, and resistance to oxidation and rusting, ensuring longevity and functionality under various environmental conditions. To ensure cost-effectivness, magnets must provide strong magnetic energy at a reasonable cost. Nd–Fe–B magnets are the strongest permanent magnets available and can be produced in both isotropic and anisotropic forms. Isotropic magnets can be magnetized in any direction, which can provide flexibility in design but generally offers lower magnetic energy than anisotropic magnets. Anisotropic magnets are aligned during manufacturing to maximize magnetic strength in a specific direction. This orientation increases the magnetic force but limits the magnetisation direction to one aligned with the grain of the material, which is optimal for specific, high-performance applications. More detailed explanations of these key parameters can be found in the literature, simplifying the complex technical descriptions for broader understanding [6], [7].

The focus of this thesis, particularly in the introductory chapters, will predominantly be on Nd–Fe–B magnets, which are a critical component in generators and motors for wind turbines and electric vehicles (EVs). Market forecasts by Roskill suggest that by 2030, rare earth magnet applications will account for about 40% of total demand, potentially leading to a tight supply-demand scenario and spurring the development of new production capacities [8]. They are primarily used in electric motors, which convert electrical energy into mechanical motion. This application benefits from the magnet's high energy efficiency and reliability performance contributing to the overall effectiveness and environmental sustainability of EVs [9]. Nd–Fe–B magnets are also crucial in renewable energy generation, especially in wind turbines, where they are used in the generators to convert wind's kinetic energy into electrical energy. The generator's rotor creates a rotating magnetic field, inducing electric energy into the stator windings. This magnetic field can be generated by electromagnets, requiring electrical excitation and consuming reactive power, or by PM, which does not require electrical excitation [10]. Their high energy product allows for the creation of more compact and efficient generators, which improves the output and

reliability of wind energy systems. Additionally, rare-earth-based permanent magnets such as samarium-cobalt and neodymium-iron-boron are extensively utilized in advanced military applications such as navigation systems in battlefield tanks and electronic warfare equipment due to their stability under extreme conditions [11].

These applications demonstrate the critical role that Nd–Fe–B magnets play in modern technology, driving advancements that touch nearly every aspect of contemporary life. By understanding and optimizing the unique properties of these magnets, industries can enhance the performance and efficiency of a wide range of devices and systems.

1.3 Production Methods for Permanent Magnets and Their Challenges

Permanent magnets are produced through several methods, each with its advantages and disadvantages. Manufacturing techniques are continuously improved with advancing technology by offering improved performance and opening new perspectives in finding innovative applications.

Sintering is still most widely used method to manufacture full-density, high-performance Nd–Fe–B magnets. The process begins with preparing an alloy using the strip-casting method, which is then converted into a fine powder through hydrogen decrepitation and jet-milling. This fine powder, consisting of single-crystal particles of the $Nd_2Fe_{14}B$ phase, is compacted into moulds under an applied magnetic field to orient the particles. The compacted green body is then sintered in a vacuum furnace at approximately 1100 °C, which allows the particles to fuse, creating a dense and robust magnet. Post-sintering heat treatment is performed to develop the full coercivity, and the magnets are machined to the desired shape and coated for protection [12]. The advantages of sintering process are producing magnets with high magnetic performance, creating complex shapes and sizes, and achieving high density. On the other hand, this technique also possesses drawbacks such as requiring high temperature with controlled atmospheres, which means high energy consumption processes. Impurities affecting the performance of a magnet are also sensitive to the process. In some cases, this may involve machining after processing, further adding cost and complexity. Despite these challenges, sintered Nd–Fe–B magnets are well suited for high-performance applications such as electric vehicles, wind turbines, and industrial motors, making sintering the most established but also the most resource-intensive and expensive route of production.

Moulding of Nd–Fe–B permanent magnets involve mixing Nd–Fe–B powder with a polymer binder, such as polyamides (nylon) or polyphenylene sulphide (PPS). These are then pressed or injected into a mould. Feedstock material in the form of magnetic powders, polymers, and additives, are kneaded in extruders and shaped into pellets of a few millimetres in size. Prior to the pellets feeding into the injection moulding machine, they must be dried to a specific moisture level to ensure the quality of the final magnet. Depending on desired properties and final applications, various polymers can be utilised as binders. Commonly used binders include polyamides, however maximum operating temperatures of polyamides is limited between 120 °C and 130 °C, beyond which they may suffer from oxidation or mechanical softening. However, PPS, can withstand higher temperatures up to 200 °C, making it suitable for more demanding applications [13]. The mould temperature during injection moulding may change between 250 °C and 340 °C according to the type of used polymer and mould design. Therefore, this technique allows the manufacturing of magnets with complicated shapes, including thin walls, suitable for complex geometries applications like sensors, small motors, and consumer electronics.

Injection-moulded magnets generally have lower magnetic performance due to the dilution effect of the binder, resulting in reduced mechanical strength and thermal stability, they are highly competitive due to their ability to produce diverse field distributions and complex shapes [14]. In the automotive industry, injection-moulded Nd–Fe–B magnets are particularly valuable. They are used extensively in magnetic sensors and electrical machines, which control nearly all moving units in modern cars. Applications include window lifters, seat positioning units, torque and rotation sensors for electrical steering systems, windshield wipers, and many other components. The ability to integrate these magnets easily with other parts through over-moulding or multi-component moulding enhances their utility and reliability in automotive applications. The demand for these magnets is growing rapidly in the automotive sector due to their efficiency and the increasing complexity of modern vehicles.

Additive manufacturing (AM), or 3D printing, a key component of Industry 4.0, rapidly expands across various high-tech sectors, including green technologies, aerospace, and medicine. Driving force for growing interest in AM is its ability to enable customized production and create complex geometries, resulting in lighter parts crucial for reducing fuel consumption and carbon emissions in automotive applications. Additionally, AM minimizes material wastage, which economically benefits expensive materials like rare earth magnetic powders [15]. Initially focused on rapid and cost-effective prototype fabrication, AM is advancing towards serial production. Despite its origins in the 1980s, AM continues to evolve as diverse material groups, such as polymers, metals, ceramics, and composites, can now be used. The form of the feedstock material and the method of material consolidation are critical, leading to seven main families of additive manufacturing [16]. Additive manufacturing involves building magnets layer by layer using techniques that allow precise control over the magnet's shape and internal structure. This method enables the production of highly complex geometries that are difficult or impossible to achieve with traditional methods, reduces material waste, and allows for the use of tailored magnetic properties through gradient structures. It also offers the potential for rapid prototyping and custom magnet designs. However, the magnetic properties of 3D-printed magnets are generally lower than those produced by traditional methods. The technology is still developing, facing challenges related to scalability and cost-effectiveness for large-scale production. Material and process optimisation is ongoing to improve the magnetic and mechanical properties of the printed magnets.

Vat photopolymerisation has emerged over the years as very important additive manufacturing process. It has been used commercially to solidify photopolymer resin layer by layer, thereby creating highly detailed and smooth objects. For ceramic or metal materials, the process uses a photocurable paste or slurry. Technologies such as stereolithography (SLA), which uses UV light, digital light processing (DLP) and continuous liquid interface production (CLIP), which uses visible light, improved the flexibility and precision of vat photopolymerisation. This technology is further superior to the extrusion-based AM technologies because of its high spatial resolution and complex shape construction with smooth surfaces. Yet, application is usually restricted to photopolymers, and generally, there are needs for post-processing steps.

Powder bed fusion (PBF) is an advanced additive manufacturing technology that uses a heat source, either laser or electron beam, to selectively melt and fuse material powder layer by layer into solid parts. It has been applied in fabrication of complex geometrical designs, including intricate hollow features that are challenging to achieve with co manufacturing methods [17]. PBF offers high customisation capabilities, making it particularly effective for creating permanent magnets with high geometric complexity and superior mechanical properties. In manufacturing permanent magnets, PBF extensively utilizes laser sources due to their precision and efficiency. Critical parameters in the PBF

process, such as laser power, exposure time, and hatching distance, play a significant role in determining the quality and characteristics of the final product [18], [19], [20], [21]. For example, shorter exposure times may result in insufficient melting of the powder, leading to lower densities and weaker structural integrity. On the other hand, longer exposure times can cause overheating, resulting in cracks and delamination that compromise the magnet's performance and durability. The geometry and size of the printed objects also influence internal stresses and the risk of delamination and cracking, especially in smaller volumes that solidify faster and may not manage heat as efficiently as larger pieces [19], [20]. The development of samarium cobalt magnets has been particularly challenging due to their high thermal sensitivity and tendency to oxidize and distort. However, PBF offers a promising method for producing flexible SmCo shapes and 3D structures by optimizing laser power, scanning speed, sintering times, and hatch space. This approach has successfully enhanced crystallisation and optimized the magnetic properties of $SmCo_5$, demonstrating PBF's ability to handle challenging materials effectively [22]. In addition to Nd–Fe–B and Sm–Co magnets, isotropic Sm–Fe–N bonded magnets have also been successfully produced using PBF. This process employed a CO_2 laser to melt a mix of 6 wt.% polyamide 12 (PA12) polymer binder and Sm–Fe–N flake particles without degrading the magnetic phase, highlighting PBF's versatility and potential in manufacturing high-performance permanent magnets with diverse material compositions [23].

Binder jetting is an additive manufacturing process that uses a liquid bonding agent to fuse powder materials such as metals, ceramics, and sand. The process typically involves spreading a layer of powder over the building platform using a powder spreading tool, followed by a print-head jetting the bonding agent into the powder layer. This sequence is repeated with successive layers of powder and binder until the entire part is formed. The printed part, known as the "green" part, is then cured in the building chamber, and any excess powder is removed [24]. Further post-processing is often required to achieve the final form. Commercial systems supporting binder jetting include those from Desktop Metal, ExOne, GE Additive, and Voxeljet [25]. The binding agents can be organic or inorganic, enabling large build volumes across a wide range of materials [26]. This versatility makes binder jetting adaptable for producing bonded magnets with near-net-shape designs. However, one of the significant challenges of this process is maintaining the speed of spreading the magnetic powder without disturbing the previously laid layers. Typically, printed magnets are porous and have a rough surface finish, which infiltration processes can mitigate. For example, using clear urethane resin as an infiltrant can enhance the mechanical strength and surface quality of the printed part, resulting in a measured density of 3.47 g/cm^3 with a magnetic filler loading of 46 vol.% (equivalent to 85 wt.%), achieving a coercivity of 716 kA/m and a remanence of 300 mT [27]. Further studies have explored the use of low-melting-point alloys like NdCuCo and PrCuCo as infiltrants, showing an 80% increase in coercivity post-infiltration, although with lower remanence values compared to the as-printed samples [28]. This reduction in remanence is due to the volume expansion from the infiltration process and the non-ferromagnetic nature of the infiltrants, illustrating some of the complexities and trade-offs involved in optimizing binder jetting for magnetic applications.

Material jetting is an advanced additive manufacturing technique that operates similarly to conventional ink-jet printing. In this process, droplets of build material are selectively deposited through nozzles, and once the material is laid down, it is typically cured using UV light or allowed to solidify at room temperature. The thin layers cure quickly, often eliminating the need for extensive post-processing steps. Known for its high precision, material jetting is currently limited to a relatively small range of materials [29]. Similar to stereolithography (SLA), material jetting can incorporate an external magnetic field to align magnetic particles during the printing process. The magnetic field source

could be an electromagnetic coil [30], a rotating Nd–Fe–B magnet [31], or a custom-designed rotating magnetic frame [32]. These setups help achieve particle alignment, resulting in reduced hysteresis loss and increased high-frequency permeability, which enhances the functional properties of the printed objects. Material jetting has been effectively used to print complex-shaped Nd–Fe–B bonded magnets with the addition of $SrFe_{12}O_{19}$, achieving a relative density of over 98%. Using 20 wt.% $SrFe_{12}O_{19}$, these magnets maintain excellent dimensional accuracy and surface quality (about 6 µm roughness) while showing strong filament coalescence. Although adding $SrFe_{12}O_{19}$ reduces the overall magnetic properties, it significantly improves the coercivity temperature coefficient, enhancing thermal stability. These attributes make printed Nd–Fe–B-based magnets with $SrFe_{12}O_{19}$ suitable for applications at higher temperatures, significantly reducing tooling costs and minimizing the waste of rare earth materials [33].

Material extrusion, particularly through methods such as fused deposition modelling (FDM) and fused filament fabrication (FFF), is one of the most widely employed additive manufacturing technologies today. In these processes, thermoplastic filaments serve as the feedstock material. These filaments are loaded into an extruder, heated to a molten state, and precisely deposited onto the printer bed through a nozzle to build the object layer by layer. A key challenge in FDM is the production of filaments, which must be extruded with strict adherence to specific diameter and ovality tolerances to ensure consistent printing at a constant flow rate. Additionally, these filaments must balance stiffness and flexibility to facilitate easy spooling and unspooling during production and printing while maintaining homogeneity to avoid defects in the printed objects [34]. The manufacturing of printable filament for FDM of permanent magnets presents unique challenges, particularly due to the incorporation of magnetic powders bonded with polymers that alter the flow and melting behaviours of the material. Various polymers have been utilized to bond Nd–Fe–B powders for this purpose, including polyamide 11 [35], polyamide 12 (PA12) [36], [37], thermoplastic polyurethane [38], PPS [39], [40], [41], and polyether ether ketone [40], [41]. Each polymer impacts the final product differently, influencing key properties such as durability, magnetic strength, and thermal stability based on its specific characteristics. One study demonstrated the potential of FDM technology for printing magnets directly integrated into a functional prototype of a rotary blood pump [42]. This was achieved using a specially developed five-component polymer-bonded magnetic compound, showcasing the capability of FDM to create complex, integrated magnetic systems within single print processes. The challenge of filament production in FDM can be overcome by employing a material extrusion technology known as big area additive manufacturing (BAAM). BAAM utilizes pre-compounded materials in pellet form, which are extruded to facilitate printing large-scale objects. While BAAM bypasses the complexities associated with filament production, it is generally more costly and offers lower resolution [43]. Despite these trade-offs, BAAM-printed magnetic components have shown superior magnetic properties compared to those produced by conventional injection moulding methods, highlighting its potential for advanced manufacturing applications where enhanced magnetic performance is critical [44]. Recent advancements in additive manufacturing have focused on the potential of anisotropic permanent magnets, which permit higher magnetic performance than isotropic magnets. This is exemplified in applications using $SrFe_{12}O_{19}$-based filaments with PPS as the binder, which are fabricated and 3D printed for use in harsh environments like automotive applications, withstanding temperatures up to 200 °C. Despite challenges due to PPS's extrusion difficulty, adjusting the filling factor to 70 wt.% enabled effective printing, significantly enhancing magnetic alignment and remanence when printed in an external magnetic field, demonstrating the potential for advanced manufacturing of high-performance magnets [45]. In this context, it's significant to recognize and highlight the in-situ alignment capabilities demonstrated in FDM printing of magnets with $SrFe_{12}O_{19}$ in a

polyamide 6 matrix at a fill grade of 49 vol.% and $Sm_2Fe_{17}N_3$ in a PA12 matrix at a 44 vol.% fill grade. Achieving a remanent magnetisation to saturation magnetisation ratio of 0.70 was possible with $SrFe_{12}O_{19}$ under an external magnetic field, which could be adjusted by changing the distance from the magnets. However, This alignment technique was ineffective for $Sm_2Fe_{17}N_3$, indicating the need for a stronger magnetic field to properly align these materials [47]. For successful alignment of $Sm_2Fe_{17}N_3$, a magnetic field greater than 1.5 T is necessary. However, current limitations in printing technologies restrict external field strengths to less than 150 mT during the printing process [46]. Additionally, the utilisation of BAAM to print magnets comprising 70 vol.% anisotropic Nd–Fe–B and 30 vol.% PA12 has shown promising results. These magnets were aligned post-printing using an external magnetic field up to 3.0 T, demonstrating a high energy product of approximately 143.2 kJ/m^3 at a 1.0 T field alignment [47]. While developing anisotropic BAAM-printed magnets represents a significant achievement, their larger size and lower resolution pose challenges, particularly for applications requiring compactness, such as automotive sensors.

Each production method for permanent magnets offers unique benefits and faces specific challenges presented in Table 1-1. The choice of method depends on specific application requirements, including magnetic performance, shape complexity, production volume, and cost constraints. As technology advances, these methods evolve, providing improved performance and new opportunities for innovative applications in various high-tech sectors, including automotive, aerospace, and renewable energy.

Table 1-1: Comparison of various production methods for permanent magnets.

Method	Advantages	Disadvantages
Sintering	High magnetic performance; ability to create complex shapes and sizes; high density.	High energy consumption due to high temperatures and controlled atmospheres; sensitivity to impurities; costly and complex post-processing required.
Injection moulding	Suitable for complex shapes and thin walls; lower manufacturing temperatures and energy requirements; versatile in automotive applications	Lower magnetic performance due to binder dilution; reduced mechanical strength and thermal stability.
Vat photopolymerisation	High spatial resolution; ability to produce complex shapes with smooth surfaces.	Limited to photopolymers; requires post-processing steps.
Powder bed fusion	High customisation; effective for complex geometries and superior mechanical properties; versatile with various materials.	Critical parameter sensitivity (laser power, exposure time); risk of internal stresses and delamination; higher production costs.
Binder jetting	Versatile with large build volumes; suitable for near-net-shape designs; adaptable to various materials	Porosity and rough surface finish; requires post-processing (infiltration) to enhance mechanical properties; maintaining powder layer stability is challenging.
Material jetting	High precision;	Limited range of materials.

	suitable for integrating magnetic fields during printing.	
Material extrusion	Widely used (FDM, FFF, BAAM); suitable for large-scale objects; flexible combining materials; relatively low cost.	Challenges in filament production; lower resolution; balance needed between stiffness and flexibility for filament spooling.

1.4 Challenges in the Use of Nd–Fe–B Polymer-Bonded Magnets

Despite their advantages, Nd–Fe–B magnets also have major disadvantages. Nd–Fe–B magnets are highly susceptible to corrosion, which can significantly affect their durability and performance under various environmental conditions [48]. The major corrosion mechanism of Nd–Fe–B magnets, is primarily due to the fast oxidation of Nd–rich and B–rich phases at the grain boundaries of the magnetic tetragonal compound $Nd_2Fe_{14}B$. These intergranular phases are prone to corrosion, mainly in moist or acidic conditions, which leads to their preferential dissolution. Consequence of the dissolution process is detachment and loss of ferromagnetic grains, compromising the structural integrity and magnetic properties of the magnet [49]. The corrosion threatens the magnet's longevity and restricts its use in environments prone to moisture and temperature fluctuations [50]. In humid conditions, Nd–Fe–B magnets can undergo the following reactions, which often lead to rapid decomposition of the intergranular phase due to water vapour at high temperatures:

$$2Nd + 3H_20 \rightarrow NdH_3 + Nd(OH)_3 \tag{1.1}$$

$$NdH_3 + 3H_20 \rightarrow Nd(OH)_3\, 3H_2 \tag{1.2}$$

$$Nd + \frac{3}{2}H_2 \rightarrow NdH_3 \tag{1.3}$$

These reactions demonstrate how the intergranular phase interacts with water, producing Nd-hydroxide and hydrogen. The hydrogen further reacts with the Nd-rich intergranular phase to form Nd-hydride, which is unstable under these conditions and decomposes back into Nd-hydroxide and hydrogen, repeating the cycle. This ongoing process exacerbates the conversion of neodymium into Nd-hydroxide, leading to significant volume expansion in the intergranular phase, which results in cracking along the grain boundaries and ultimately, complete decomposition of the magnet into a powder [50], [51]. Further, in aqueous acidic conditions, the susceptibility to dissolution increases in the following order for the non-coupled single phases: ferromagnetic phase $Nd_2Fe_{14}B$ > Nd-rich phase > B-rich phase $Nd_{1+\varepsilon}Fe_4B_4$. The differing electrochemical potentials of the three phases primarily result in galvanic corrosion, where intergranular regions of more negative electrochemical potentials of the Nd and B-rich areas are attacked first causing their anodic dissolution [51], [52].

In this way, it has remained one of the challenges concerning effective adhesion between magnetic particles and the polymer matrix in PBMs, important to ensure mechanical integrity and optimal performance under a wide variety of conditions [53]. Enhanced adhesion of magnetic particles with the polymer binder in PBMs provides a promising solution to mitigate these issues. Improved adhesion protects the magnetic particles from environmental exposure, minimising possibilities of corrosion and prolonging the operational lifespan of the magnets.

PBMs benefit from the polymer binder, which encapsulate the magnetic particles, thus protecting them from corrosion and oxidation. However, the efficiency and durability of PBMs significantly depend on the integrity of the composite material. In Nd–Fe–B PBMs, the potential causes of poor adhesion at the interface between the magnetic particles and polymer matrix, such as oxide layer formation on the filler during processing in air or crosslinking of the polymer, pose a significant challenge, undermining the mechanical strength and overall performance of the final product [54]. This issue is even more pronounced in additive manufacturing, where the interfacial adhesion between polymer and metal is notably weaker than within the pure polymer itself, further compromising the mechanical strength and overall performance of the final product. Therefore, addressing the reduction in interfacial adhesion is critical for enhancing the efficiency and extending the longevity of Nd–Fe–B PBMs, ultimately broadening their range of applications.

To improve the adhesion and corrosion resistance of Nd–Fe–B magnets, various strategies have been employed. Surface treatment of the magnetic powder, such as passivation pre-treatments including phosphatising [55], [56] or chromatisating [57], followed by coating with silanes, has been explored through wet chemistry routes [58], [59]. The application of liquid crystal polymer (LCP) enhances the wetting of Nd–Fe–B powders by PPS, significantly improving the magneto-mechanical properties of thermoplastic Nd–Fe–B magnets [60]. Silanes are versatile adhesion promoters that form molecular bridges between organic resins and inorganic fillers, creating durable, chemical-resistant bonds. These agents start by hydrolysing to form silanols, reacting with moisture to integrate tightly with substrates that have surface hydroxyl groups, enabling stable covalent bonding. Silanes are particularly effective on materials with abundant reactive hydroxyls, such as silica and oxides, enhancing the adhesion and stability of composites across various applications [61]. However, their application in industrial settings can be complex due to the need for specialized methods. Techniques such as spraying, slurry application, and in-situ coating are utilized to effectively bond silanes to fillers, requiring precise control of application rates, dwell times, and temperatures to ensure successful integration and maintain the reactivity of silanes. These processes, while effective, demand careful setup and monitoring to avoid issues like incomplete reactions or safety hazards such as explosions from volatile by-products [61]. The bonding mechanisms of silane-based coatings are presumed to involve both chemical bonds and physical adsorption. As silanes undergo hydrolysis, they form reactive silanol groups that can potentially bond with hydroxyl groups on the magnetic powder surface through condensation reactions, forming a durable Si—O—Metal bond crucial for the stability and effectiveness of the coating. The current literature and available data, however, do not extensively cover the specific molecular interactions at play, revealing a significant gap in our comprehensive understanding of how exactly these silane coatings interact at the molecular level with the surface of magnetic powders. While the general application and benefits of such coatings are well-documented, the intricate details of these interaction mechanisms remain under-explored. This thesis acknowledges the necessity of filling this knowledge gap and suggests that future research efforts employing advanced analytical techniques such as X-ray photoelectron spectroscopy, Fourier-transform infrared spectroscopy, and atomic force microscopy could prove invaluable. These studies could uncover the precise nature of these interactions, potentially revolutionizing the application of these coatings and significantly enhancing the performance and longevity of magnetic materials in various industrial settings. Another strategy employs adhesion promoters, such as organo-titanates [62], [63], to improve adhesion. Titanate coupling agents enhance the functionality of fillers in plastics by chemically bridging inorganic and organic materials through proton coordination, enabling reactions with non-hydroxyl substrates. These agents facilitate in-situ reactions within the thermoplastic melt, improve flame retardancy, and enable the particulate surfaces to

become hydrophobic and organophilic, which aids in achieving better dispersion and integration of fillers into the polymer matrix without the need for water [64].

Plasma technology is another promising method for modifying or enhancing surface properties, such as corrosion resistance and electrical, thermal, or mechanical characteristics. Plasma treatments involve the use of ionized gases to modify the surface characteristics of materials without altering their intrinsic properties. This process is advantageous for several reasons, including its ability to clean, etch, and functionalize surfaces at an atomic or molecular level [65]. The mechanism behind plasma surface treatments involves the generation of a plasma field in a controlled environment, typically within a vacuum chamber. In this field, gases such as argon, nitrogen, or oxygen are ionized, creating a mixture of ions, electrons, and reactive neutral species. When these reactive particles collide with the surface of a treated material, they can induce various physical and chemical changes. These changes include the removal of surface contaminants, the alteration of surface roughness, and the introduction of functional groups. Plasma treatment is particularly economical and environmentally friendly as it requires no water or chemicals, unlike other surface-modification methods [63], [66], [67]. Plasma treatments have been applied to diverse materials, enhancing wetting properties in various polymers, improving the adhesion of plasma-deposited coatings, reducing friction, upgrading biomaterials, and strengthening the bond between thermoplastic polymers and metal surfaces [66], [67], [68], [69]. Plasma treatments successfully modify the surface of PA12, where low-pressure microwave plasma makes PA12 wettable [68], [69]. There has been no published research specifically addressing the plasma treatment of Nd–Fe–B powder, indicating a potential gap in the current scientific literature that could open new avenues for enhancing the properties of these materials. This lack of studies underscores the need for innovative research to explore the effects of plasma treatment on the performance and durability of Nd–Fe–B magnets. Future research should continue to focus on optimising the manufacturing processes and surface treatments to improve the properties and performance of PBMs further.

1.5 Strategies to Reduce Dependency on Rare Earths and Environmental Considerations

The global reliance on rare earth permanent magnets, particularly Nd–Fe–B magnets, has been fundamental in driving technological advancements across various sectors, as outlined in Subchapter 1.2. These magnets, favoured for their exceptional magnetic properties, including higher energy density and compact size compared to traditional magnets, present substantial environmental and supply chain challenges [70]. The extensive use of these materials necessitates urgent measures to support ongoing technological innovation and address sustainability concerns.

A primary issue is the significant dependency on rare earth materials sourced predominantly from China, which controls over 80% of the global supply [71]. This dependence introduces considerable sustainability and geopolitical risks, prompting the need its mitigation.

To enhance the sustainability of the magnet industry, comprehensive strategies are being pursued. These include developing efficient recycling processes that help reduce the need for virgin raw material extraction [72], [73] and researching alternative materials that do not require rare earth elements [74]. Such materials could match the performance of existing Nd–Fe–B magnets with future advancements in material science. Notable advancements in reducing rare earth content have been achieved by developing Dy-free Nd–Fe–B anisotropic bonded magnets. These magnets, made using Nd–Cu–Al elements

and produced via the d-HDDR method, showcase the potential to maintain high coercivity without dysprosium [75]. Additionally, improving the design and robust surface treatments of magnets can extend the lifespan of products, thereby decreasing the overall demand for replacements and reducing reliance on rare earth supplies [76].

This thesis focuses on exploring innovative surface treatment methodologies that enhance the mechanical integrity, magnetic characteristics, and environmental resistance of polymer-bonded Nd–Fe–B magnets. By advancing these technologies, the thesis aims to contribute to more sustainable and efficient use of rare earth magnets, addressing critical challenges and enabling broader applications in essential technological fields.

Chapter 2

Objectives and Structure of the Thesis

2.1 Objectives

The primary objective of the thesis was to optimize surface treatment methodologies that enhance the mechanical integrity, magnetic characteristics, and environmental resistance of fabricated polymer-bonded Nd–Fe–B magnets. Specifically, the dissertation aimed to improve the adhesion between Nd–Fe–B magnetic powder and the polyamide matrix through advanced surface treatments, utilize both injection moulding and fused deposition modelling for magnet fabrication to achieve superior material properties, and evaluate the performance of these magnets under various environmental conditions to assess their industrial applicability. Additionally, during research a highly filled printable filament comprising 93 wt.% Nd–Fe–B bonded with 7 wt.% PA12 was successfully developed, addressing one of the greatest challenges in the FDM production of permanent magnets.

2.2 Hypotheses

The central hypothesis of this dissertation is that by applying an appropriate surface treatment to polymer-bonded Nd−Fe−B magnets, we can not only significantly enhance their mechanical strength, magnetic properties, and resistance to environmental factors but also improve their overall processability. We hypothesize that:

- Hypothesis 1:
  Surface modifications through a combination of phosphatisation treatment, and subsequent applying tetraethyl orthosilicate (TEOS), and 3-aminopropyltriethoxysilane (APTES) significantly enhance the mechanical and environmental performance of Nd−Fe−B polymer-bonded magnets without compromising their magnetic properties.

- Hypothesis 2:
  Organo-titanate as a dry coupling agent in the FDM filament fabrication improves the adhesion between the inorganic filler and the organic polymer matrix, thus improving the mechanical properties and environmental stability of the printed magnets.

- Hypothesis 3:

Plasma treatments significantly enhance the mechanical and magnetic properties of Nd−Fe−B/PA12 magnets printed via FDM without compromising their environmental stability.

- Hypothesis 4:
  Using gas-atomised magnetic particles in FDM printing improves density, reduce porosity, and enhance magnetic properties and environmental stability compared to magnets made with melt-spun powders.

2.3 Structure of the Thesis

The dissertation is structured around three core publications, each detailed in its chapter and addressing different aspects of surface treatment for polymer-bonded Nd−Fe−B magnets.

Chapter 3, representing Publication I, focuses on enhancing the mechanical properties and environmental stability of Nd−Fe−B magnets through wet chemical modifications like phosphatisation, TEOS, and APTES. This chapter emphasizes the critical role of surface treatments in improving adhesion and achieving enhanced mechanical and environmental resilience, supporting Hypothesis 1. Chapter 4, detailing Publication II, introduces a dry coupling agent based on organo-titanate into the feedstock material. This integration aims to enhance the adhesion between inorganic Nd–Fe–B powder and organic PA12 binder. The chapter explores the development of highly filled filaments and assesses how the shape of filler particles influences the density and porosity of FDM printed magnets, thereby supporting Hypotheses 2 and 4. Chapter 5 explores Publication III, which investigates the use of plasma treatments to enhance the properties of Nd−Fe−B/PA12 magnets. It supports Hypothesis 3 by examining the application of plasma treatments to magnetic powders and PA12 and testing the FDM printed samples for mechanical and environmental stability.

These publications collectively explore innovative techniques aimed at improving the mechanical properties, magnetic performance, and environmental stability of the magnets, each contributing uniquely to the field of material science and magnet manufacturing.

2.4 Contribution of the Thesis

The main scientific contributions of this dissertation are:

- Successful implementation of surface treatments significantly improves the mechanical properties and corrosion resistance of the magnets. This leads to better adhesion between the magnetic powders and the polymer matrix, reducing flux loss and boosting mechanical strength—marking a crucial advancement in the surface treatment of magnetic materials.
- Plasma treatments can enhance the interfacial adhesion between magnetic powders and the polymer matrix, improving mechanical strength and environmental stability while preserving the magnets' magnetic properties. The demonstrated resistance to hygrothermal corrosion in plasma-treated FDM-printed magnets highlights the potential of these magnets in demanding applications, paving the way for more sustainable usage of rare earth magnets.

- Detailed comparative analysis of the effects of particle shapes and surface treatments on the performance of FDM-printed magnets, offering new insights into manufacturing optimisations that bridge the gap between laboratory research and industrial applications.

These studies offer substantial theoretical and practical advancements, promoting more efficient and sustainable magnetic material usage. This thesis bridges the gap between academic research and practical applications, pushing the boundaries of material science and engineering to create more robust, efficient, and sustainable magnetic materials.

2.5 Methodological Approach

The methodological approach of this dissertation investigates the enhancements in Nd−Fe−B polymer-bonded magnets through a series of specified surface treatments and techniques aimed at substantiating the proposed hypotheses. The process begins with wet chemical modification and injection moulding, where magnetic powders are altered in a pilot lab reactor to enhance their surface properties before being moulded into final magnet shapes (Publication I). Following this, dry coupling agents are incorporated into the magnetic powder and polymer blend, which is then extruded into filaments for FDM printing, assessing the impact of these agents on the magnets' properties (Publication II). Additionally, plasma treatments are employed, involving the application of radiofrequency plasma to magnetic powders and low-pressure microwave plasma to polymers. This is intended to enhance their compatibility and adhesion, which are crucial for the durability of FDM-printed magnets (Publication III).

Applied surface treatments are in turn characterized by several advanced techniques in developing an understanding of how they alter the physical and chemical properties of these magnets and influence overall performance. Scanning electron microscopy (SEM) with energy dispersive X-ray (EDX) spectroscopy (Publication I-III) offering morphological and elemental composition information. Fourier-transform infrared spectroscopy (FTIR) helps in identifying specific bonding and functional groups (Publication I), while thermogravimetric analysis (TGA) and differential scanning calorimetry (DSC) evaluate the thermal stability and crystallinity of the materials.

Further measurements include tests on magnetic properties using vibrating sample magnetometry (VSM, Publication I) and tools such as a Helmholtz coil and permeameter (Publications I-III). Mechanical integrity is tested through tensile and flexural strength tests (Publications I and III), and environmental durability testing exposes the magnets to severe conditions like thermal cycles and corrosive environments to gauge their functional stability over time (Publications I-III). These comprehensive testing protocols ensure that the magnets can maintain their magnetic properties under adverse conditions, providing a robust validation of the surface treatments' effectiveness. More detailed parameters and protocols are provided in the respective chapters of each publication.

Chapter 3

Wet Chemical Modification

Publication I
A. Damnjanović, I. Milošev, and N. Kovačević, "Enhanced mechanical properties and environmental stability of polymer-bonded magnets using three-step surface wet chemical modifications of Nd–Fe–B magnetic powder" Heliyon, vol. 10, no. 4, p. e26024, Feb. 2024, doi: 10.1016/j.heliyon.2024.e26024

3.1 Introduction

In recent decades, polymer-bonded magnets based on Nd–Fe–B alloys have emerged as highly promising materials with significant contributions to technological advancements. They offer higher energy products in reduced volumes than conventional materials, making them indispensable in modern technologies. These magnets are crucial in 'green technology' applications such as electric vehicles and wind turbines, which are vital for addressing climate change concerns [70].

The manufacturing of PBMs involves mixing magnetic powder with a binder and using either compression or injection moulding. Recently, additive manufacturing methods like fused deposition modelling have also been utilised for fabricating PBMs [36], [77]. Injection moulding, although requiring more polymer for better flow (35–40 vol.%), allows for complex shapes but results in slightly reduced magnetic strength due to higher binder content [78], [79]. PBMs offer greater design flexibility compared to sintered or hot-deformed types and can be used in a variety of applications, from computer storage to automotive products.

Depending on desired properties and final applications, various polymers can be utilised as binders. The commonly employed binder is solid epoxy resin, owing to its convenient moulding and processing characteristics in the industrial production of bonded magnets. Nevertheless, the use of bonded magnets in advanced industries has been hindered by the limited ability of epoxy binders to withstand high temperatures, resist corrosion, and maintain satisfactory mechanical performance [80]. Regarding moldability and mechanical strength, binder resins such as thermoplastic polyamide 12 are preferable because they allow for higher filler loadings of up to 70 vol% [81], [82], [83]. Other polymers, such as polyphenylene sulfide, offer advantages in terms of heat resistance but require a smaller filler load [84]. Polyether ether ketone, utilised in space applications, complies with stringent aerospace requirements by having high thermal stability, low outgassing, low flammability, and high radiation resistance [41]. By selecting an appropriate binder polymer based on desired properties and applications, enhanced performance and expanded possibilities for bonded magnets can be achieved.

However, there is a pressing need for more sustainable usage of PBMs, given their susceptibility to oxidation and corrosion, which can shorten the lifespan of magnet assemblies. One approach to enhance sustainability involves depositing functional coatings on magnetic substrates. These coatings improve surface properties, including oxidation resistance, mechanical strength, and electrical and thermal conductivity [85]. Another strategy focuses on the compatibility between magnetic particles and polymers. Various methods have been studied to improve this interaction, and silane coupling agents have emerged as particularly effective. The silanes serve dual purposes: they facilitate the mechanical bonding of magnetic powder and polymer and maintain desirable magnetic properties and corrosion resistance.

Surface modification methods employing organo-silane coupling agents have attracted significant attention because of their remarkable corrosion resistance and strong adhesion properties. The primary chains of organic polymers, characterised by siloxane bonds (Si–O–Si), possess higher bond energies than C–C and C–O bonds. The helical structure and presence of organic groups within these bonds contribute to reduced intermolecular forces, leading to decreased surface tension and enhanced water repellence. Coating agents with the general formula R–Si−$(OR')_n$, where R and R′ represent alkyl groups, and n is either 3 or 4, exhibit promising potential [86]. Applying a monolayer of the coating agent onto the surface of the powder offers several advantages. First, it reduces the viscosity of suspensions, resulting in improved dispersion. Second, it enhances the hydrophobicity of the powder surface, leading to enhanced water repellence. Finally, it facilitates compatibility with the polymer matrix by enabling chemical bonding between the powder and the polymer through hydrogen or ionic bonds. These interactions strengthen the overall adhesion between the coated powder and polymer matrix, thereby enhancing the performance of the composite material [82], [87], [88]. Applying a silane coupling agent to coat Nd–Fe–B powders offer the necessary resistance to oxidation and corrosion during processing. Various silane agents can be utilised to treat the surface of Nd–Fe–B, such as tetraethoxysilane [55], N-(2-aminoethyl)-3-aminopropyltrimethoxysilane [54], 3-aminopropyltriethoxysilane [89] and (3-glycidoxypropyl)trimethoxysilane [90]. These silane agents play a crucial role in enhancing the stability and protective properties of the surface of Nd–Fe–B powders, ensuring their suitability under the intended processing conditions. In commercial applications, silanes are commonly mixed with magnetic powder in liquid form to act as coupling agents. However, ensuring a homogeneous mixture throughout the magnetic powder can be challenging. This study aims to evaluate a three-step surface modification of Nd–Fe–B magnetic powder for its impact on the mechanical properties and environmental stability of injection-moulded PBMs. Additionally, the variability in the volume ratio of polymer to magnetic filler, as well as the use of diverse polymers, fundamentally changes the mechanical properties and affects the environmental stability and magnetic characteristics of these magnets. Therefore, to maintain the integrity and specificity of our findings, we have consciously chosen not to use the work of other authors for comparison in this study.

3.2 Materials and Methods

3.2.1 Materials

The magnetic filler used in this study was a commercial isotropic MQP B+ (− 150 mesh) powder provided by Magnequench. MQP B+ powder, composed of an Nd–Fe–Co–B alloy, was produced using a melt-spinning process, forming particles with an irregular flakelike

morphology. As- received magnetic powder exhibited the following magnetic properties: residual remanence within the range of 895–915 mT, coercivity between 716 and 836 kA/m, and a maximum energy product of 126–134 kJ/m^3 [91]. Polyamide 12, a polymer binder, was used in either powder or pellet form (Vestosint and Vestamid, respectively, from Evonik, Italy). A phosphoric acid solution was employed as a first step, while tetraethyl orthosilicate was utilised as a coupling agent. 3- aminopropyltriethoxysilane was grafted onto the TEOS layer as the final modification step. Isopropyl alcohol (IPA) was used as a dilution solution. All chemicals were supplied by Sigma-Aldrich (Slovenia).

3.2.2 Surface modification of Nd–Fe–B powder

Magnetic powder particles were coated using patented technology/procedure [92]. The powder coating was performed using a Reactor-Ready pilot lab reactor (Radleys, UK), which comprised a reaction vessel, an overhead polytetrafluoroethylene anchor stirrer, and a vacuum-jacketed option connected to a Huber Ministat 230 thermoregulator/circulator. The integration of these components enables rapid heating or cooling within the system, which is essential for producing high-quality powder coatings.

The first step involved a phosphating treatment, wherein a mixed solution of 0.5 wt.% phosphoric acid solution, 2.5 wt.% IPA and MQP B+ were added to the lab reactor and stirred for 10 min in air at atmospheric pressure. The mixture was then heat-treated for 1 h at 80 °C and subsequently for 2.5 h at 120 °C. However, because the volume of the solution was insufficient for a uniform dispersion, more IPA was added.

In the second step, a composite coating layer is obtained by adding a mixed solution of 0.7 wt.% TEOS, 0.30 wt.% phosphoric acid, 0.26 wt.% deionised water (DI), and 2.5 wt.% IPA to the powder obtained in the previous step and mixed for 10 min. Because the volume of the diluting solution seemed insufficient for a uniform dispersion, more IPA was added. The obtained mixture was heat-treated for 1 h at 80 °C and subsequently for 2.5 h at 120 °C in air at atmospheric pressure while stirring.

In the final step, MQP B+ powder coated with a phosphate layer and a TEOS layer from the first and second steps was subject to the silane coupling agent APTES, which exhibits the best rust-prevention properties. The coated powder was mixed with a solution of 0.5 wt.% APTES, 2.5 wt.% IPA, and 0.3 wt.% DI, stirred for 10 min in an air atmosphere and then heat-treated while stirring at 100 °C for 1 h in the air at atmospheric pressure.

All powders obtained were cured in an oven at 100 °C for 1 h.

Several batches were produced to evaluate the differences that may arise between the presence and absence of TEOS and APTES, respectively, as presented in Table 3.1. The surface modification of the batch, subsequently employed in the industrial manufacturing of PBMs, followed a three-step process, as illustrated in Figure 3-1.

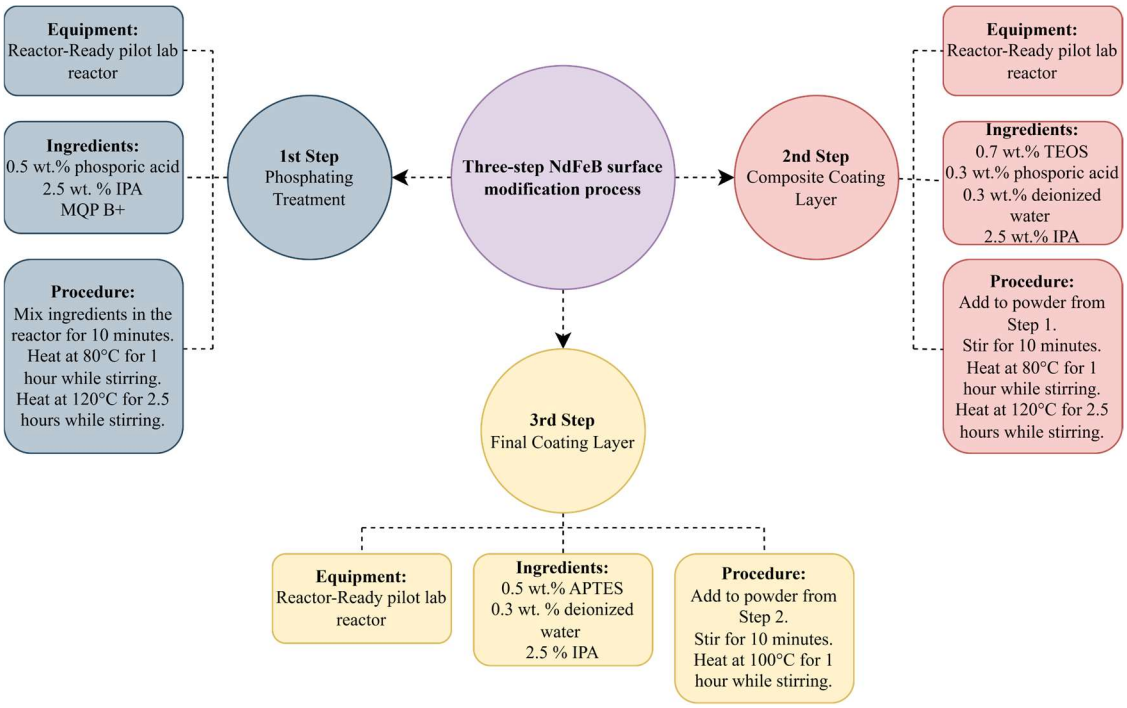

Figure 3-1: Schematic representation of the three-step surface modification process of the batch MQP B+/H_3PO_4/APTES.

Table 3-1: Overview of magnetic powder batches with different coating layers.

Batch name of magnetic powders	Surface modification
As-received MQP B+	none
MQP B+/H3PO4	phosphate coatings
MQP B+/H3PO4/TEOS	phosphate + TEOS coatings
MQP B+/H3PO4/TEOS/APTES	phosphate + TEOS + APTES coatings
MQP B+/H3PO4/APTES	phosphate + APTES coatings

3.2.3 Injection moulding of Nd–Fe–B bonded magnets

PBMs were produced in manufacturing facilities at Kolektor KFH. Before injection moulding, the magnetic powder was mixed with additives by combining 99 wt.% of filler and 1 wt.% of additives for 2 min. Additives were added to provide a better dispersion of the polymer, better flow properties, and less friction. This mixture was added to the first dosage unit of the two-screw extruder in a 93 wt.%, and in the second dosage unit, 7 wt.% of PA12. The temperature in the multibarrel zone extruder ranged from 160 °C to 230 °C. The resulting mixture was kneaded, extruded, and cut into pellets.

Subsequently, the pellets were injection-moulded to produce the bonded magnets. The temperature range in the injection moulding unit ranged from 230 °C to 295 °C, with the pressure varying from 804 to 868 bar. PBMs were produced in the shape of cylinders and dog-bone-shaped tubes. The total length of the test tube was 150 mm, with a 50 mm – test section gauge length and 20 mm wide, whereas the injection-moulded cylinders were 10 mm × 9.9 mm. Dog-bone-shaped tubes were produced to evaluate mechanical properties, whereas cylinders were used to evaluate environmental stability.

Two batches were produced. The first batch included as-received MQP B+ powder and PA12. Cylinders were made of as-received MQP B+ powder and PA12 powder, whereas dog-bone-shaped-tubes from as-received MQP B+ powder and PA12 pellets. This is because the manufacturing process was optimized for PA12 pellets, and only cylinders were injection-moulded without defects with PA12 powder. Therefore, we used dog-bone-shaped tubes from Kolektor KFH regular production, i.e., as-received MQP B+ powder bonded with PA12 pellets. The second batch included MQP B+ powder, modified with phosphate and subsequently with silanes, bonded with powdered PA12, and labelled modified MQP B+/PA12.

3.2.4 Characterisation

Different methods were used to characterise the surface of the as-received MQP B+ powder and modified powder from batch MQP B+/H_3PO_4/TEOS/APTES and evaluate the efficiency of the coating layers against corrosion. Fourier-transform infrared spectroscopy was used to obtain the infrared spectrum of absorption of the as-received and coated powders. FTIR spectra of samples were measured by PerkinElmer Spectrum 100, using an attenuated total reflectance mode ATR sampling accessory.

Magnetic measurements of the uncoated and coated powders were performed using a vibrating sample magnetometer (VSM, LakeShore 7307) at room temperature. All samples were first magnetized before the VSM measurement. For this measurement, hysteresis loops were plotted as magnetisation, M as a function of the applied field, and H (M − H loop).

The as-received and modified powders were subjected to thermogravimetric analysis to determine the effect of temperature on the oxidation and corrosion susceptibility. TGA tests were performed on the uncoated and coated samples using a Mettler Toledo thermogravimetric analyser TGA/DSC1. The test conditions were the same for all samples in the non-isothermal mode. The samples were heated from ambient temperature to 600 °C at a heating rate of 10 °C/min in the presence of air as the purge gas.

The surface morphology and chemical composition of the as-received and modified and the injection-moulded magnets were determined using SEM coupled with EDX. SEM images and EDS spectra were taken in secondary electron mode using Jeol–IT300 SEM equipped with Oxford EDX at 15 keV energy beam (JEOL ltd). Samples were not pretreated; they were fixed on carbon tape before analysis. Injection-moulded cylinders were magnetized using an impulse magnetizer K-Series (MAGNET-PHYSIK) at a voltage of 2000 V to saturate the samples. After magnetisation, residual remanence and intrinsic coercivity were measured using a permeameter (PERMAGRAPH®, MAGNET-PHYSIK).

The magnetic flux of the magnetized cylinders was measured using a Helmholtz coil (MS 75 with electronic Fluxmeter EF 14, MAGNET-172 PHYSIK), both before and after subjecting them to environmental tests.

Mechanical testing was performed on five dog-bone-shaped specimens at room temperature. The test specimens were injection moulded in specified dimensions according to the standard ISO 527 for 1B type test specimens. Mechanical tests consisted of flexural and tensile tests. The flexural test was conducted using a Zwick test machine (Z100) following standard ISO 178:2001 at a test speed of 1 mm/min [93]. Tensile tests were performed on the same test machine as a flexural test, with different setups, following ISO 527 [94]. The testing speed was 1 mm/min with a load cell of 100 kN.

3.2.5 Evaluation of environmental stability and corrosion resistance

The corrosion resistance of Nd–Fe–B permanent magnets in humid and chloride-containing environments was reported to be remarkably low [95], which is attributed to the reaction

of the Nd-rich phase with H_2O, resulting in the formation of $Nd(OH)_3$ and causing decohesion and dropout of magnetic grains [96]. Such functionality deterioration due to corrosion undermines the strength of the magnets, leading to irreversible loss in flux and, in severe cases, complete disintegration of the magnet.

In this study, the environmental stability and corrosion resistance of Nd–Fe–B magnets were evaluated by measuring the flux loss after exposure to four test environments. The percentage of irreversible flux loss after the tests and after the remagnetisation of samples was calculated to assess environmental stability and corrosion resistance.

To examine the stability of the magnets in an aqueous environment, the magnetized cylinders were immersed in deionized (DI) water at 120 °C and corrosive water at 95 °C for 2000 h, respectively. The corrosive water immersion test was performed following standard ASTM D1384 [97]. The loss of magnetic flux was measured at seven-day intervals after the immersion processes.

For the bulk corrosion test, the cylinders were subjected to pressurized steam at 120 °C for 96 h to assess the material degradation under the combined effect of heat and water vapour. To simulate the effects of rapid temperature changes that may occur during the use of Nd–Fe– B magnets, cylinders underwent temperature shock in air, involving 900 cycles of exposure to temperatures ranging from −40 °C to +140 °C for 30 min each, with a chamber transfer time of less than 10 s.

All the above-mentioned tests were performed on at least three magnetized cylinders for each batch.

3.3 Results and Discussion

3.3.1 Characterisation of as-received and modified magnetic powder

In the referenced literature, an alkoxy oligomer capped with an alkoxysilyl group is recommended for the coating treatment. Among the alkoxy groups, ethoxy groups are preferred due to their reactivity and compatibility, which is why we selected tetraethyl orthosilicate, which is a widely accepted choice in materials science for such applications because of its ethoxy groups [92].

Additionally, for the final coating treatment, we selected APTES from the recommended list of silane coating agents. APTES is renowned for its ability to enhance the interface between polyamide matrices and inorganic materials through its reactive amino and ethoxysilyl groups. These groups facilitate the formation of silanol groups that can bond with substrate surfaces, thus improving filler dispersion and interfacial adhesion, thus contributing to the mechanical robustness and stability of the composites [98].

Figure 3-2 compares the FTIR spectra, depicting the as-received and modified MQP B+ powders and TEOS and APTES. The modified powder exhibits a band at approximately 1100 cm^{-1}, indicating the presence of Si–O–Si and Si–O–C bonds originating from APTES on the powder surface (Fig. 3.2b). Moreover, an additional characteristic band corresponding to C–H stretching from COC was observed at 2900 cm^{-1} [99]. The spectral bands observed on the surface of the modified magnetic powder are in line with those derived from TEOS and APTES silanes (Figure 3-2a). This evidence supports the presence of silane groups on the surface of the modified magnetic powder, thereby confirming the successful implementation of the silane layer.

The results of the VSM measurements, as presented in Figure 3-3, demonstrated that the intrinsic magnetic properties of the modified powders remained unaffected by the

surface coating process. Specifically, the modified specimens exhibited magnetic characteristics similar to those of the as-received powder. This observation was particularly notable for the samples that underwent a three-step modification process, initially with phosphate and subsequently with silanes, as their hysteresis loops overlapped with those of the uncoated powder, confirming the preservation of their intrinsic magnetic properties.

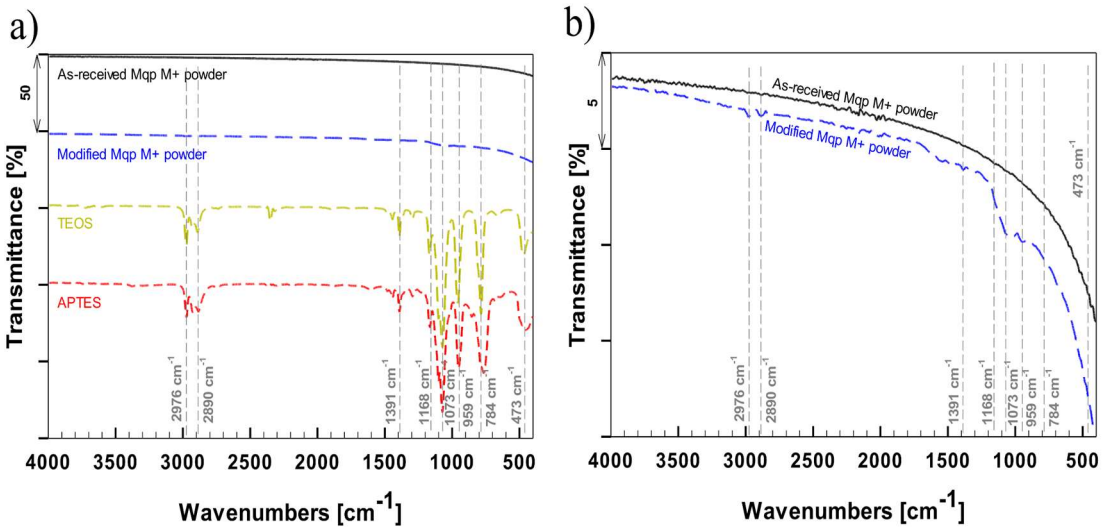

Figure 3-2: FTIR spectra comparison of as-received MQP B+ powder, modified MQP B+ powder, and liquid silanes TEOS and APTES, with a transmission scale up to 50% (a) and FTIR spectra of as-received MQP B+ powder and modified MQP B+ powder with transmission scale up to 5% (b).

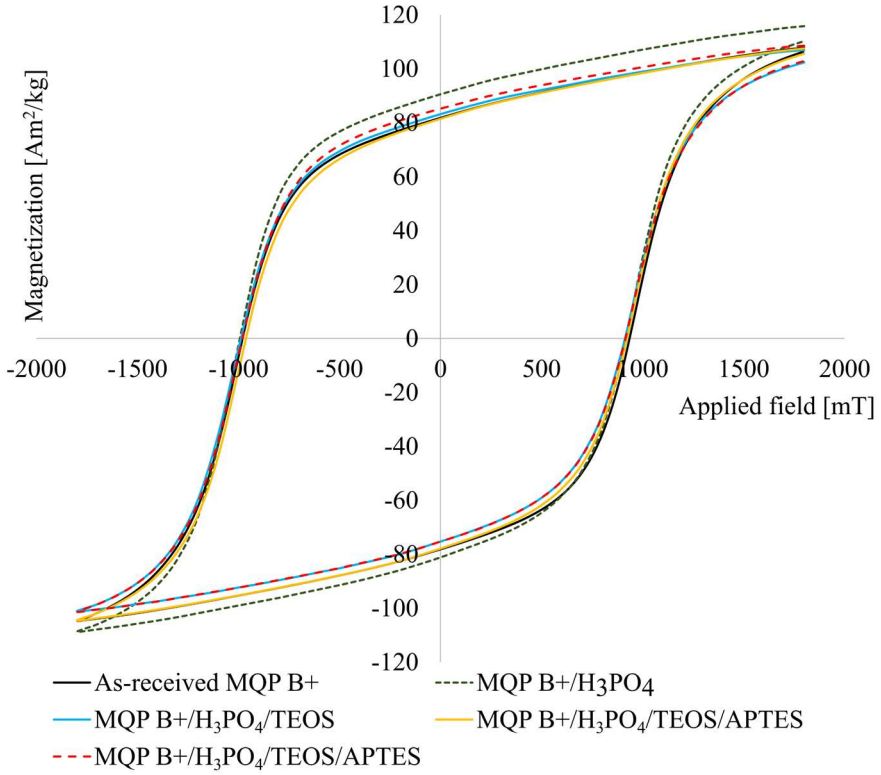

Figure 3-3: Hysteresis curves obtained via VSM measurements for the as-received and different batches of modified MQP B+ powder.

The advantageous effects of applying the powder coating are depicted in Figure 3-4, which shows the TGA curves. It is evident that the initial weight gain began simultaneously for all samples and increased with temperature over time. The observed increase in the weight can be attributed to the formation of oxidation products during the measurement process. Notably, powders with distinct coating layers exhibited diverse behaviours. The TGA curve demonstrated the highest weight gain of 1.7% for the as-received powder. Conversely, the MQP B+/H_3PO_4/TEOS/APTES sample, where the powder was phosphatized to improve the adhesion of silane layers, followed by TEOS coating and subsequent grafting of APTES, exhibited the lowest weight gain of 0.7%. These findings suggest that this specific composite coating improves thermal stability for the Nd–Fe–B powders. Consequently, it was selected as the feedstock material for industrial-scale injection moulding, and the moulded samples were subsequently subjected to further evaluation.

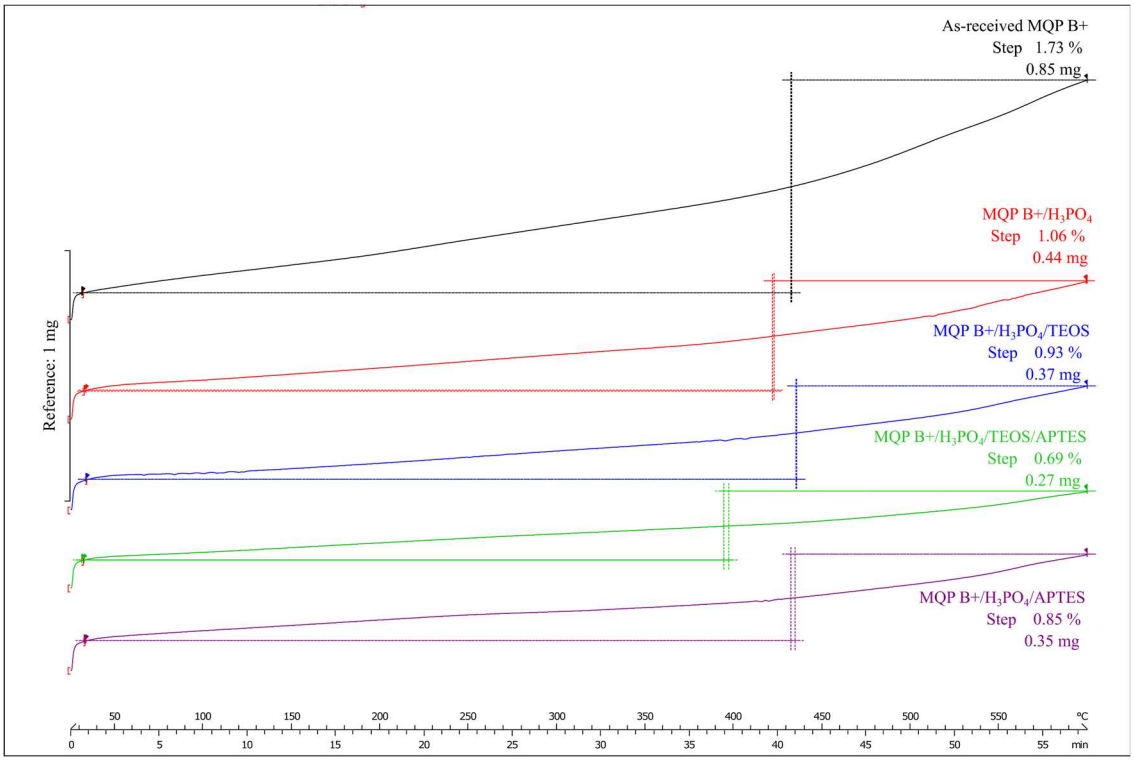

Figure 3-4: TGA curves illustrate weight gain (y-axis) over time with increasing temperature (x- axis) for different batches of MQP B+ powder. The bar represents a scale reference for the y- axis.

The morphologies and compositions of the as-received and modified MQP B+ powders were investigated using electron microscopy with chemical analysis (SEM-EDX). The SEM micrographs presented in Figure 3-5 highlight the effects of the melt-spun process, which resulted in the formation of irregularly shaped flake-like particles with noticeable melting traces and an uneven surface. The melt-spun process is followed by crushing, leading to the blocky morphology observed in the MQP B+ powder. To assess the elemental composition of the powders, the as- received samples and the modified MQP B+ powder were compared. As indicated by the elemental distribution in Table 3-2, there is a minor presence of P, N, and Si on the surface of the modified MQP B+ powder, originating from the coating layers.

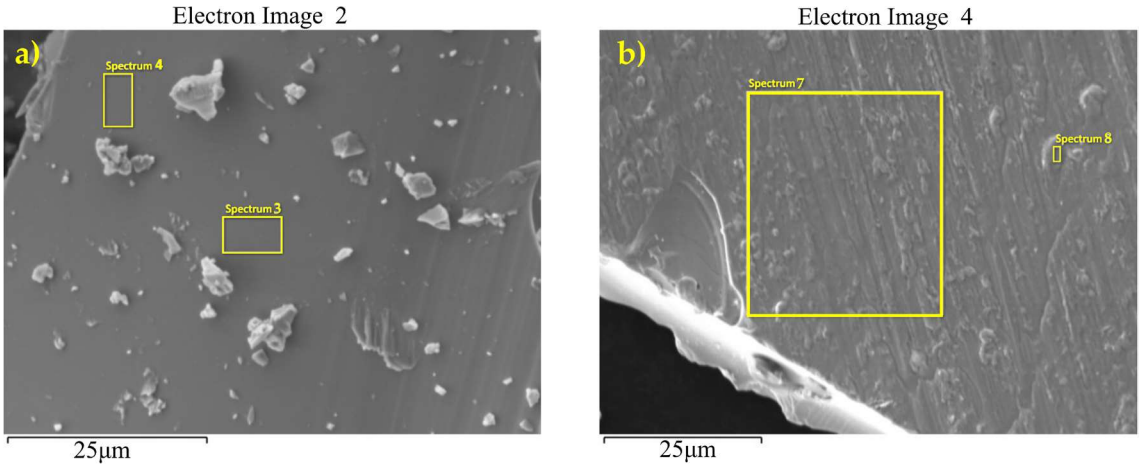

Figure 3-5: SEM images comparing as-received MQP B+ (a) and modified MQP B+ (b) powder. Areas where EDS analysis was conducted are denoted by enumerated rectangles; the results are given in Table 3-2.

Table 3-2: The elemental compositions (wt. %) of the as-received MQP B+ powder and modified MQP B+ powder were determined by EDX spectrum analysis (SEM images in Figure 3-6).

Spectrum label	As-received MQP B+ powder		Modified MQP B+ powder	
	Sp. 3	Sp. 4	Sp. 7	Sp. 8
Nd	28.2	28.0	28.0	27.4
Fe	65.5	65.5	63.5	63.9
Co	5.3	5.5	5.5	5.4
O	1.0	1.0	2.0	2.3
P	/	/	0.3	0.3
Si	/	/	0.5	0.6
N	/	/	0.2	0.1
Total	100.0	100.0	100.0	100.0

3.3.2 Injection-moulded magnets characterisation

The results of the magnetic measurements are summarized in Table 3-3. The intrinsic characteristics of the material, such as the coercivity, are influenced by the composition of the initial material. The obtained H_{ci} values for injection-moulded cylinders align with those of the as-received powder. For the 65% volumetric loading of the magnetic filler utilised in our study, the expected remanence value was 585 mT. The injection-moulded cylinders achieved 83% of their theoretical B_r values. However, it should be noted that polymer binders are typically used in the form of pellets during the manufacture of magnets in an industrial setting. The lower B_r values observed in this study may be attributed to the suboptimal parameters employed for injection moulding using powdered polymer binder. The coating layers did not diminish the magnetic properties, as evidenced by the VSM hysteresis analysis of the modified and as-received powders (Figure 3-3). The remanence (B_r) and energy product (BH_{max}) remained similar for both the modified and non-modified batches, providing further confirmation from previous VSM measurements.

Furthermore, as mentioned earlier, test dog-bone-shaped tubes produced from the MQP B+/PA12 batch exhibited defects and were unsuitable for mechanical testing. Owing to the lack of optimisation in the injection moulding process, the production of defect-free test dog-bone-shaped tubes from the unmodified material failed. Conversely, the successful manufacturing of such tubes was achieved with the modified material, supporting the notion that the surface treatment of powders enhances powder fluidity by reducing the friction between the magnetic powder and the polymer, which is aligned with the previous study [58].

Table 3-3: Measured magnetic properties of injection-moulded samples (with a minimum of three samples per measurement).

Batch	B_r [mT]	H_{ci} [kA/m]	BH_{max} [kJ/m^3]
As-received MQP B+	895-915	716-836	126-134
MQP B+/PA12	486 ±1.3	719 ±2	39.3 ±0.2
Modified MQP B+/PA12	487.6 ±0.8	727.2 ±2	39.3 ±0.2

The surface characteristics of the injection moulded cylinders from both batches are depicted in Figure 3-6, revealing no apparent contrast between the two. Notably, the homogeneity and distribution of magnetic particles within the polymer matrix were remarkably similar. The elemental compositions (wt.%) of the major elements detected on the surfaces of the magnetic powders and polymer in the cylinders are presented in Table 3-4 and Table 3-5. In Table 3-5, the absence of Si and P on the magnetic component surface, compared to their presence on the polymer surface in the polymer matrix, suggests the incorporation of some coating material into the polymer matrix throughout the moulding process. The concentrations of Nd and Fe in the magnetic portion of the cylinders in both batches were comparable. A higher concentration of C suggests that applying the coupling agent TEOS and the subsequent grafting of APTES onto the TEOS layer improved the adhesion between the modified magnetic powder and the polymer matrix. As a result, the higher carbon concentration primarily originates from the polymer matrix that encapsulates Nd–Fe–B particles.

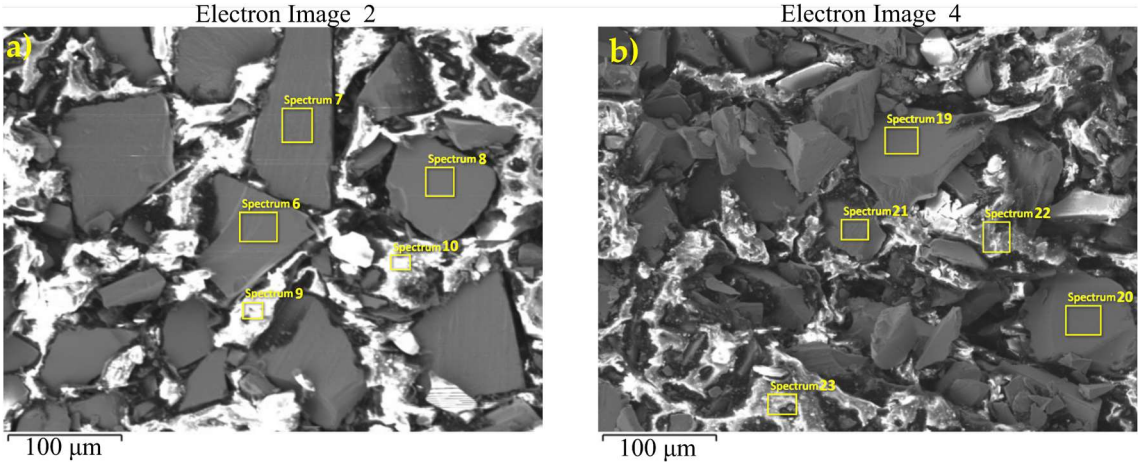

Figure 3-6: SEM images of the injection-moulded cylinders produced from as-received (a) and modified (b) MQP B+ powder, both bonded with PA12. Areas where EDS analysis was conducted are denoted by enumerated rectangles; the results are given in Table 3-4 and Table 3-5.

Table 3-4: The elemental compositions (wt.%) of the injection-moulded (IM) cylinders produced from as-received MQP B+ powder, bonded with PA12 (SEM image in Figure 3-6a).

Spectrum label	MQP B+ powder in IM cylinder			PA12 matrix	
	Sp. 6	Sp. 7	Sp. 8	Sp. 9	Sp. 10
C	4.5	5.0	4.7	18.4	72.8
O	1.2	1.5	1.4	2.5	4.4
Fe	62.2	61.8	62.1	51.6	14.8
Co	5.0	5.2	5.1	4.3	1.1
Nd	27.1	26.5	26.7	23.2	6.9
Total	100.0	100.0	100.0	100.0	100.0

Table 3-5: The elemental compositions (wt.%) of the injection-moulded (IM) cylinders produced from modified MQP B+ powder bonded with PA12. (SEM image in Figure 3-6b).

Spectrum label	Modified MQP B+ powder in IM cylinder			PA12 matrix	
	Sp. 19	Sp. 20	Sp. 21	Sp. 22	Sp. 23
C	7.5	7.1	9.5	68.7	72.6
O	2.6	2.2	2.1	5.1	8.9
Si	/	/	/	0.7	0.5
P	/	/	/	1.0	0.6
Fe	58.8	59.6	58.5	15.8	11.8
Co	5.0	5.1	4.6	1.1	/
Nd	26.1	26.0	25.4	7.6	5.6
Total	100.0	100.0	100.0	100.0	100.0

3.3.3 Mechanical properties

The obtained mechanical test results, as depicted in Figure 3-7, clearly indicate the effectiveness of the silane coating layers in improving the mechanical properties of the injection-moulded dog-bone-shaped tubes. Specifically, the modified MQP B+/PA12 batch exhibited significantly higher tensile strength, elongation at break, and elastic modulus, with improvements of 62%, 16.7%, and 19.9%, respectively, when compared to the MQP B+/PA12 batch. Moreover, the modified batch also demonstrated a noteworthy 51.9% increase in flexural stress during flexural testing. These results validate the successful enhancement of molecular interaction between the inorganic component (Nd–Fe–B) and the organic component (PA12) through three-step modification.

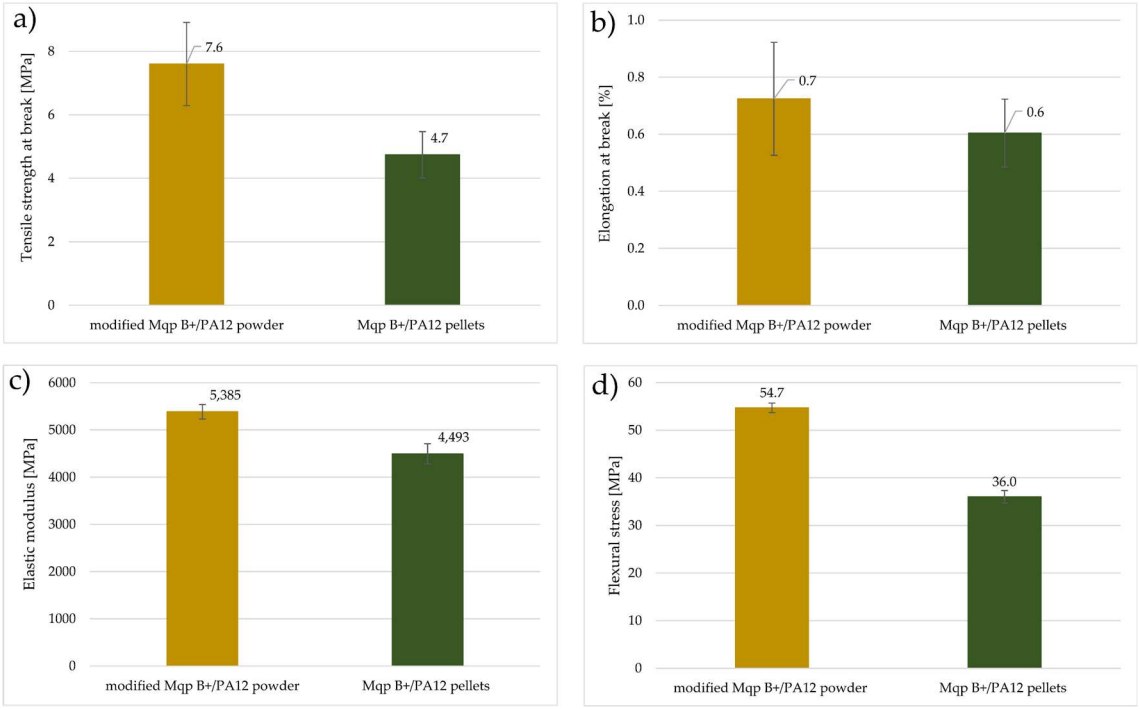

Figure 3-7: Results of tensile testing for modified MQP B+/PA12 powder and MQP B+/PA12 batches: (a) Tensile strength at break (MPa), (b) Elongation at break (%), (c) Elastic modulus (MPa), and (d) Flexural testing.

3.3.4 Environmental stability and corrosion resistance

Flux loss in magnetic materials can be divided into reversible, recoverable irreversible, and structural loss. Reversible flux loss, highly dependent on temperature, can be reverted by cooling the magnet, while irreversible flux loss involves persistent changes that do not revert to their initial state even after removing the perturbing factor. The reversible and irreversible flux losses were assessed on injection-moulded cylinders of modified MQP B+/PA12 and MQP B+/PA12 batches. These cylinders were exposed to four distinct scenarios; the results are presented in Table 3-6. The flux loss over 2000 h in this corrosive environment is depicted in Figure 3-8. Figure 3-9 provides a graphical representation of the flux loss as a function of time exposure to temperature shocking in air over 900 h. The observed slight increase in flux loss after 300 h aligns with the ± 1% precision of the Helmholtz coil measurement, underscoring the material's thermal stability (Figure 3-9). This change confirms the material's capacity to sustain a stable magnetic domain arrangement even under sustained thermal stress. The conditions of water immersion, BCT, and temperature shocking resulted in acceptable flux loss values for both batches. Interestingly, the batch of modified MQP B+/PA12 showed no irreversible flux loss in all three tests, while the MQP B+/PA12 batch showed minor irreversible flux loss of 0.5% in water immersion and 1.5% in temperature shock. This suggests that injection-moulded magnets made from MQP B+ bonded with PA12 are well-suited for applications that involve water immersion or diverse temperature conditions in dry air. Additionally, utilizing modified powder can extend the magnet's lifespan due to reduced flux loss. This correlates with TGA results, which reveal better oxidation resistance for modified powder than as received MQP B+.

However, a significant flux loss was noted in the test scenario involving immersion of the cylinders in corrosive water at 95 °C for 2000 h. Both batches exceeded the 5% flux loss limit, indicating the unsuitability of these magnets for applications involving aqueous media containing salts. A significant highlight is that the batch made from modified MQP B+ showed lower flux loss than that made from as-received powder. This indicates that the anti-oxidation property can be improved by treating the magnetic powder with phosphoric acid before applying silane treatment using TEOS and subsequent grafting of APTES.

Table 3-6: Overview of different environmental stability tests to which modified MQP B+/PA12 and MQP B+/PA12 batches were exposed.

Test name	Test temperature/Duration	Sample name	Reversible flux loss [%]	Irreversible flux loss [%]	Rusting
Immersion in water	120 °C/2000 h	Modified MQP B+/PA12	0.7	0	Low
		MQP B+/PA12	2.9	0.5	Low
Immersion in corrosive water	95 °C/2000 h	Modified MQP B+/PA12	9.8	5.9	Severe
		MQP B+/PA12	12.1	7.4	Severe
Bulk corrosion test	120 °C/96 h	Modified MQP B+/PA12	1.5	0	Severe
		MQP B+/PA12	2.0	0	Severe
Temperature shocking	-40/140 °C/2000 h	Modified MQP B+/PA12	0.4	0	Low
		MQP B+/PA12	2.9	1.5	Low

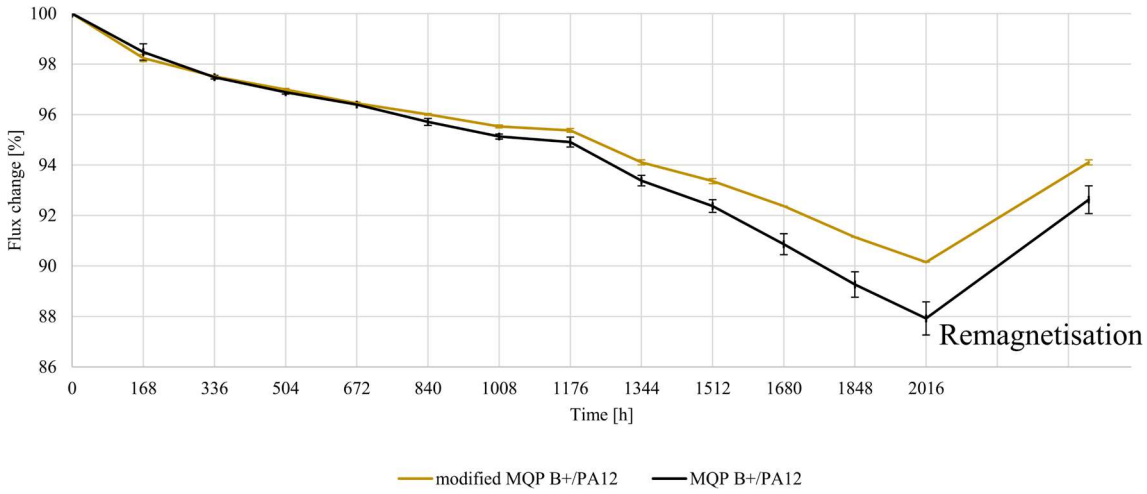

Figure 3-8: Flux loss of injection-moulded cylinders versus time exposure to corrosive water at 95 °C for 2000 h and after final remagnetisation.

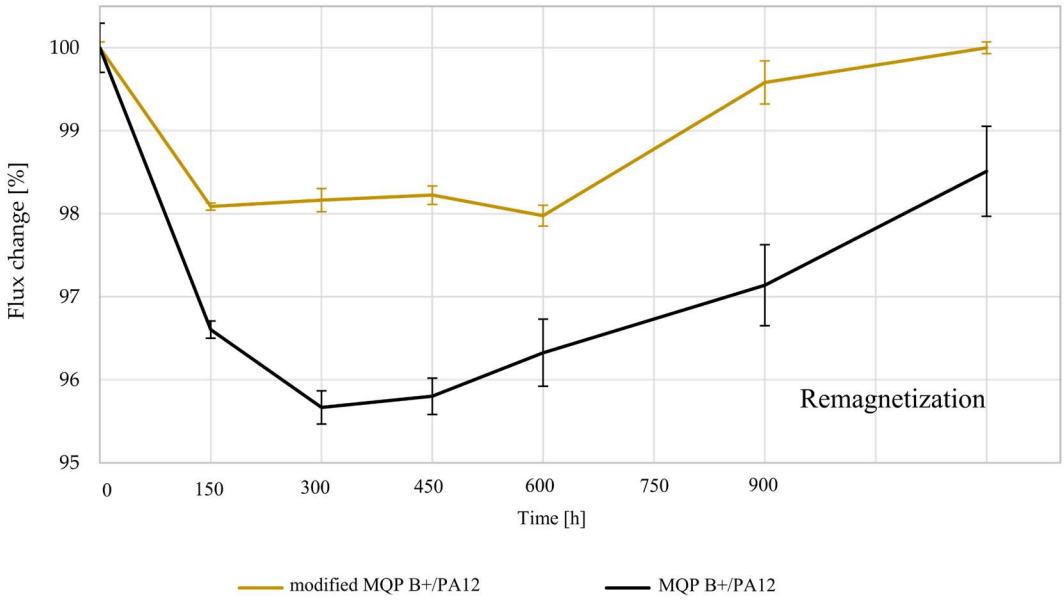

Figure 3-9: Flux loss of injection-moulded cylinders versus time exposure to temperature shocking on air, to temperatures ranging from −40 °C to +140 °C, for a total of 900 h.

3.4 Conclusions

The main objective of this study was to evaluate the three-step surface modification on magnetic powders and the mechanical properties and corrosion resistance of polymer-bonded magnets. The FTIR and SEM-EDX analyses confirmed the successful coverage of the silane coating on the surface of the modified MQP B+ powder, as indicated by the presence of stretching vibrations associated with Si–O–Si and Si–O–C bonds, and the detection of Si, N, and P elements. Furthermore, VSM measurements demonstrated that

the presence of the coating layer did not diminish the magnetic properties of the modified powder.

The modified bonded magnets exhibited lower irreversible flux loss than the non-treated batch in various environments, including water immersion at higher temperatures, exposure to pressurized steam during the BTC test, and temperature shock. However, a significant flux loss was observed when the cylinders were immersed in corrosive water, exceeding the 5% flux loss limit for both batches. These findings suggest that applying a composite silane coating to MQP B+ powder can result in minimal or reduced flux loss in applications involving water immersion or diverse temperature conditions in dry air, compared to non-treated MQP B+ magnets.

Regarding mechanical properties, the flexural and tensile test measurements demonstrated that the presence of the silane coating significantly increased the flexural and tensile strength of the modified bonded specimens.

In summary, applying a silane coating on the magnetic filler successfully enhanced the adhesion between the filler and polymer in the polymer matrix and improved corrosion resistance. The modified bonded magnets demonstrated lower irreversible flux loss and enhanced mechanical properties compared to the non-treated material.

Chapter 4

Dry Coupling Agent

Publication II
A. Damnjanović and N. Kovačević, "Influence of Magnet Particle Shape on Magnetic and Environmental Stability of FDM Polymer-Bonded Magnets," Materials, vol. 16, no. 8, p. 2993, Jan. 2023, doi: https://doi.org/10.3390/ma16082993

4.1 Introduction

Permanent magnets based on rare-earth materials are an indispensable component of modern technology. Not only do they provide higher-energy products than alnico or ferrite magnets, but they are also able to achieve this with less volume. They are the core of green technologies, such as hybrid and electric vehicles and wind turbines. Permanent magnets are most commonly manufactured using formative technologies, where magnetic powders can be compacted by sintering. Sintered magnets are known for their high-energy products but are prone to corrosion. Polymer-bonded magnets can be formed by applying pressure and high temperatures to the feedstock material by compression moulding, extrusion, injection moulding, or calendering processes. The feedstock material consists of a magnetic powder and a polymer binder. PBMs have some advantages over sintered magnets, as they can be easily fabricated into a near-net shape and have good mechanical properties. However, owing to the presence of the polymer, the magnetic properties of PBMs are lower than those of sintered magnets. A decrease in the remanence and energy of the product is linked to the amount of polymer used, as well as to the presence of pores and internal magnetic shear loss [1].

The major advantage of compression moulding is that it allows for a high magnetic filler loading. In the case of epoxy-bonded Nd–Fe–B magnets, the loading of the magnetic filler can be up to 98.5 wt.%. However, a disadvantage of compression moulding is that only simple geometries can be produced. On the other hand, injection moulding can produce complex shapes, although it requires specific tooling, which is costly [101]. Additive manufacturing technologies are promising solutions for overcoming the problem of expensive tooling. AM is a technology in which the desired shape is achieved by the successive addition of feedstock material, usually in a layer-by-layer manner [16]. With AM technology, there is great freedom in producing complex geometries, which enables the production of lighter parts. In the automotive industry, this feature is extremely important from both the environmental and economic perspectives. With lighter vehicles, fuel consumption and carbon emissions are reduced. Another economic aspect is that in additive technologies, material is built up and not removed, resulting in reduced material

consumption. This is particularly significant for critical raw materials, such as magnetic powders based on rare-earth elements.

Material extrusion is by far the most commonly used AM technology. Common names include fused deposition modelling and fused filament fabrication. In FDM, the feedstock material is in the form of a thermoplastic filament. The filament is loaded into the extruder, where it is heated, melted, and deposited through the nozzle head on the printer bed. Initially, filaments were made from various thermoplastic polymers. For instance, studies have been conducted on optimizing printing parameters to achieve tailored mechanical properties of composites based on polylactic acid and thermoplastic polyurethane [102], [103]. Furthermore, the utilisation of statistical evaluations to optimize process parameters for thermoplastic polymers can lead to achieving the best objective function [104]. Adopting a statistical approach in this regard can offer a time-saving advantage compared to experimental approaches. In recent years, FDM objects have been successfully printed using filaments made from composites, metals and alloys, ceramics, concrete, and biomaterials [15]. Magnetic fillers in PBMs can be bonded with various polymers depending on the final application. To date, FDM magnets have been printed in which an Nd–Fe–B powder is bonded with polyamide 11 [105], polyamide 12 [35], polyphenylene sulfide [39], ethylene ethyl acrylate [106], thermoplastic polyurethane [38], and polyether ether ketone [40]. The filament was also manufactured from a multicomponent system of polyoxymethylene as a dominant binder, mixed with spherical Nd–Fe–B powder and compounded Nd–Fe–B/polyamide 12 pellets [42]. Besides filaments, PBM can be extruded from slurries made of thermosetting epoxy resin [33]or photopolymer resin [107]. In this case, the FDM printing is coupled with UV curing. The manner in which the filaments are fused layer by layer causes most FDM objects to be anisotropic and not fully dense. Typically, there is a weaker bond and strength along the plane of the layer interface on a printed object [34].

The manufacturing of filaments is one of the greatest challenges in FDM. The filament for FDM needs to be extruded within a certain diameter and ovality tolerance to be printable at a constant flow rate over time. The filament needs to be stiff yet flexible enough to be spooled during filament production and despooled during printing. Finally, it must be homogenous. A complex filament production process can be avoided in big-area additive manufacturing (BAAM). BAAM is a material extrusion-based AM technology that uses pre-compounded materials in the form of pellets. BAAM is intended for printing very large objects, has a lower resolution, and is expensive. BAAM-printed Nd–Fe–B/polyamide 12 magnets exhibit better magnetic properties than injection-moulded magnets [35].

An important characteristic of PBMs, in addition to having a high remanence and energy product, is their long-term stability and their ability to resist demagnetisation, which consequently affects magnet performance during operation. Exposure to high temperatures or environmental degradation by corrosion leads to demagnetisation. It is certainly important to consider corrosion resistance when selecting PBMs for use in harsh environments, especially in the automotive industry, where components are subjected to a wide range of conditions.

In addition, there is an interference adhesion problem. Conventional methods to improve adhesion in polymer-bonded magnets include the surface treatment of the magnetic powder. For instance, passivation pre-treatment, such as phosphatising [55] or chromatisating [90], followed by coating magnetic powders in an aqueous solution of silanes [54], [55], [82], [90]. These processes are performed via wet chemistry routes, which can be time-consuming and challenging to apply on a production scale. In this study, to improve the adhesion between the magnetic powder and the polymer binder, we decided to use all components in the same physical state.

We have investigated the influence of the magnetic particle shape as well as the magnetic filer fraction on the magnetic and mechanical properties and environmental stability of PBMs. To improve the adhesion between magnetic filler particles and polymer binder, all feedstock material was applied in powder form. Furthermore, alternative additive manufacturing was compared with the traditional production injection moulding technique.

4.2 Materials and Methods

4.2.1 Filament extrusion of Nd–Fe–B bonded with polyamide 12

Two commercial isotropic magnetic powders based on Nd–Fe–Co–B alloys were used for the FDM printing of the specimens. Both powders were provided by company Magnequench. MQP B+ powder (−150 mesh), based on a Nd–Fe–Co–B alloy, was produced using a melt-spinning process, generating particles with irregular flake-like morphology. MQP B+ powder has a particle-size distribution predominantly below 90 micrometers, denoted by the negative sign before "150 mesh", indicating that the powder particles were smaller than the mesh size. The MQP S powder, based on a Nd–Pr–Fe–Co–Ti–Zr–B alloy, was produced by gas atomisation; thus, the particles had a spherical morphology. The MQP S powder has a d_{50} value of 30–55 micrometers, signifying that half of the particles were larger than this range while the remaining half were smaller. MQP S, being less coarse, is suitable for manufacturing bonded magnets, particularly by injection moulding, extrusion, and calendering, owing to its superior flowability [108]. The properties of the Nd–Fe–B powders are summarized in Table 4-1. MQP B+ has higher initial magnetic properties, which makes it more attractive for certain applications despite its potentially lower flowability compared to MQP S. Polyamide 12, a polymer binder, was used in the powder form (Vestosint, Evonik, Pandino, Italy). Magnetic and polymer powders were used as received without preconditioning, in other words, without drying, sieving, magnetizing, etc.

Table 4-1: Magnetic properties of the as-received Nd–Fe–B powders (source material datasheet: https://mqitechnology.com/products/bonded-neo-powder).

Magnetic powder	Residual induction, B_r [mT]	Intrinsic coercivity, H_{ci} [kA/m]	Energy product, BH_{max} [kJ/m^3]
MQP S	730-760	670-750	80-92
MQP B+	895-915	716-836	126-134

The amount of Nd–Fe–B powder in the bonded magnet is directly responsible for its magnetic and mechanical behaviours of bonded magnets. However, a higher content of magnetic filler may change the rheology of the polymer melt during the process and subsequently affect the mechanical properties of the bonded magnets. That is why this study utilized two different polymer loadings of 7 and 10 wt.%.

Because of the poor adhesion between the inorganic filler and the organic polymer matrix, titanium triisostearoylisopropoxide (TTS, Ken-React® CAPOW® KR® TTS/H) was added to the filler as a powdered coupling agent. The role of TTS is to provide a molecular bridge at the interface between two substrates [109]. The magnetic filler was premixed in a kitchen blender with 1 wt.% TTS. After one minute of mixing, 0.2 wt.% zinc stearate (Sigma-Aldrich, St. Louis, MO, USA) and 0.5 wt.% stearic acid (Sigma-Aldrich) were

added and mixed for one minute. Because the former acts as an external lubricant, whereas the latter serves as an internal lubricant, they were added to reduce the powder surface friction and protect the extruder parts [110]. The final step involved blending a suitable amount of PA12 with a pre-prepared premix of magnetic powder and additives. The mixture was homogenized for two minutes.

Filament extrusion was achieved using a single-screw extruder (Linden IIKA). Inside the extruder vessel, there were double Z blades for kneading and homogenizing the material. The extruder was purged with a Dyna-Purge®E2 cleaning mass between batches to prevent contamination of the subsequent batch. The premixed filler, additives, and polymer were flood-fed into the vessel and kneaded for 30 min at temperatures between 185 °C and 200 °C. The feedstock material was mixed, melted, and extruded through a die with a diameter of 1.8 mm. The filament was cooled using compressed air at the conveyor belt. The diameter of the filament was manually measured with a calliper at the end of the conveyor belt. It was kept in the range between 1.7 and 1.8 mm by adjusting the speed of the conveyor belt. Table 4-2 provides a summary of four batches that were extruded into printable filaments, while Figure 4-1 depicts a schematic representation of the manufacturing process involved in the production of filaments and FDM printing.

Table 4-2: Composition of the prepared filaments.

Sample	Nd–Fe–B powder	Nd–Fe–B		PA12	
		[wt.%]	[vol.%]*	[wt.%]	[vol.%]
S90/10	Spherical	90	57.1	10	41.6
S93/7	Spherical	93	66.1	7	32.6
B90/10	Irregular shape	90	56.5	10	65.5
B93/7	Irregular shape	93	42.2	7	33.2

*Including added additives and excluding estimated void of 1.3%.

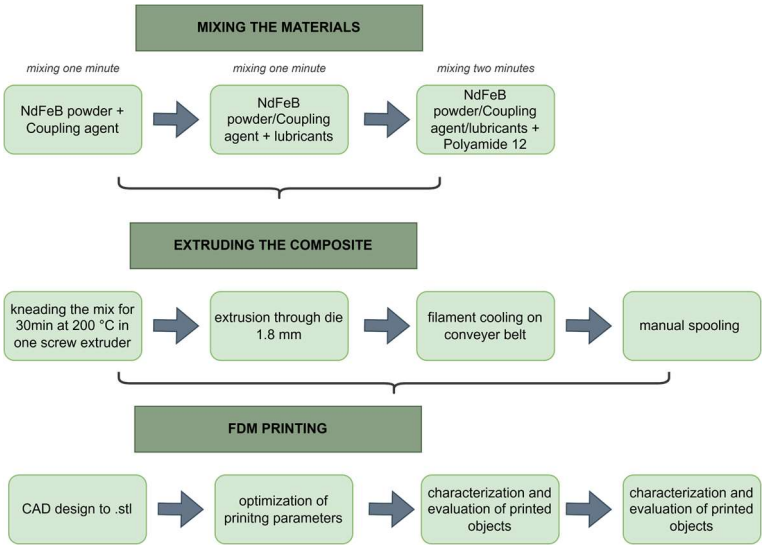

Figure 4-1: Schematic representation of the production processes for filaments and FDM printing.

4.2.2 Additive manufacturing of permanent magnets

In FDM printing, nozzle clogging can lead to interruptions in the printing process, rendering it impossible to clean the nozzle and resume printing on the same sample. This issue is particularly pronounced when dealing with highly filled filaments, such as those utilized in our study. As a result, our foremost goal was to ensure the uninterrupted printing of each sample. Therefore, the determination of printing parameters was driven by the need to sustain continuous FDM printing while avoiding any nozzle-clogging complications. For the FDM extrusion of the bonded magnets, a commercial desktop Craftbot Flow XL 3D printer was used. The filaments were extruded at 250 °C, and the printing speed was 10 mm/s. The printing platform was heated to 70 °C to ensure additional adhesion of the extruded material. To avoid clogging during material extrusion, a nozzle head with a 0.8 mm diameter was chosen. The height between the nozzle head and the printing bed was set to 0.2 mm. The samples were printed in the shape of cylinders (10 mm × 7 mm). All specimens were printed horizontally on the building platform with a raster angle of +45°/−45° in alternate layers and 100% infill density. Cylinders were printed with two different layer thicknesses, 0.1 and 0.2 mm, to evaluate the influence of the layer thickness on the final density and porosity of the printed samples. Table 4-3 presents an overview of the essential printing parameters employed for fabricating each sample, while Figure 4-2 depicts the spooled filaments and the printed samples.

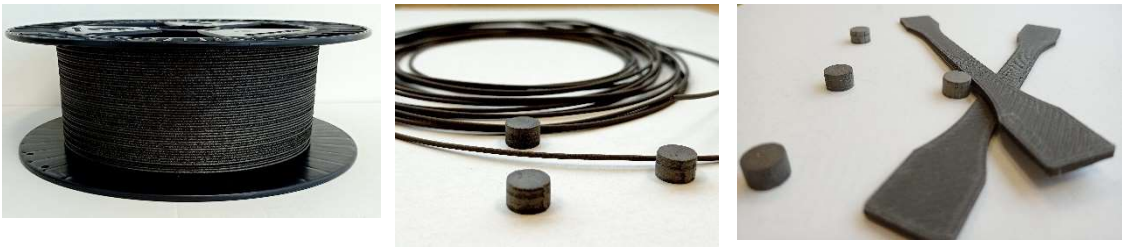

Figure 4-2: Extruded filament for FDM and FDM-printed samples in the form of cylinders and dog-bone-shaped test tubes.

Table 4-3: Overview of printing parameters.

Printing parameter	Value [unit]
Nozzle temperature	250 °C
Printing speed	10 mm/s
Platform temperature	70 °C
Nozzle head diameter	0.8 mm
Raster angle	+45°/+45°
Infill density	100 %
Layer thicknesses	0.1 mm
	0.2 mm

4.2.3 Injection moulding of Nd–Fe–B bonded with polyamide 12

Feeding pellets for injection moulding (IM) were made from filaments by crushing them into 5 to 10-mm pieces. The injection-moulded magnets were manufactured using Krauss Maffei KM50-190 at the manufacturing facilities at Kolektor KFH (Slovenia). The temperature range in the injection moulding unit ranged from 230 °C to 295 °C, with the pressure varying from 804 to 868 bar.

4.2.4 Characterisation

Scanning electron microscopy coupled with energy dispersive X-ray analysis (JSM-IT300, JEOL SEM equipped with Oxford EDX at 15 keV energy beam) was used to analyse the shape and elemental composition of the as-received Nd–Fe–B powders. SEM images of the filaments were used to analyse the distribution of the filler particles in the polymer matrix. EDX was used to determine the elemental composition of the filaments and at the fracture of broken dog-bone-shaped tubes made from filament S90/10.

To evaluate the temperature stability and filler content in the filaments, thermogravimetric analysis was performed using TGA/DSC 1 (Mettler-Toledo GmbH, Ljubljana, Slovenia). The filament samples were heated in air to 600 °C at a heating rate of 10 °C/min.

Differential scanning calorimetry was used to evaluate the thermal stability of filaments and the influences of additives and fillers. The tested samples were heated and cooled in a thermal analyser apparatus (Mettler Toledo DSC1 STARe System). The first cooling run and second heating run were evaluated. The samples were heated from 25 °C to 480 °C at a rate of 10 °C/min in an air atmosphere to determine melting behaviour. The cooling cycle run between two heating cycles, from 200 °C to 30 °C at a rate of 10 °C/min in an air atmosphere, was carried out to determine cold crystallisation. The degree of crystallinity, X_c [%], was calculated based on the formula:

$$X_c = \frac{\Delta H_m}{(1 - w_f) \times \Delta H_0} \times 100, \tag{4.1}$$

where ΔH_m [J/g] is the melting enthalpy of filaments after the second heating, w_f is the weight fraction of the filler [%], and ΔH_0 [J/g] is the melting enthalpy [J/g] of 100% crystalline PA12 (245 J/g [38], [111]).

The rheological properties of the filaments were evaluated by measuring the melt flow index (MFI; LMI5000 Series, Dynisco). The filaments were cut into granules, and 30 g of each batch was fed into an MFI capillary and preheated to 260 °C. The melt time was set to 120 s, and a 5 kg load was applied.

The density of the printed cylinders was measured based on Archimedes' principle using an analytical balance (XP205 by Mettler-Toledo GmbH). The measured densities were compared with the expected calculated densities. The expected density was calculated using the rule of mixtures, excluding void formation:

$$\rho_{calculated} = \frac{\rho_{filler} \times vol\%_{filler} + \rho_{add1} \times vol\%_{add} + \rho_{add2} \times vol\%_{add2} + \rho_{add} \times vol\%_{add3} + \rho_{polymer} \times vol\%_{polymer}}{100}, \tag{4.2}$$

where labels add_1, add_2, and add_3 refer to the following additives: coupling agent, internal lubricant, and external lubricant, respectively.

Porosity was evaluated using the following equation:

$$Porosity(\%) = \frac{\rho_{calculated} - \rho_{measured}}{\rho_{calculated}} \times 100, \quad (4.3)$$

FDM-printed cylinders were magnetized using an impulse magnetizer K-Series (MAGNET-PHYSIK) at a voltage of 2000 V to saturate the samples. After magnetisation, the residual remanence and intrinsic coercivity were measured using a permeameter (PERMAGRAPH®, MAGNET-PHYSIK). The measured residual remanence was compared with the theoretical value. The theoretical value of B_r was calculated using the following formula:

$$Br_{theorethical} = \frac{vol\%_{filler}}{100} \times Br_{as-received\ powder} \quad (4.4)$$

The magnetic flux was measured using a Helmholtz coil (MS 75 with electronic Fluxmeter EF 14, MAGNET-PHYSIK) before and after exposure to different environmental tests.

4.2.5 Environmental stability

The environmental stability of FDM-printed PBMs was studied using potential environmental stresses, i.e., accelerated hot aqueous immersion, dry heat, and cyclic temperature–humidity corrosion tests. The goal of these tests was to evaluate the effects of moisture, the presence of aggressive ions, and temperature on the flux loss. Tests were performed with at least three samples.

Cylinders from batches B93/7 and S93/7, with a layer height of 0.1 mm, were immersed in deionized water at 85 °C for 1000 h to evaluate the influence of water absorption on flux loss. Cylinders from batches B90/10 and S90/10 with layer heights of 0.1 mm were immersed in corrosive water at 95 °C for 1000 h. A solution of corrosive water was prepared according to the standard ASTM D1384 [97]. Sodium salts were dissolved in 1 L of deionized water. The exact amount of sodium salts can be found in Table 4-4.

Table 4-4: Chemical composition of the corrosive water solution.

Compound	Concentration [mg/L]
Na_2SO_4	148
NaCl	165
$NaHCO_3$	138

To evaluate the effect of hot air, cylinders from batches B93/7 and S93/7, with a layer height of 0.1 mm, were exposed to dry air at 85 °C for 1000 h. Cylinders from batches B93/7 and S93/7 with a layer height of 0.1 mm were subjected to the bulk corrosion test according to ASTM A1071/A1071M-11 [112]. In the BCT test, the samples were exposed to pressurized steam to determine their resistance to degradation by the combined action of heat and water vapour. The samples were placed on top of glass, filled with demineralised water, and then placed in autoclaves at 120 °C for 96 h. Water in the glass created 100% relative humidity at a pressure of 200 kPa. Four cylinders from batches B93/7 and S93/7 with a layer height of 0.2 mm were exposed to a humidity cyclic test according to IEC-60068-2-38 [113]. The samples were kept in the environmental chamber for 10 cycles, with each cycle lasting 24 h. The first five cycles were a cold phase with a low temperature of 10 °C, and the five following cycles did not include a cold phase at a high temperature of

+65 °C. The humidity cyclic test is an environmental test used to evaluate the performance of materials and components under conditions involving changes in temperature and humidity. The test is designed to simulate real-world conditions and identify defects that may be caused by "breathing", which is the movement of air or moisture in and out of a material or component. This can occur when the temperature on the surface of the material is lower than the dew point, resulting in condensation. As the temperature changes, the air inside the material expands and contracts, which can cause air or moisture to enter through the cracks or gaps. Over time, this can lead to water accumulation inside the material, potentially causing damage or failure.

The magnetic flux was measured using a Helmholtz coil before testing. The magnets were moved and cooled at the end of each test, and the reversible flux loss was measured. The samples were saturated again to determine the irreversible flux loss, and the flux was measured.

4.3 Results and Discussion

4.3.1 As-received magnetic powder characterisation

The morphology of the as-received MQP S and MQP B+ powders was examined using SEM. The SEM micrographs in Figure 4-3 show the effects of the different manufacturing methods. The melt-spun process produced irregularly shaped flake-like particles. The melt-spun process is followed by crushing; therefore, the MQP B+ powder has a blocky morphology. Gas atomisation produces spherical particles with smooth surfaces. For the MQP B+ powder, a brittle nature can be observed. The SEM micrographs in Figure 4-3 show filler particles inside the polymer matrix in filaments. In filament B90/10, few MQP S particles were observed because of the difficulty in thoroughly cleaning the extruder. In the subsequent subsection, the elemental composition of the as-received powders is discussed and compared with the elemental composition obtained for the magnetic portion of the filament.

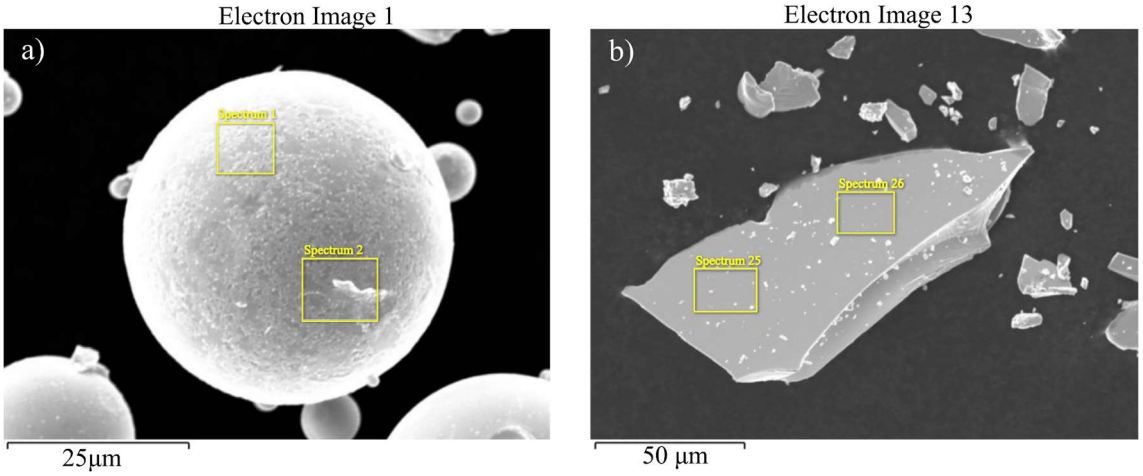

Figure 4-3: SEM micrographs of the as-received MQP S particles (a) and MQP B+ particles (b).

4.3.2 Filaments characterisation

The surface features of filaments S90/10 and B90/10 are shown in Figure 4-4, indicating a contrast between the two. The former exhibits a relatively smoother surface texture owing to the finer magnetic particles used in its production. Conversely, the latter presents a more pronounced ''shark skin'' appearance attributed to using coarser magnetic particles. Table 4-5 and Table 4-6 show the elemental compositions (wt.%) of the major elements detected at the surface of the as-received powders and filaments S90/10 and B90/10. The concentrations of Nd and Fe in the magnetic part of the filament were lower than those in the starting alloy, and the concentration of C was high. A high concentration of C could mean that the coupling agent TTS improved the adhesion between the filler and the polymer. Thus, a high C concentration originates from the polymer that encapsulates the Nd–Fe–B particles.

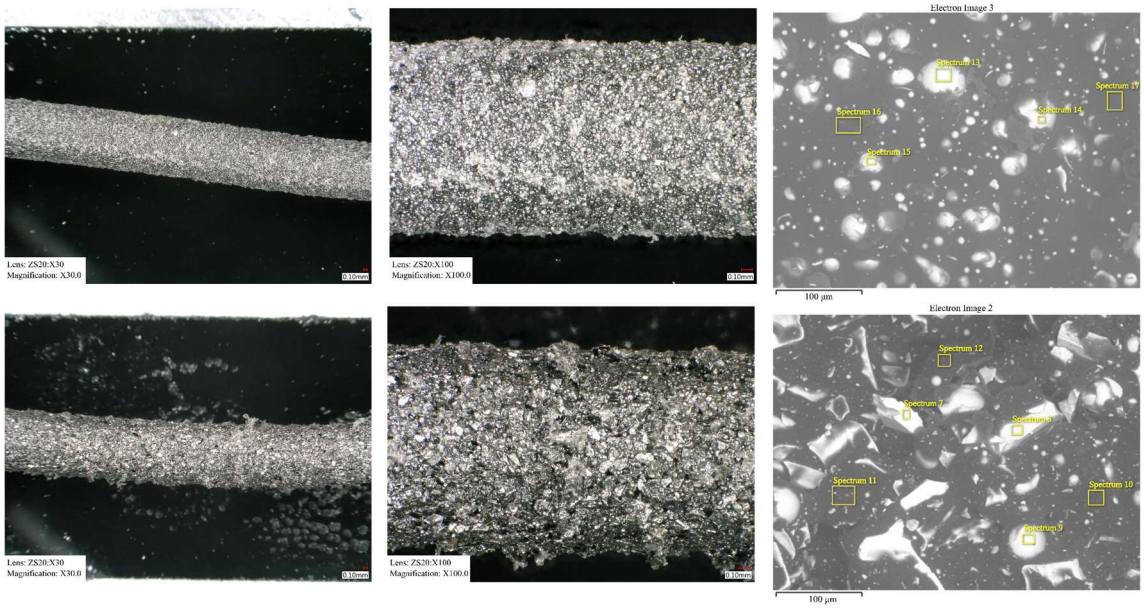

Figure 4-4: SEM micrographs of filament S90/10 (a) and filament B90/10 (b), showing Nd–Fe–B particles dispersed in the polymer matrix.

Table 4-5: Elemental composition (wt.%) of the as-received MQP S powder and filament S90/10.

Spectrum label	As-received MQP S powder		MQP S powder in filament 90/10			PA12 matrix in filament S90/10	
	Sp. 1	Sp. 2	Sp. 13	Sp. 14	Sp. 15	Sp. 16	Sp. 17
Fe	71.0	73.7	27.1	26.1	26.2	8.4	6.9
Nd	17.3	17.2	7.0	6.9	6.5	2.3	1.8
C	/	/	56.6	57.6	58.1	75.8	77.5
O	/	/	6.4	7.0	6.6	12.3	12.7
Ti	2.3	2.1	0.9	0.9	0.9	0.5	0.4
Zr	6.4	3.8	2.0	1.5	1.7	0.7	0.7
Co	3.0	3.2	/	/	/	/	/

Total	100.0	100.0	100.0	100.0	100.0	100.0	100.0

Table 4-6: Elemental composition (wt.%) of the as-received MQP B+ powder and filament B90/10.

Spectrum label	As-received MQP B+ powder		MQP B+ powder in filament 90/10			PA12 matrix in filament B90/10		
	Sp. 25	Sp. 26	Sp. 7	Sp. 8	Sp. 9	Sp. 10	Sp. 11	Sp. 12
Fe	66.3	66.0	27.4	27.0	30.0	8.6	9.7	7.8
Nd	28.0	28.3	11.9	11.7	8.4	3.5	4.0	3.3
C	/	/	51.9	52.7	53.2	75.6	74.6	75.4
O	/	/	5.9	6.2	5.5	11.3	10.8	12.6
Co	5.7	5.7	2.3	2.2	1.3	0.6	0.6	0.6
Ni	/	/	0.4	/	/	/	/	/
Zr	/	/	0.2	0.2	1.6	0.4	0.3	0.3
Total	100.0	100.0	100.0	100.0	100.0	100.0	100.0	100.0

TGA analysis provided information on the mass reduction of the filament under a high-temperature condition. TGA analysis can be used to estimate the filler content in the filament, where the mass-loss percentage represents the degradation of the polymer. When filler loading was 93 wt.%, the expected mass loss would be 7%, and the same goes for filaments with 90 wt.%, for which the expected loss was 10%. However, Figure 4-5 shows that the loss is slightly higher and differs among the batches. The higher-than-expected mass loss can be attributed to the presence of additives, which also degrade to a certain extent. In addition, the higher mass loss suggests that the filler particles were partly degraded due to high temperatures.

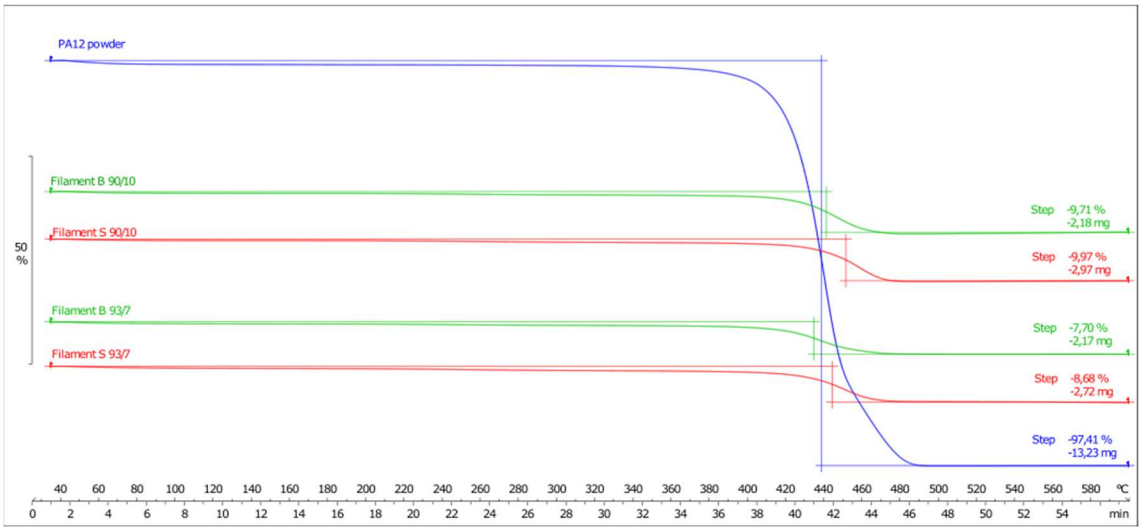

Figure 4-5: TGA curves after heating the filaments to 600 °C.

The filament's melting point was found to be approximately 177 °C through DSC analysis. This implies that FDM-printed magnets bonded with PA12 can withstand temperatures up to 170 °C. However, the operating temperature of printed magnets is contingent on their specific application and conditions, and it is restricted by the service temperature range of PA12, which is −40 °C to 80 °C, with short-term temperatures up to

110 °C. DSC data and the calculated degree of crystallinity are presented in Table 4-7, indicating that an increase in filler loading correlates with an increase in the degree of crystallinity and a decrease in melting temperatures. Furthermore, the data demonstrate a link between filler presence and the degree of crystallinity in FDM-printed specimens.

Table 4-7: DSC analysis on the filament samples. The table includes data on the melting temperature after first and second heating, T_{m1} and T_{m2}, respectively; enthalpy after first and second heating, ΔH_{m1} and ΔH_{m2}, respectively; cold crystallisation temperature, T_c, and enthalpy, H_c, after the cooling cycle; and the calculated degree of crystallinity, X_c.

Sample	T_{m1} (°C)	ΔH_{m1} (J/g)	T_c (°C)	ΔH_c (J/g)	T_{m2} (°C)	ΔH_{m2} (J/g)	X_c (%)
S90/10	177.7	6.1	149.7	6.0	176.1	5.3	21.6
S93/7	176.2	5.1	149.9	4.5	174.6	4.1	23.9
B90/10	176.8	5.5	149.4	5.9	175.9	5.3	21.7
B93/7	176.2	4.2	147.8	4.2	175.4	3.8	22.3

The MFI measurements, depicted in Figure 4-6, indicate that filaments with higher polymer content, such as S90/10 and B90/10, exhibit greater flowability than those with 7 wt.% of polymer binder. Hence, higher content of the thermoplastic binder leads to an increase in MFI values and improves fluidisation. Additionally, the filament made with spherical particles had more than double the MFI values. These results also support the suitability of MQP S powders for FDM printing, given their higher MFI values, which reduce the risk of printer head clogging. Consequently, using MQP S powder enables the printing larger and more complex-shaped samples.

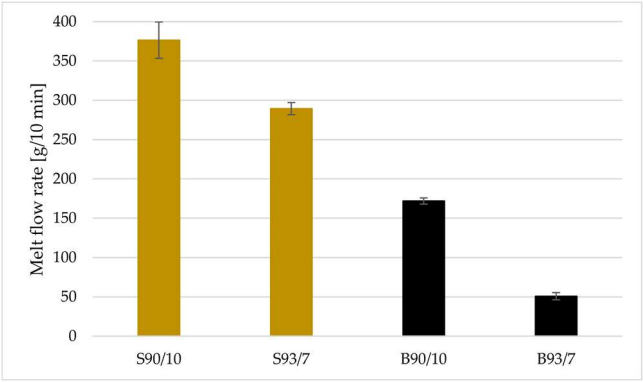

Figure 4-6: The melt flow index [g/10 min] of MQP S and MQP B+ filaments with various filler loadings.

4.3.3 Characterisation of the FDM-printed polymer-bonded magnets

Poor density and porosity are common characteristics of materials produced by any additive manufacturing technology. Figure 4-7 presents bar graphs displaying the densities and estimated porosity of injection-moulded and FDM-printed magnets. FDM-printed magnets exhibited the lowest density, primarily due to poor adhesion between extruded layers and the lack of high-pressure in the IM process that brings the material together. Porosity was estimated from measured and calculated densities. Porosity in magnets can cause internal oxidation of the magnetic powder by air or moisture trapped inside the

pores. Moreover, high porosity leads to low residual remanence due to low density. The measured density results reveal that samples printed with spherical powder have higher density and porosity values than those printed with irregularly shaped powder. Moreover, S90/10 and S93/7 samples with a layer thickness of 0.1 mm demonstrate higher density and lower porosity values compared to those with a layer thickness of 0.2 mm. These findings indicate that the shape and size of the powder particles, as well as the layer thickness, play a crucial role in the final density and porosity of FDM-printed samples.

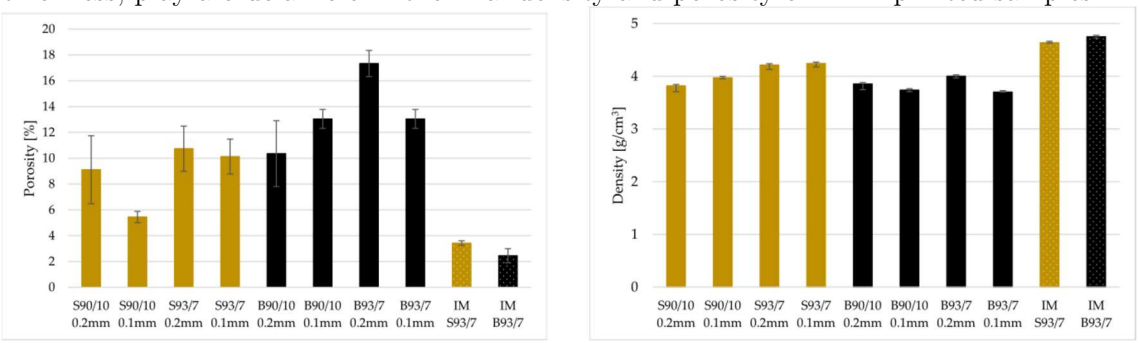

Figure 4-7: Bar charts of density and calculated porosity of FDM-printed magnets, with various filler loadings and printing heights, and injection-moulded magnets.

A dog-bone-shaped specimen (type 1 B) was printed using filament S90/10 by FDM printing in accordance with ISO 527-2 [24]. This type of specimen is commonly used in mechanical testing, specifically for flexural and tensile testing, in order to evaluate the strength and behaviour of the material under load. The flexibility of the material made it challenging to conduct mechanical tests, as the specimens did not break under an applied load of 10 kN. A flexible specimen is depicted in Figure 4-8.

Figure 4-8: Dog-bone-shaped specimen, FDM-printed from filament S90/10, fully bent without breaking.

A tensile test with the same specimens was repeated until the specimen broke. After the tensile test, the surface fracture of the specimen was examined using SEM/EDX. A SEM image of the specimen is shown in Figure 4-9. The carbon content values on powder particles, as determined through EDX analysis in Table 4-8, are consistent with the results obtained from the EDX analysis of the S90/10 filament from Table 4-5.

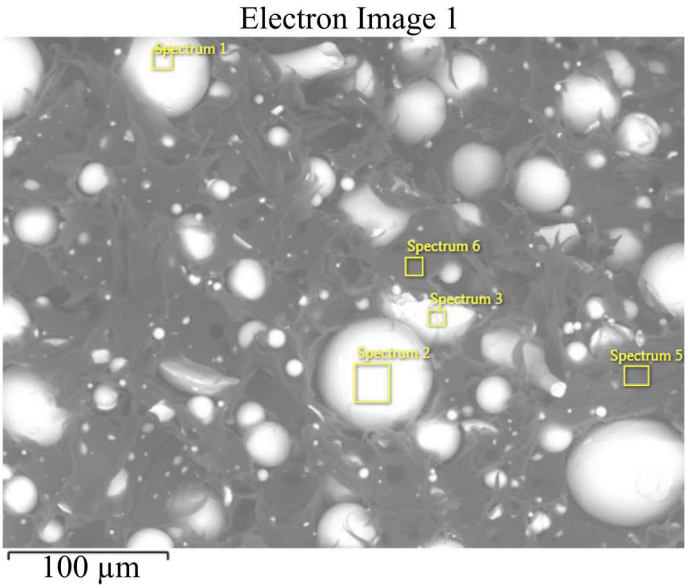

Figure 4-9: SEM image of surface fracture of the dog-bone-shaped specimen, FDM-printed from filament S90/10. Nd–Fe–B were pulled out of the polymer matrix.

Table 4-8: Elemental composition (wt.%) of the surface fracture of dog bone specimen made from filament S90/10.

Spectrum label	MQP S powder in Test Tube			PA12 Matrix in Test Tube	
	Sp. 1	Sp. 2	Sp. 3	Sp. 5	Sp. 6
Fe	38.3	39.8	38.5	17.3	19.1
Nd	10.4	10.4	10.0	4.7	5.2
C	43.2	42.5	44.7	68.0	66.7
O	4.3	3.6	3.5	8.1	7.2
Ti	1.2	1.3	1.2	0.8	0.7
Zr	2.6	2.4	2.1	1.1	1.1
Total	100.0	100.0	100.0	100.0	100.1

The magnetic properties of the samples were evaluated, and the results for at least three samples are summarized in Table 4-9. The expected lower Br values of FDM-printed samples due to their low density and high porosity were observed. However, considering the constraints of FDM printing technologies (lack of high pressure), extremely high Br values were obtained for the FDM-printed samples. The Br values of the FDM-printed samples were above 90% of the expected theoretical remanence for a filler loading of 90 wt.%. FDM magnets made from MQP S achieved a Br value of 98% for 93 wt.% filler loading, while those made from MQP B had 87%. The intrinsic properties of the material, such as coercivity, depend on the composition of the starting material and are not affected by the sample density. The Hci values of the as-received powder, as stated in MDS, are 716–836 kA/m for the melt-spun powder and 670–750 kA/m for the atomized gas. The Hci values of the FDM-printed samples were consistent with those of the as-received powder and the IM samples, indicating that no degradation of the magnetic powder occurred during filament manufacturing and FDM printing.

Table 4-9: Measured magnetic properties of FDM-printed and injection-moulded (IM) samples.

Sample	BH_{max} [kJ/m^3]	H_{ci} [kA/m]	$B_{r\ measured}$ [mT]	$B_{r\ theoretical}$ [mT]
S90/10 0.2 mm	18.7 (±0.9)	719.2 (±1.2)	347.8 (±0.4)	375.1
S90/10 0.1 mm	21.7 (±0.1)	721.8 (±1.2)	367.3 (±0.4)	375.1
S93/7 0.2 mm	28.9 (±1.1)	721.5 (±1.3)	422.2 (±7.9)	434.2
S93/7 0.1 mm	29.4 (±1.5)	721.3 (±2.6)	426 (±11.0)	434.2
B90/10 0.2 mm	27.3 (±0.4)	700.6 (±0.8)	410.8 (±3.4)	449.5
B90/10 0.1 mm	28.7 (±0.4)	712.2 (±1.3)	409.8 (±2.5)	449.5
B93/7 0.2 mm	35.5 (±1.0)	713.2 (±0.9)	456.5 (±6.8)	521.4
B93/7 0.1 mm	35 (±0.3)	705.8 (±1.0)	454.2 (±1.7)	521.4
IM S93/7	32 (±0.1)	710.8 (±1.1)	449 (±0.7)	434.2
IM B93/7	46.3 (±0.6)	697.7 (±1.0)	528.8 (±3.3)	521.4
S90/10 0.2 mm	18.7 (±0.9)	719.2 (±1.2)	347.8 (±0.4)	375.1

Total flux loss can be categorized into reversible loss, recoverable irreversible loss, and structural loss. Reversible flux loss occurs as a function of temperature and can be undone by cooling the magnet. Irreversible changes are those that do not return to their original value after the disturbing influence is removed. These can be further divided into those that can be restored by remagnetisation at room temperature, recoverable irreversible loss, and those that cannot, as a result of structural or metallurgical changes, often called ageing loss [114].

The reversible and irreversible flux losses were evaluated after exposing the magnets to different scenarios. It is likely that the magnets made from the gas-atomized powder experienced a lower flux loss because they had a higher density and lower porosity. This implies that if a magnet is more compact and has fewer gaps or voids, it has less possible routes for water or air entrapment. A higher density and lower porosity can lead to improved magnetic performance, resulting in lower flux loss. The rule of thumb in the industry is that magnets should not have flux loss higher than 5% over 1000 h of testing [35], [75]. Table 4-10 summarises the environmental tests performed to evaluate the stability of the magnets, as well as the final irreversible flux loss observed after testing. The results indicate that irreversible flux loss was less than 5% in all tests except for the test where FDM magnets were immersed in corrosive water. It is worth noting that this particular test is considered highly aggressive, and it is uncertain whether even IM magnets would have a flux loss of less than 5%. The flux loss of magnets produced using MQP S powder was lower than those made from MQP B+ when immersed in pure water, as shown in Figure 4-10. This difference may be attributed to the better bonding between magnet and polymer particles in the former. However, in corrosive water solution with aggressive ions at high temperatures, the presence of aggressive ions accelerates surface corrosion and flux loss, as depicted in Figure 4-11 and Figure 4-12, for both S90/10 and B90/10 magnets. Figure 4-13 shows a cross-section of the most corroded sample after the corrosive water test, which demonstrates the progression of corrosion in the FDM samples. Sample B90/10 had a significantly higher depth of corrosion, nearly double that of S90/10, and exhibited almost double the flux loss after the same test.

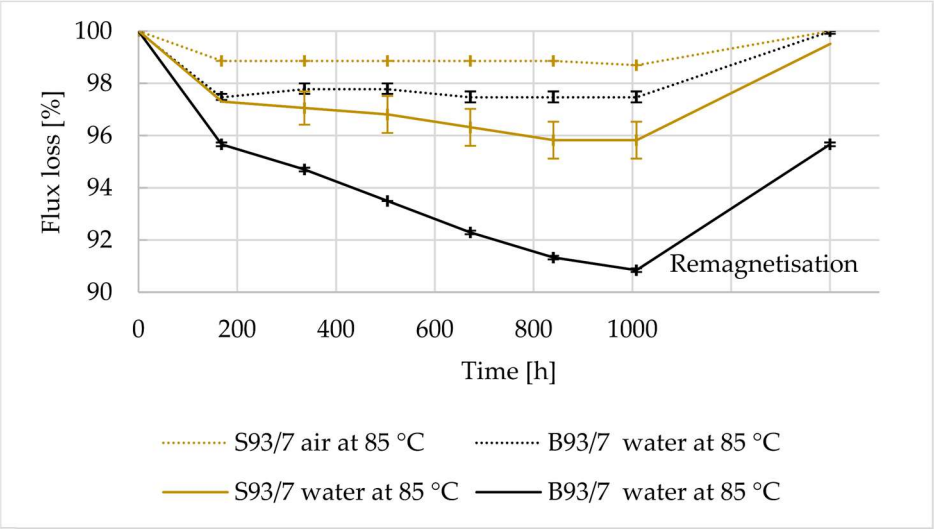

Figure 4-10: Flux loss of FDM-printed samples S93/7 and B93/7 vs. time exposure to hot water and air at 85°C and after final remagnetisation.

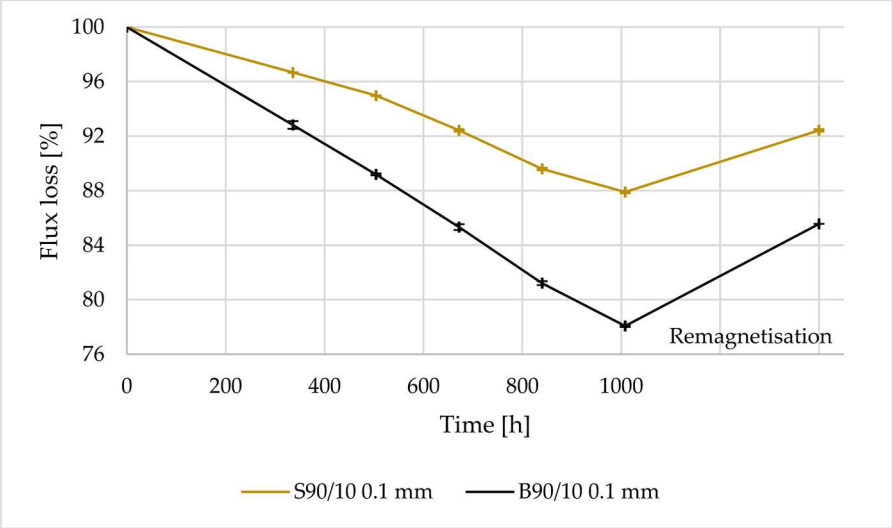

Figure 4-11: Flux loss of FDM-printed samples S90/10 and B90/10 vs. time exposure to corrosive water at 95°C for 1000 h and after final remagnetisation.

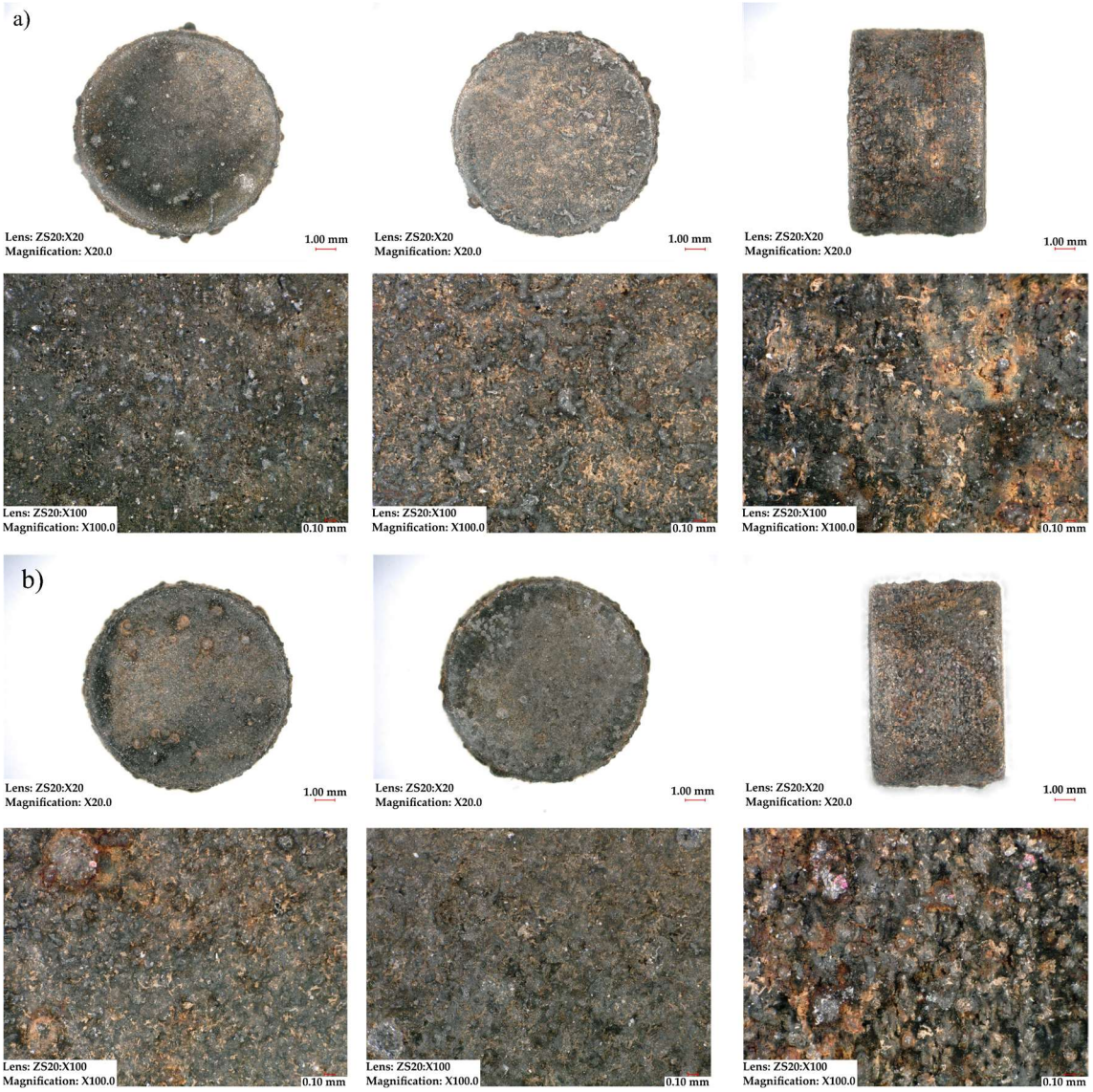

Figure 4-12: Surface corrosion of samples S90/10 (a) and B90/10 (b): top, bottom, and side after immersion in corrosive water at 95 °C for 1000 h.

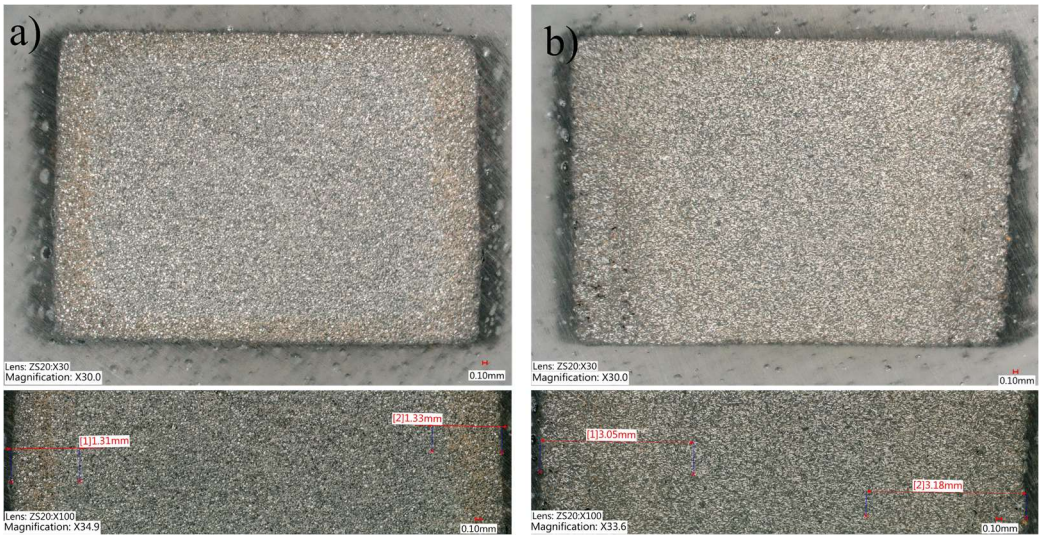

Figure 4-13: Surface corrosion, cross-section microscopic images of magnets S90/10 (a) and B90/10 (b) showing progress of corrosion after immersion in corrosive water at 95 °C for 1000 h.

Table 4-10: Overview of environmental testing and flux loss due to ageing.

Test name	Test temperature/ duration	Sample name	Reversible flux loss [%]	Irreversible flux loss [%]	Rusting
Immersion in water	85 °C/1000 h	S93/7 0.1mm	3.4	0.5	Low
		B93/7 0.1mm	9.2	4.3	Low
Exposure to hot water	85 °C/1000 h	S93/7 0.1mm	1.3	0	No evidence
		B93/7 0.1mm	2.5	0	No evidence
Immersion in corrosive water	95 °C/1000 h	S90/10 0.1mm	12.1	7.6	Severe
		B90/10 0.1mm	21.9	14.4	Severe
Bulk corrosion test	120 °C/96 h	S93/7 0.2 mm	2.9	0	Low
		B93/7 0.2 mm	4.8	0	Low
Cyclic temperature/ humidity test	-10/65 °C/240 h	S93/7 0.2 mm	0.6	0	No evidence
		B93/7 0.2 mm	0.8	0	No evidence

4.4 Conclusions

Fused deposition modelling technology can be utilized to produce Nd–Fe–B magnets bonded with PA12 in a cost-effective manner. However, FDM-printed magnets exhibit lower magnetic properties than their injection-moulded counterparts, possibly due to their lower density and higher porosity. Nonetheless, FDM-printed magnets can achieve high

magnetic properties by utilizing high loading factors. For instance, FDM magnets made from MQP S had a B_r value of 98% of the expected theoretical remanence for 93 wt.% filler loading, while those made from MQP B had 87%. The extrusion process used in filament making and FDM printing did not affect the coercivity of the samples. Furthermore, FDM-printed magnets exhibited an irreversible flux loss of less than 5% or zero when exposed to hot water, air, or pressurized steam. Thus, FDM- printed magnets are suitable for applications involving such conditions. By using a coupling agent, the adhesion between the magnetic filler and polymer binder was improved, as confirmed by SEM/EDX analysis. Overall, although FDM printing is a low-budget option for producing Nd–Fe–B magnets, it can generate magnets with comparable magnetic performance and corrosion resistance to those produced via injection moulding.

Chapter 5

Plasma Surface Treatments

Publication III
A. Damnjanović, G. Primc, R. Zaplotnik, M. Mozetič, and N. Kovačević, "The Impact of Plasma Surface Treatments on the Mechanical Properties and Magnetic Performance of FDM-Printed NdFeB/PA12 Magnets," Materials, vol. 17, no. 10, p. 2275, Jan. 2024, doi: https://doi.org/10.3390/ma17102275

5.1 Introduction

Permanent magnets, especially those based on rare earth materials, are crucial in modern high-technology applications. Their integration into electronics and renewable technologies has become increasingly widespread in daily life [115]. As the demand for such materials increases, the sustainable use of rare earth elements, recognized as critical raw materials, is essential [116].

Among the various types of permanent magnets, neodymium iron boron magnets are the most widely used owing to their superior magnetic properties. Although sintered Nd–Fe–B magnets are known for their exceptional strength, they are highly susceptible to corrosion [48]. To mitigate this, magnetic powders are often combined with polymer binders to create injection-molded or compression-molded magnets. Polymer-bonded magnets benefit from the polymer binder encapsulating the magnetic particles, thus protecting them from corrosion and oxidation [108]. Additionally, the rise of additive manufacturing, the cornerstone of Industry 4.0, is rapidly advancing the field of permanent magnet production. Unlike traditional formative manufacturing techniques such as injection or compression moulding, AM offers greater design flexibility, builds material up rather than removing it, and consumes less material. This is a significant advantage when working with costly materials such as rare-earth-based magnetic powders. AM technologies offer various methods for producing magnets, each with its advantages and drawbacks. Stereolithography-produced Nd–Fe–B magnets with high filler content can achieve impressive magnetic properties [117]. Powder bed fusion excels in complex geometries and mechanical properties but requires careful control of process parameters to avoid defects [18], [19], [20]. While binder jetting enables near-net shapes, it must overcome the issues of porosity and finish quality [27]. Fused deposition modelling is prominent for using thermoplastic filaments with magnetic fillers but faces its own set of challenges in terms of material properties and printing consistency. The challenge lies in the production of filaments with appropriate properties for consistent printing [34]. Various polymers have been used to bond Nd–Fe–B powders, including polyamide 12 (PA12) [36], thermoplastic polyurethane [38], polyphenylene sulfide [39], and polyether ether ketone [40], [118], each selected based on the intended application of the final product. Big area additive

manufacturing bypasses the intricacies of filament production by utilizing pre-compounded materials in pellet form, which are appropriate for fabricating large objects, although this comes with the trade-offs of lower resolutions and increased costs [44], [47]. BAAM-printed NdFeB/PA12 magnets have demonstrated superior magnetic properties than those produced by injection moulding. Additionally, extrusion from slurries, such as thermosetting epoxy [33] or photopolymer resins [107], presents another avenue for PBM production, combining 3D printing with UV curing for enhanced results. It is worth noting that FDM, as well as BAAM, belongs to the material extrusion family of additive manufacturing processes, as defined by ISO/ASTM 52900 [16].

However, the efficiency and durability of PBMs significantly depend on the integrity of the composite material. In Nd–Fe–B PBMs, the potential causes of poor adhesion at the interface between the magnetic particles and polymer matrix, such as oxide layer formation on the filler during processing in air or crosslinking of the polymer, pose a significant challenge, undermining the mechanical strength and overall performance of the final product [54]. This issue is even more pronounced in additive manufacturing, where the interfacial adhesion between polymer and metal is notably weaker than within the pure polymer itself [53], further compromising the mechanical strength and overall performance of the final product. Therefore, addressing the reduction in interfacial adhesion is critical for enhancing the efficiency and extending the longevity of Nd–Fe–B PBMs, ultimately broadening their range of applications.

Strategies employing adhesion promoters, such as silanes [58], [98], [119] and organo-titanates [62], have been utilized to improve adhesion. Additionally, plasma technology, known for its ability to modify or enhance surface properties, such as corrosion resistance and electrical, thermal, or mechanical characteristics, is gaining popularity. It can also influence factors such as surface tension, thereby affecting adhesion and porosity [120]. Plasma treatments have been applied to diverse materials, enhancing wetting properties in various polymers, improving the adhesion of plasma-deposited coatings, reducing friction [63], upgrading biomaterials [66], and strengthening the bond between thermoplastic polymers and metal surfaces [67]. Plasma treatment is particularly economical and environmentally friendly as it requires no water or chemicals, unlike other surface-modification methods.

While plasma treatment of macroscopic samples is a mature technology [121], the adequately uniform treatment of large quantities of powder materials in a reasonable time still represents both scientific and technological challenges [120], which arise from the huge surface-to-mass ratio of the microscopic powder. The polymer powder dropping through plasma will quickly melt upon interaction with plasma species and form aggregates, likely to stick to the surfaces facing plasma [122]. Powder in a dish will be unevenly treated: the topmost particles will melt and will be over-treated, while those deep in the container will not be affected at all. Stirring polymer powder in a dish would help uniform treatment, but the flux of plasma species should be maintained at a relatively low level to prevent overtreatment of uppermost polymer particles. The magnetic particles, on the other hand, will not melt upon treatment with a gaseous plasma sustained by a discharge of reasonable power density, so they can be treated simply by dropping through a plasma with an appropriate density of charged particles.

The aim of this study was to investigate the impact of an environmentally friendly dual-plasma treatment process on enhancing the interfacial bonding between Nd–Fe–B magnetic fillers and PA12 polymers in polymer-bonded magnets. This innovative approach, which involves modifying the surface of the Nd–Fe–B magnetic fillers with radio-frequency (RF) plasma and/or treating the PA12 polymer with low-pressure microwave plasma (MW), represents a novel contribution to the field of magnet manufacturing. By applying plasma treatment to feedstock materials, we introduce a unique method that has not been

extensively explored in previous research. Plasma treatments successfully modify the surface of polyamide 12, where low-pressure microwave plasma makes PA12 wettable and often nanostructured. However, prolonged treatment hinders its melting for laser sintering [68]. Shorter treatments improved hydrophilicity without affecting meltability; adjusting gas mixtures optimized surface properties, indicating that plasma exposure and gas composition are key to tailoring PA12 surfaces [69]. We assess the effectiveness of this approach by evaluating the mechanical and magnetic properties of FDM-printed specimens, including flexural and tensile strength. Furthermore, we conduct comprehensive corrosion tests, including immersion in water at 85 °C for 1000 h and bulk corrosion testing at 120 °C for 500 h. We hypothesize that this innovative approach will not only improve the interfacial bonding between the magnetic filler and polymer matrix but also bolster the mechanical strength of the FDM-printed specimens without detracting from their magnetic properties.

5.2 Materials and Methods

5.2.1 Materials

To fabricate filaments for FDM, we used a spherical magnetic powder based on an Nd–Pr–Fe–Co–Ti–Zr–B alloy, commercially known as MQP S, supplied by company Magnequench (Singapore). The as-received magnetic powder had the following magnetic characteristics: residual remanence between 730–760 mT, coercivity spanning from 670 to 750 kA/m, and a maximal energy product fluctuating within 80–92 kJ/m^3 [91]. Polyamide 12, available under the commercial label Vestosint (Evonik, Pandino, Italy), was selected as the polymer binder. As per the manufacturer's datasheet, PA12 has a melting point of 176 °C and an approximate bulk density of 440 g/dm^3 [123]. During the fabrication of the filament for our second batch, organo-titanate based on titanium triisostearoylisopropoxide (CAPOW®KR®TTS/H, Ken-React®, Bayonne, NJ, USA) was integrated as a coupling agent because of the poor adhesion between the inorganic filler and the organic polymer matrix.

5.2.2 Plasma treatment of magnetic filler and polymer binder

The polymer powder was treated in a low-pressure microwave plasma reactor equipped with a mixing pot. The plasma was sustained using a magnetron coupled to a waveguide with a vacuum-tight window and was concentrated just beneath the window, as shown elsewhere [124]. The small penetration depth of microwaves in the electrically conductive plasma prevented the expansion of dense plasma into the entire reactor [125], so the polymer powder was treated with the diffusing plasma. The microwave source operated at the standard frequency of 2.45 GHz. The chamber was pumped with a two-stage rotary pump (Leybold, Export, PA, USA) with an ultimate pressure below 1 Pa. The pressure was measured using a Pirani vacuum gauge (Pfeiffer Vacuum, Asslar, Germany). About 300 g of PA12 powder was added to the mixing pot equipped with a stirring device, rotating at 20 RPM. After evacuating the plasma reactor to the ultimate pressure of about 1 Pa, oxygen was leaked via a mass flow controller at 170 sccm to reach a working pressure of 70 Pa. Plasma was sustained at the power of 500 W, and the polymer powder was treated for 30 min. An experimental system was set up to treat magnetic powder while free-falling through non-equilibrium gaseous plasma, as shown in Figure 5-1.

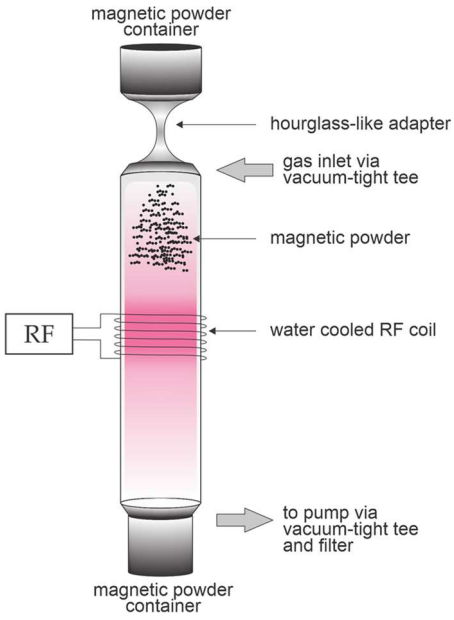

Figure 5-1: A schematic representation of a low-pressure radio frequency fall-through plasma system for the treatment of magnetic powder.

A vertical 35-cm tube with an outside diameter of 40 mm made of borosilicate glass was mounted between two vacuum flanges. A six-turn coil was wrapped around the tube and connected to a radiofrequency matching network and generator operating at the industrial frequency of 13.56 MHz (Advanced Energy, Fort Collins, CO, USA). The reactor was pumped with a two-stage rotary vacuum pump capable of achieving an ultimate pressure of 0.1 Pa (Trivac D16B, Leybold, Export, PA, USA). Oxygen was leaked via a precise needle valve, and the pressure was monitored using an absolute capacitive pressure gauge (MKS Baratron, Andover, MA, USA). Both the upper and bottom vacuum flanges were connected to two powder-storage containers of volumes of about 0.4 L. Magnetic powder was then poured into a container and attached to the reactor. On one side of the container, fitted via a KF40 flange, an hourglass-like adapter was mounted to slow down the fall of magnetic powder through plasma (length 8 cm with 4.5 mm inner narrowing that is 2 cm long). The adapter dimensions can be distinguished from Figure 5-1. The system was evacuated to roughly 3–5 Pa. Oxygen was introduced via a needle valve to obtain the operating pressure of 35 Pa, and then the plasma generator was turned on. The plasma in the H-mode was sustained in the middle of the tube. The forward and reflected powers were 500 and 20 W, respectively. The reactor was turned upside-down, so the magnetic powder fell through the powerful plasma due to gravitation. The residence time of magnetic powder in plasma was only 0.25 s. Finally, the treated powder was collected from the bottom container.

5.2.3 Filament extrusion

We used the process described in a previous study for filament extrusion [36]. To enhance the speed and printing precision, we used MQP S as the magnetic filler. The spherical morphology of the MQP S particles was found to be advantageous, enhancing printability and resulting in filaments that were easier to print than those made with melt-spun magnetic powder. Additionally, according to the aforementioned findings, samples printed with MQP S exhibited higher density, reduced porosity, and improved corrosion resistance,

demonstrating superior environmental stability with less flux loss during corrosion testing. Four distinct batches of filaments were manufactured, each with a filler loading of 93 wt.% and a polymer loading of 7 wt.% (Table 5-1). The first batch, denoted as MQP S/PA12, incorporated MQP S filler bonded with PA12 without the use of coupling agents or plasma treatments. This batch served as a reference for evaluating the effects of adding a coupling agent or plasma surface treatments on the mechanical and magnetic properties of FDM-printed samples. The second batch incorporated MQP S filler bonded with PA12, with an organo-titanate as the coupling agent, and was designated MQP S/PA12 CA. The addition of organo-titanate aimed to establish a molecular bridge at the interface between the two substrates, enhancing the bond strength and compatibility between the magnetic powder and polymer matrix [109]. The third batch resembled the first in terms of fillers and the absence of a coupling agent, yet PA12 underwent plasma treatment; this batch was labelled MQP S/PA12*. The final (fourth) batch mirrored the third batch in terms of coupling agent absence, but both MQP S and PA12 underwent plasma treatment, resulting in its designation as MQP S*/PA12*. A summary of the batches is presented in Table 5-1.

5.2.4 Fused deposition modelling of permanent magnets

The PBMs used in this study were fabricated using an industrial-grade desktop 3D printer, Flashforge Creator 3 (Jinhua, Zhejiang, China), accompanied by its slicing software, Flash Print version 5.5.2. Printing was performed at a temperature of 270 °C with a print speed of 50 mm/s, while the travel speed was adjusted to 100 mm/s. The printing platform was preheated to 80 °C to facilitate optimal adhesion of the extruded material. To further enhance bed adhesion and prevent detachment during the printing process, each specimen was printed with a 6-layer brim. Considering the risk of clogging during extrusion, a nozzle head with a 0.8 mm diameter was selected. The gap between the nozzle head and the print bed was set to 0.2 mm. The extruder was primed with a single skirt layer at the beginning of each print. The samples were printed in a horizontal orientation on the build platform, adopting a raster angle configuration of ±45° for alternate layers and ensuring an infill density of 100 %. Cylindrical specimens measuring 10 mm × 9.50 mm were produced to evaluate the magnetic properties and environmental stability of the printed samples. For mechanical assessments, dog-bone-shaped samples with dimensions of length 75 mm, width 12.5 mm, thickness 4 mm, and gauge length 20 mm were printed to determine the tensile properties in accordance with the ISO 527-2 standard [94]. The samples for the flexural test had dimensions of 80 mm length, 10 mm width, and 4 mm thickness, in accordance with the ISO 178 standard [93]. A detailed summary of the printing parameters is presented in Table 5-2, while Figure 5-2 illustrates the spooled filaments and the printed samples, and Figure 5-3 outlines the process flow from material preparation to FDM printing.

Figure 5-2: Images of FDM printed tensile, flexural test samples, and cylinders (a), FDM printing of tensile test sample (b), extruded and spooled filaments (c), and FDM printed cylindrical magnet (d).

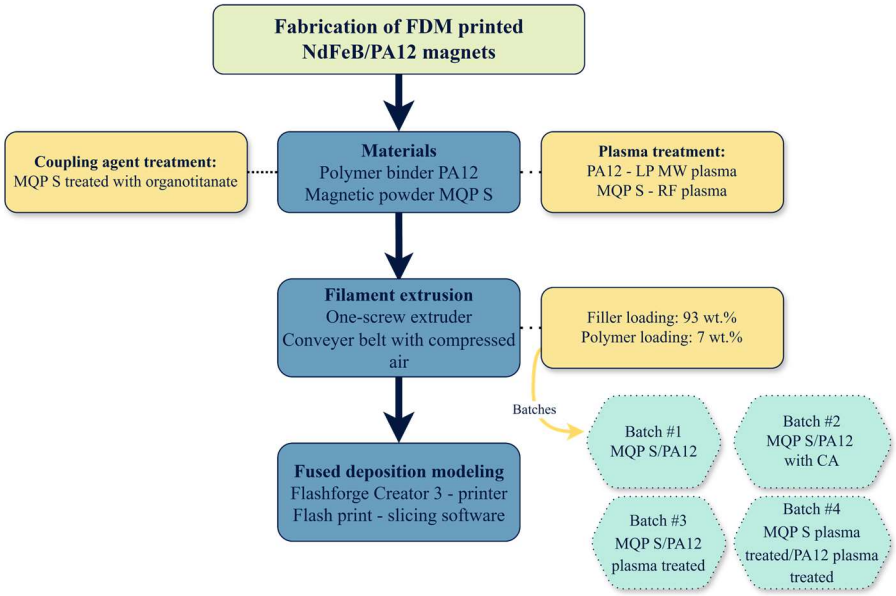

Figure 5-3: Process diagram highlighting the major steps from material selection to FDM printed parts.

Table 5-1: Overview of manufactured filament batches.

Batch label	Magnetic filler	Polymer binder	Coupling agent	Surface treatment
MQP S/PA12	Nd–Fe–B	Polyamide 12	None	None
MQP S/PA12 CA	Nd–Fe–B	Polyamide 12	Organo-titanate	None
MQP S/PA12*	Nd–Fe–B	Polyamide 12	None	Low-pressure microwave (MW) plasma *

MQP S*/PA12*	Nd–Fe–B	Polyamide 12	None	Radiofrequency plasma * and low-pressure microwave plasma *

Table 5-2: Detailed printing parameters for the FDM fabrication.

Printing parameter	Value [unit]
Material	MQP S bonded with PA12
Nozzle temperature	270 °C
Printing speed	50 mm/s
Travel speed	100 mm/s
Platform temperature	80 °C
Nozzle head diameter	0.8 mm
Raster angle	±45°
Infill density	100%
Infill pattern	Hexagon
Layer thicknesses	0.15 mm

5.2.5 Characterisation

Various techniques have been employed to characterize the physical, magnetic, and mechanical properties of filaments and FDM-printed samples derived from four distinct batches. A review of the literature on polyamide activation by plasma treatments indicates varied findings, with discussions on functional group types often avoided owing to the difficulties of overlapping peaks when using standard XPS for surface characterisation [126], [127]. However, wettability is determined by the straightforward technique, i.e. interaction with water. A clear distinction emerged when observing the behaviour of polymer powders in water plasma-treated PA12 dispersed effectively, indicating an improved affinity for water, whereas untreated PA12 remained floating on the water surface. Obviously, plasma treatment of polymer powder resulted in a significant increase in wettability. The quantitative technique of the sessile drop method is not feasible for fine powder because the water droplet is larger than the powder.

The surface morphology and elemental composition of filaments and fractured surfaces of mechanical test tubes after the tensile test were analysed via SEM coupled with EDX spectroscopy. SEM micrographs and EDX spectra were acquired in the secondary electron mode using a Jeol–IT300 SEM equipped with an Oxford EDX system, operating at a beam energy of 15 keV. Notably, no pre-treatment was applied to the samples, which were fixed onto carbon tape prior to analysis.

The filaments from all four batches were subjected to thermogravimetric analysis (TGA) to assess their temperature stability and filler content. TGA tests were performed using a Mettler Toledo thermogravimetric analyser TGA/DSC1 model (Greifensee, Switzerland). Uniform test conditions were maintained for all batches in dynamic mode, with the samples subjected to heating from ambient temperature to 600 °C at a heating rate of 10 °C/min in the presence of air as the purge gas.

Differential scanning calorimetry (DSC) was employed to evaluate the thermal stability, influence of additives and fillers, melting behaviour, and cold crystallisation of the filaments. The DSC analysis was conducted using a Mettler Toledo DSC1 STARe System

(Greifensee, Switzerland). The first cooling and the second heating run were examined, with the samples undergoing heating from 25 °C to 480 °C at a rate of 10 °C/min under an air atmosphere to determine melting behaviour. Additionally, a cooling cycle was performed between two heating cycles, involving a temperature range of 200–30 °C at a rate of 10 °C/min in an air atmosphere to ascertain cold crystallisation. The degree of crystallinity (X_c [%]) was calculated using the following formula:

$$X_c = \frac{\Delta H_m}{(1 - w_f) \times \Delta H_0} \times 100, \tag{5.1}$$

where ΔHm [J/g] represents the melting enthalpy after the second heating, w_f is the weight fraction of the filler [%], and ΔH_0 [J/g] corresponds to the melting enthalpy [J/g] of 100% crystalline PA12 (245 J/g[38], [111]).

To assess the rheological properties of the filaments, melt flow index measurements were conducted using an LMI5000 Series instrument (Dynisco, Franklin, MA, USA). The filaments were granulated, and 30 g of each batch was introduced into an MFI capillary and preheated to 260 °C. The melt time was set at 120 s, and a 5 kg load was applied. Archimedes' principle was employed using an analytical balance (XP205 by Mettler-Toledo, Greifensee, Switzerland) to determine the densities of the printed cylinders. The measured densities were compared with the calculated densities, which were determined using the rule of mixtures, not accounting for the void presence, using the following equation:

$$\rho_{calculated} = \frac{\rho_{filler} \times vol\%_{filler} + \rho_{add1} \times vol\%_{add1} + \rho_{add} \times vo\ \%_{add2} + \rho_{add3} \times vol\%_{add3} + \rho_{polymer} \times vol\%_{polymer}}{100}, \tag{5.2}$$

were labels add1, add2, and add3 refer to the following additives: the coupling agent, internal lubricant, and external lubricant, respectively.

Porosity was evaluated using the following equation:

$$Porosity\ (\%) = \frac{\rho_{calculated} - \rho_{measured}}{\rho_{calculated}} \times 100, \tag{5.3}$$

where $\rho_{calculated}$ represents the calculated density, and $\rho_{measured}$ denotes the measured density. To investigate the internal structure and assess the porosity, potential voids, or interlayer air gaps, one sample from each batch was subjected to high-resolution X-ray computed tomography (CT) scanning. The scans were performed using a Phoenix v|tome|x s240 system (General Electric, Cincinnati, OH, USA). The operational parameters for the CT scans were set to a voltage of 170 kV and current of 230 µA, with an exposure time of 200 ms per projection. The acquired data were reconstructed to visualize and quantify the internal morphology of the printed samples, enabling the analysis of their structural integrity. The FDM-printed cylinders were subjected to magnetisation using an impulse magnetizer K-Series (MAGNET-PHYSIK; Köln, Germany) at a voltage of 2000 V to reach saturation. Following magnetisation, residual remanence and intrinsic coercivity were determined using a permeameter (PERMAGRAPH®, MAGNET-PHYSIK, Köln, Germany). The measured residual remanence was compared to the theoretical value, which was calculated using the following formula:

$$Br_{theorethical} = \frac{vol\%_{filler}}{100} \times Br_{as-received\ powder} \tag{5.4}$$

The magnetic flux of the magnetized cylinders was measured before and after subjecting them to environmental tests using a Helmholtz coil (MS 75 with an electronic Fluxmeter EF 14, MAGNET-PHYSIK, Köln, Germany).

Mechanical testing was performed at room temperature on five samples from each batch. The mechanical evaluation included both flexural and tensile tests. Flexural tests were performed at a testing speed of 1 mm/min using a Zwick test machine (Z100, Zwick Roell, Ulm, Germany) in accordance with the ISO 178:2001 standard. Following the ISO 527-2 guidelines, tensile testing was also conducted using the same testing apparatus employed for flexural testing, maintaining a testing speed of 1 mm/min. A load cell with a capacity of 100 kN was used in the tests.

5.2.6 Evaluation of environmental stability and corrosion resistance

Two test scenarios were employed to assess the environmental stability and corrosion resistance of FDM-printed cylinders. The magnetic flux was measured before and after each test, with a minimum of three samples. The first test aimed to evaluate magnet stability in a high-temperature aqueous environment, targeting the potential influence of water absorption on flux loss. The magnetized cylinders were immersed in deionized water at 85 °C for 1000 h. Additionally, a bulk corrosion test was conducted to evaluate the degradation of the material under elevated temperature and exposure to water vapour. The cylinders were subjected for 500 h to pressurized steam at 120 °C and 2 bars to simulate conditions that may lead to accelerated material deterioration and, consequently, flux loss.

5.3 Results and Discussion

5.3.1 Characterisation of the filaments

SEM micrographs of fractured surfaces of filaments for all four batches are shown in Figure 5-4. Table 5-3, Table 5-4, Table 5-5 and Table 5-6 present the elemental compositions (wt.%) of major elements detected on the cross-sectional areas of the filament surfaces by EDX, including both the magnetic powders and the polymer matrix within the filament. Examination of the SEM images revealed no noticeable contrast variation among batches. The homogeneity and distribution of the magnetic particles within the polymer matrix were consistent across all batches. The voids observed in the images suggest a debonding mechanism in which the MQP S particles are pulled from the matrix.

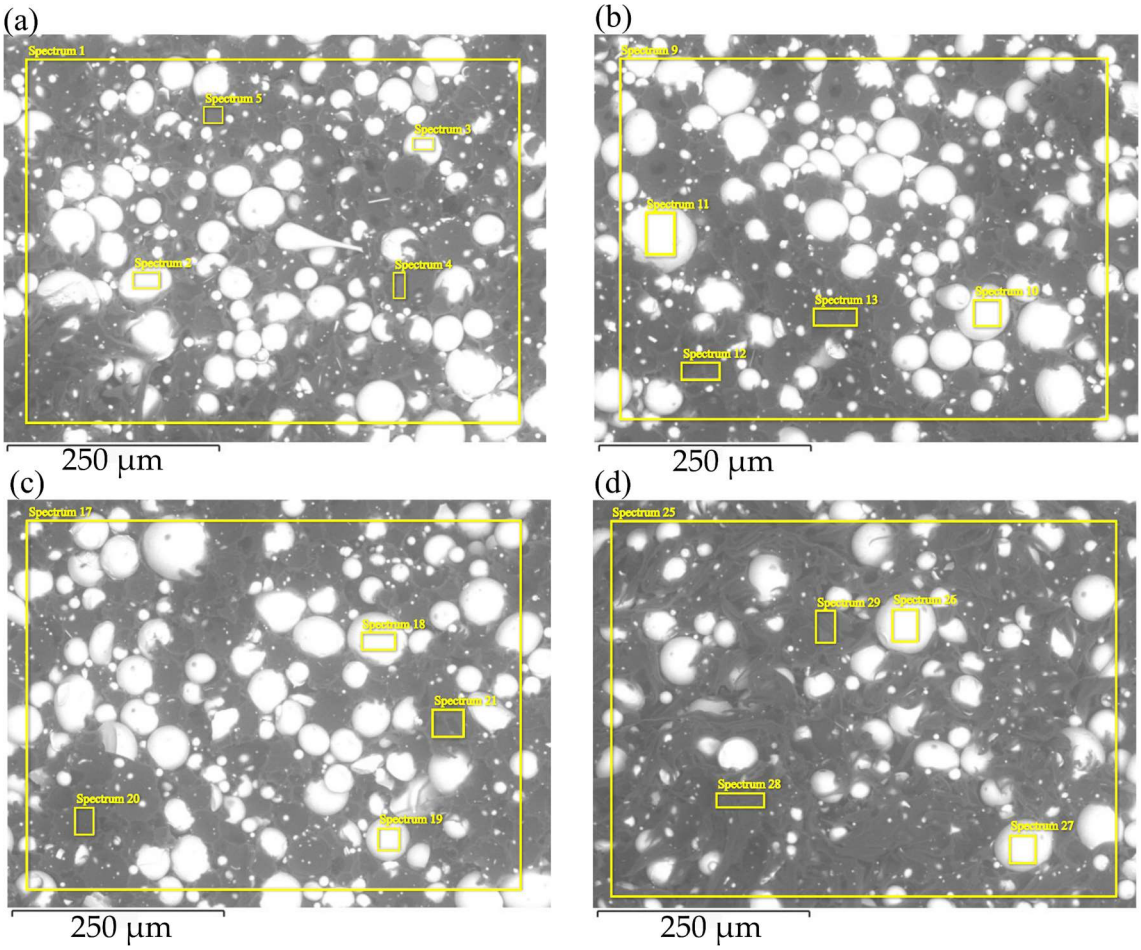

Figure 5-4: SEM micrographs of filament fractured surface for batches (a) MQP S/PA12, (b) MQP S/PA12 CA, (c) MQP S/PA12*, and (d) MQP S*/PA12*. Note that spherical lighter-coloured particles represent MQP S particles, while the darker material corresponds to the PA12 matrix.

The elemental compositions of all filament batches were comparable, with a rather high concentration of carbon (C) observed in the spectra MQP S. This high C concentration is likely attributed to examining cross-sections involving filament breakage by pulling. It appears that when the filament was torn apart, the MQP S particles retained some polymer on their surfaces, contributing to the high concentration of C observed in the spectra of MQP S.

Table 5-3: Elemental compositions (wt.%) detected in the cross-sectional areas of the filament surface of batch MQP S/PA12.

Spectrum	MQP S		PA12	
label	Sp. 2	Sp. 1	Sp. 4	Sp. 5
C	48.4	49.5	72.3	74.3
O	4.9	4.8	9.2	9.0
Ti	1.1	1.1	0.4	0.4
Fe	33.1	33.2	13.4	12.0
Co	1.7	1.3	0.5	0.5
Zr	2.2	2.1	0.8	0.7

Nd	8.6	8.0	3.4	3.1
Total	100.0	100.0	100.0	100.0

Table 5-4: Elemental compositions (wt.%) detected in the cross-sectional areas of the filament surface of batch MQP S/PA12 CA.

Spectrum	MQP S		PA12	
label	Sp. 10	Sp. 11	Sp. 12	Sp. 13
C	44.5	46.4	70.6	72.3
O	4.9	5.5	9.4	9.7
Ti	1.1	1.0	0.6	0.5
Fe	36.6	34.6	14.1	12.9
Co	1.7	1.5	0.7	0.5
Zr	2.1	2.0	0.9	0.7
Nd	9.1	9.0	3.7	3.4
Total	100.0	100.0	100.0	100.0

Table 5-5: Elemental compositions (wt.%) detected in the cross-sectional areas of the filament surface of batch MQP S/PA12*.

Spectrum	MQP S		PA12	
label	Sp. 18	Sp. 19	Sp. 20	Sp. 21
C	47.0	46.2	71.5	71.2
O	4.4	4.3	9.1	7.7
Ti	1.1	1.1	0.4	0.4
Fe	35.3	35.7	13.7	15.2
Co	1.4	1.3	0.6	0.6
Zr	2.0	2.2	0.9	0.9
Nd	8.8	9.2	3.8	4.0
Total	100.0	100.0	100.0	100.0

Table 5-6: Elemental compositions (wt.%) detected in the cross-sectional areas of the filament surface of batch MQP S*/PA12*.

Spectrum	MQP S		PA12	
label	Sp. 26	Sp. 27	Sp. 28	Sp. 29
C	50.6	51.3	76.5	74.3
O	4.8	4.7	10.8	9.5
Ti	1.1	0.9	0.3	0.3
Fe	32.2	31.8	9.1	11.5
Co	1.3	1.3	0.4	0.4

Zr	1.8	1.8	0.6	0.8
Nd	8.2	8.2	2.3	3.2
Total	100.0	100.0	100.0	100.0

The results obtained from the TGA analysis are shown in Figure 5-5. TGA offers a useful means of estimating polymer content, as the percentage of mass loss corresponds to the extent of polymer degradation. As expected, across all four batches, each containing 7 wt.% polymer, the mass loss remained close to 7%, as demonstrated in Figure 5-5.

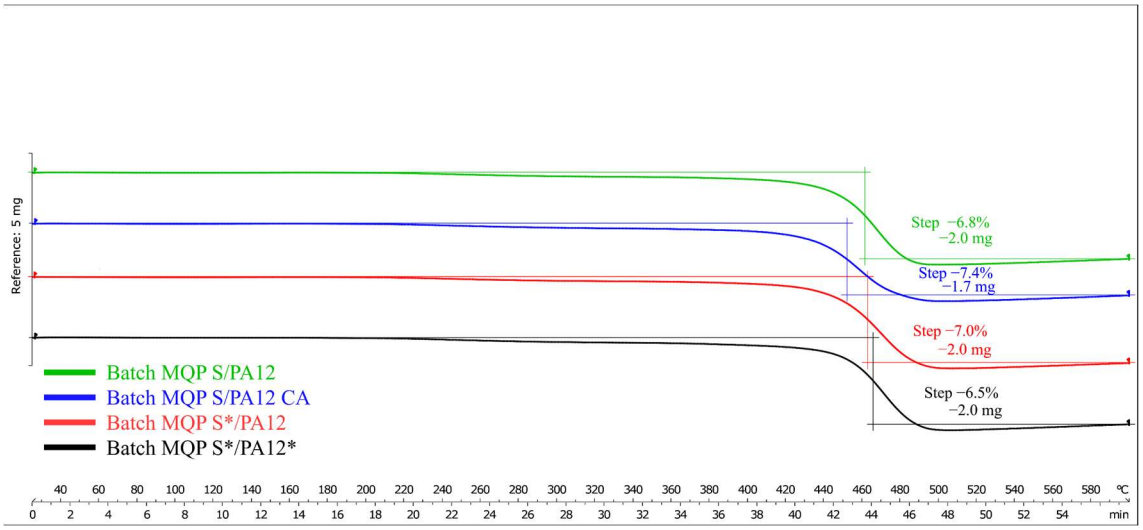

Figure 5-5: TGA curves depicting the thermal degradation behaviour of filaments from all four produced batches.

Although there were minor variations among the batches, these fluctuations suggest that the feedstock materials may not have been perfectly homogenized during filament production. Notably, the second batch (blue curve in Figure 5-5), which incorporated organo-titanate as a coupling agent, exhibited the highest mass loss due to the partial degradation of the coupling agent itself.

Results of the DSC analysis, presented in Figure 5-6 and Table 5-7, revealed that the melting temperatures (T_{m1} and T_{m2}) after the first and second heating cycles for all four batches were consistently close, with T_{m1} at approximately 176 °C and T_{m2} at approximately 175 °C. This uniformity suggests similar thermal stability and composition among batches in terms of the factors influencing the melting points. The enthalpy changes (ΔH_{m1} and ΔH_{m2}) after the first and second heating cycles showed minor variations among batches, with values in the second heating cycle (ΔH_{m2}) being slightly lower, possibly owing to decreased crystallinity or structural changes [111]. The calculated degree of crystallinity ranged from 19.5% to 21.7%. Notably, the batch MQP S/PA12 CA exhibited slightly higher crystallinity, suggesting that organo-titanate as a coupling agent contributed to the increased crystalline structure formation. Similarly, in the case of MQP S*/PA12*, where both the filler and binder underwent plasma surface modification, the higher degree of crystallinity can be attributed to these modifications.

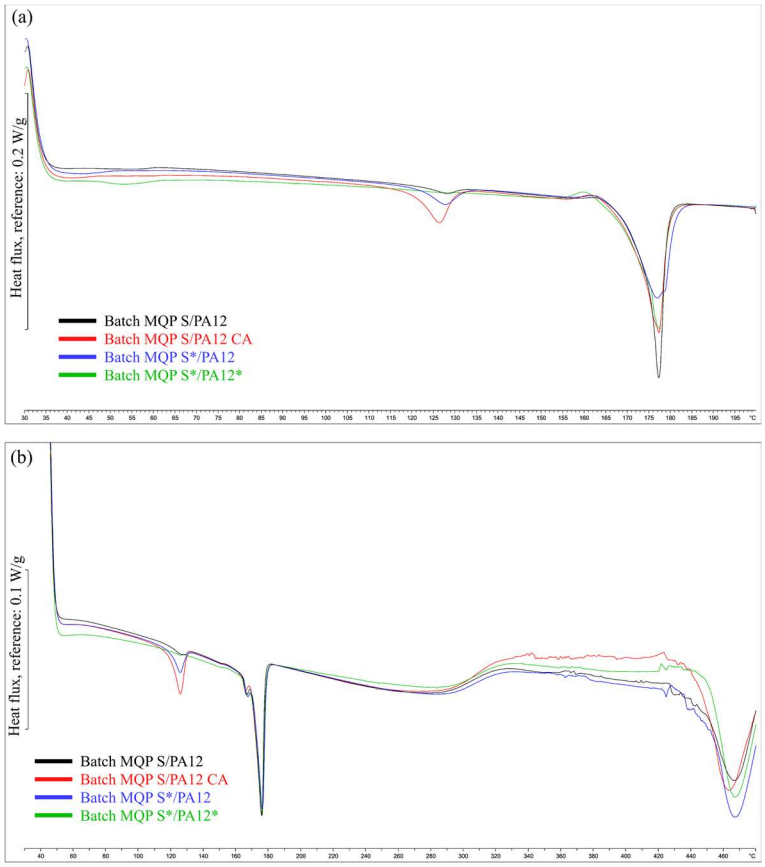

Figure 5-6: First (a) and second (b) heating DSC curves for extruded filaments.

Table 5-7: Overview of DSC analysis for filament batches, including melting temperatures (T_{m1} and T_{m2}), enthalpy (ΔH_{m1} and ΔH_{m2}) after first and second heating cycles, cold crystallisation temperature (T_c), enthalpy (ΔH_c) after the cooling cycle, and calculated degree of crystallinity (W_c).

Batch	T_{m1} (°C)	ΔH_{m1} (J/g)	T_c (°C)	ΔH_c (J/g)	T_{m2} (°C)	ΔH_{m2} (J/g)	X_c (%)
MQP S/PA12	176.8	4.4	150.0	3.9	175.4	3.4	19.5
MQP S/PA12 CA	176.7	4.3	148.2	4.2	175.4	3.7	21.7
MQP S/PA12*	176.4	4.1	149.6	3.9	175.7	3.6	20.8
MQP S*/PA12*	176.5	4.3	150.0	4.0	175.4	3.7	21.4

The MFI data for all batches of filament are presented in Table 5-8. The batch labelled MQP S/PA12 CA exhibited the highest MFI among all the batches. A higher MFI can be attributed to the presence of a coupling agent in the form of organo-titanate, which enhances the dispersion between the inorganic filler phase and organic polymer phase. Consequently, it promotes effective deagglomeration and the subsequent removal of air and water from the interface [128]. Conversely, the batch where only the polymer underwent

treatment in a low-pressure microwave plasma reactor displayed the lowest MFI. Similar plasma treatment resulted in suboptimal polymer melting behaviour, particularly when prolonged low-pressure microwave plasma treatment was applied to achieve target morphological changes [68]. These changes proved to be more advantageous when the magnetic filler was also subjected to radio-frequency plasma treatment, as observed in the case of batch MQP S*/PA12*. Importantly, suboptimal MFI values can lead to challenges in the extrusion process, such as over-extrusion or inconsistent filament extrusion, impacting the quality and consistency of FDM-printed samples.

Table 5-8: Summary of the MFI data for each batch.

Batch	MFI [g/10 min]	Standard deviation
MQP S/PA12	216	21
MQP S/PA12 CA	289	9
MQP S/PA12*	185	12
MQP S*/PA12*	239	10

5.3.2 Properties of the FDM-printed polymer-bonded magnets

Table 5-9 provides an overview of the measured and calculated densities of FDM-printed cylinders, along with the corresponding calculated porosity. It is noteworthy that in a prior study, injection-moulded cylinders produced from the same feedstock materials as batch MQP S/PA12 CA achieved a measured density exceeding 4.5 g/cm^3 and exhibited a calculated porosity of less than 2%. In the context of this study, the achieved FDM densities ranged from 92% to 94% of the theoretical density, indicating a reasonably high level of material consolidation. Nevertheless, it is important to acknowledge that FDM-printed cylinders inherently possess higher porosity than injection-moulded ones due to the nature of the printing process itself. FDM technology yields parts with increased porosity compared to those produced through alternative manufacturing methods [129]. Since identical printing parameters were applied across all batches, the observed higher porosity in the FDM cylinders can be attributed to potential challenges in achieving optimal layer-to-layer adhesion during the printing process.

Table 5-9: Measured and theoretical densities along with porosity of FDM-printed cylinders for each batch.

Batch	Measured density [g/cm3]	Vol.% filler	Theoretical density	Porosity [%]
MQP S/PA12	4.5 ± 0.1	65.5	4.8	6.0 ± 0.4
MQP S/PA12 CA	4.4 ± 0.1	66.9	4.8	8.4 ± 1.1
MQP S/PA12*	4.4 ± 0.1	65.5	4.8	8.0 ± 0.5
MQP S*/PA12*	4.5 ± 0.1	65.5	4.8	5.9 ± 0.7

The CT scan analysis across all batches, including tensile test tubes, flexural test tubes, and cylinders, showed that the cylinders exhibited the least detectable voids. This suggests

a correlation between the smaller dimensional scale of the cylinders and a reduction in observable porosity, potentially due to the layer resolution and deposition characteristics inherent to FDM. In contrast, mechanical test tubes manifested a greater frequency of air voids, indicating a variance in the filament-to-filament adhesion during the printing process. In the reference batch (MQP S/PA12), voids are present sporadically, which could be indicative of a uniform filler distribution that is not influenced by a coupling agent. Contrastingly, introducing an organo-titanate coupling agent in batch MQP S/PA12 CA is associated with the most detectable voids and air gaps. This observation is particularly interesting when considering the batch's highest MFI value. The elevated MFI could imply a reduced viscosity, potentially facilitating the printing process but also allowing for increased void formation, likely due to the material flowing too readily, leading to inconsistent layer adhesion and increased porosity. Similarly, batch MQP S/PA12* also exhibited a significant presence of voids. The lowest MFI value of this batch suggests that the increased viscosity could have adversely affected the printing process, possibly hindering the material's ability to flow and merge between layers, thus contributing to the formation of voids [130]. The batch MQP S*/PA12* voids may signal an altered interaction between the modified surfaces of the filler and the polymer, potentially influenced by the interaction between the altered surface-free energies of plasma-treated filler and polymer [68]. Detailed visualisation of these characteristics can be seen in the CT scan depicted in Figure 5-7.

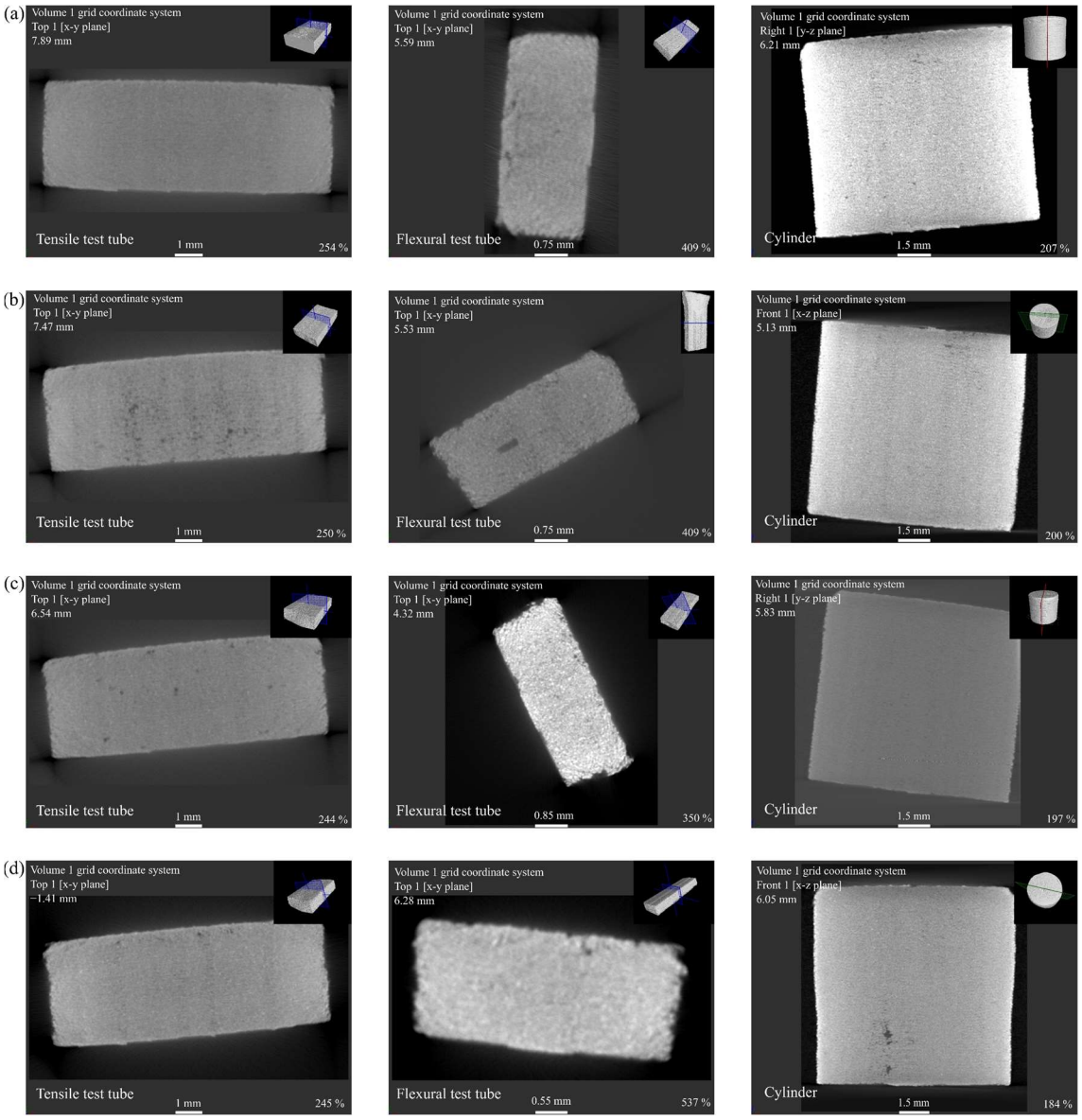

Figure 5-7: CT scan comparison of FDM-printed samplesin batches: (a) MQP S/PA12, (b) MQP S/PA12 CA, (c) MQP S/PA12*, and (d) MQP S*/PA12*.

When it comes to magnetic properties and residual remanence (B_r) in PBMs, they are significantly influenced by the volume fraction of the magnetic filler within the magnet. Generally, higher volume percentages of filler lead to increased B_r values. However, the presence of pores can have a counteractive effect, diminishing the achieved B_r [79]. In Table 5-10, both measured and theoretical B_r values for FDM-printed cylinders are presented. Across all batches, the achieved B_r values ranged from 85% to 89% of their theoretical counterparts. Notably, a correlation can be observed between measured porosity values from Table 5-9 and the achieved B_r values; samples with higher porosity tend to exhibit lower B_r values. Specifically, batches MQP S/PA12 CA and MQP S/PA12* had porosity levels of 8.4% and 8%, respectively, achieving B_r values of 85% and 86% of their theoretical B_r. Conversely, batches MQP S/PA12 and MQP S*/PA12*, which had lower porosity at approximately 6%, achieved nearly 89% of their theoretical B_r values. In Table 5-10,

measured values for intrinsic coercivity can be observed. Considering that the as-received MQP S powder exhibits an H_{ci} range of 670–750 kA/m [91], it becomes evident that certain FDM batches displayed H_{ci} lower than that of the as-received MQP S powder. This decrease in H_{ci} can be attributed to inappropriate processing conditions that may have altered the microstructure of the materials. Poor adhesion between the polymer matrix and the magnetic particles results in a reduction in coercivity. It is worth mentioning that during filament extrusion, the feedstock material, including MQP S powder, was exposed to a temperature range of 180 °C to 200 °C for a 30-min duration. This thermal exposure likely contributed to the oxidation of MQP S particles. Furthermore, any occurrence of larger grain sizes or misaligned grains during the printing process could lead to a decrease in H_{ci} values. Interestingly, the batch containing a coupling agent stands out as the exception, maintaining the same H_{ci} values as the as-received MQP S powder. This further confirms that the coupling agent could effectively shield the magnetic powder during filament manufacturing and extrusion processes.

Table 5-10: Summary of magnetic properties for FDM printed cylinders: maximum energy product (BH_{max}), measured and theoretical remanence (B_r), and intrinsic coercivity (H_{ci}).

Sample	BH_{max} [kJ/m^3]	H_{ci} [kA/m]	$B_{r\ measured}$ [mT]	$B_{r\ theoretical}$ [mT]	$B_{r\ measured}$ [% of $B_{r\ theoretical}$]
MQP S/PA12	29.4 ± 0.4	650 ± 1	432.3 ± 3.5	488.1	88.6
MQP S/PA12 CA	28.3 ± 0.1	710.2 ± 0.8	422.1 ± 0.8	498.7	84.7
MQP S/PA12*	28.0 ± 0.4	649.7 ± 1.2	422.1 ± 2.7	488.1	86.5
MQP S*/PA12*	27.9 ± 1.5	650 ± 0.3	434.4 ± 0.8	488.1	89.0

Tensile test results of batches of FDM-produced composites, presented in Table 5-11, provide an overview of how different treatments and the inherent characteristics of FDM, such as increased porosity and layer adhesion variability, impact the mechanical properties of these materials. All batches exhibited variations in elastic modulus as well as relatively large standard deviations, indicating potential inconsistencies in material properties. This variability could stem from the FDM process itself, where issues in layer consolidation can lead to poor interlayer adhesion, reducing the structural integrity of the printed parts. Additionally, porosity within the layers is a common concern in FDM printing, further contributing to potential weaknesses in the mechanical structure and impacting the elastic modulus measurements [131]. The addition of 0.5 wt.% of organo-titanate in MQP S/PA12 CA led to a reduced modulus of 141 ± 40 MPa when compared to MQP S/PA12, indicating enhanced flexibility but at the cost of increased brittleness, as evidenced by its significantly lower ductility (5 ± 2%). In the third batch, MQP S/PA12*, where PA12 was treated with low-pressure microwave plasma, a considerable increase in stiffness was observed, with an elastic modulus of 974 ± 161 MPa. This suggests that plasma treatment improves material properties, likely due to enhanced adhesion at the molecular level. The final batch, MQP S*/PA12*, which underwent dual plasma treatment, presented a balanced profile of moderate stiffness (578 ± 389 MPa) and the highest ductility (21 ± 2%), indicating an optimal combination of treatments for improved flexibility and consistency. Across all batches, tensile strength values were relatively similar, ranging from 5.5 to 6.9 MPa. Despite the different treatments, this uniformity suggests that while FDM-produced materials can withstand some tension, their strength in resisting a pulling force is not

exceptionally high, which is a characteristic to be considered in their application. Overall, the results show that the tensile properties of FDM-produced materials, particularly elastic modulus and elongation at break, vary significantly across different batches, emphasizing the crucial role of specific treatments in material optimisation. Evidently, microwave and radiofrequency plasma treatments have been shown to enhance these properties markedly. Despite these variations, the tensile strength across all batches remains consistently limited, underscoring a characteristic trait of FDM materials in their response to tensile stress.

When it comes to flexural properties, presented in Table 5-12, the first batch, MQP S/PA12, which combined MQP S filler with PA12 without coupling agents, demonstrated a flexural strength of 14 ± 2 MPa and a strain of 6 ± 2%. This serves as a reference for the untreated material's performance. In contrast, the second batch, MQP S/PA12 CA, which included an organo-titanate coupling agent, showed a lower flexural strength of 10 ± 1 MPa but a slightly higher strain of 7 ± 1%, suggesting that the addition of the coupling agent may lead to a decrease in strength but a marginal increase in flexibility. The third batch, MQP S/PA12*, where PA12 underwent microwave plasma treatment, exhibited a flexural strength of 10 ± 1 MPa and an increased strain of 8.6 ± 0.3%, indicating that plasma treatment of the polymer powder can enhance the material's flexibility. This is evident in the higher strain value compared to the untreated and coupling agent-treated batches. The final batch, MQP S*/PA12*, where both MQP S and PA12 underwent radiofrequency and microwave plasma treatment, respectively, showed the highest flexural strength of 15.4 ± 0.4 MPa and a strain of 5 ± 1%. This suggests that the dual plasma treatment significantly enhances the material's strength while maintaining a comparable level of flexibility to the untreated batch. These results highlight the influence of material treatments on the flexural properties of FDM-printed composites. The inclusion of a coupling agent and plasma treatments, particularly dual plasma treatment, has been found to significantly alter the flexural strength and strain, demonstrating the potential for tailoring material properties through specific processing techniques in FDM applications.

Table 5-11: Overview of elastic modulus, tensile strength, and elongation at break for different batches of 7 wt.% for PA12 and 93 wt.% for Nd–Fe–B FDM-produced composites.

Batch	Elastic Modulus [MPa]	Tensile Strength at Yield [MPa]	Elongation at Yield [%]
MQP S/PA12	621 ± 247	6.9 ± 0.3	17 ± 4
MQP S/PA12 CA	141 ± 40	6 ± 1	5 ± 2
MQP S/PA12*	974 ± 161	5.5 ± 0.3	16 ± 4
MQP S*/PA12*	578 ± 389	6 ± 1	21 ± 2

Table 5-12: Overview of flexural strength and strain for different batches of 7 wt.% PA12 and 93 wt.% Nd–Fe–B FDM-produced composites.

Batch	Flexural Strength [MPa]	Flexural Strain [%]
MQP S/PA12	14 ± 2	6 ± 2
MQP S/PA12 CA	10 ± 1	7 ± 1
MQP S/PA12*	10 ± 1	8.6 ± 0.3
MQP S*/PA12*	15.4 ± 0.4	5 ± 1

Figure 5-8 displays SEM micrographs of the fractured surfaces from each batch after the tensile test. It is evident from the images that the breakage occurs directly along the magnet/polymer interface, suggesting that delamination is more likely to occur in regions with smooth, uniform surfaces compared to areas with irregularly shaped particles [81]. This observation underscores the importance of particle morphology in influencing the adhesive bonding within the composite, potentially affecting the overall mechanical integrity of the printed structures.

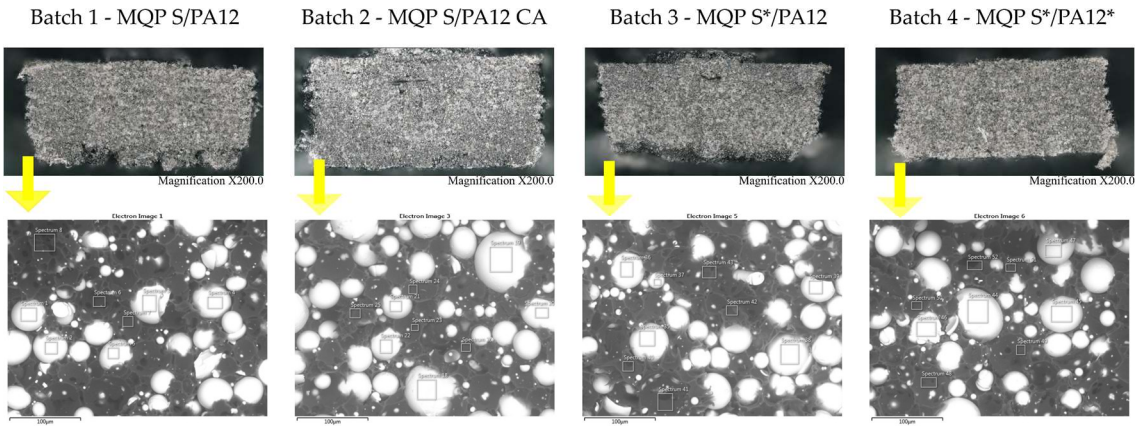

Figure 5-8: SEM images of the fractured surfaces after the tensile test.Note that spherical lighter-coloured particles represent MQP S particles, while the darker material corresponds to the PA12 matrix.

5.3.3 Evaluation of environmental stability and corrosion resistance

Environmental stability assessment of the FDM-printed magnets involved subjecting them to two distinct test scenarios. Magnetic flux measurements were taken before and after each test and the results are presented in Table 5-13 and Table 5-14, distinguishing between reversible and irreversible flux losses. When the magnets were immersed in deionized water at 85 °C for 1000 h, both reversible and irreversible flux losses were remarkably low, with the irreversible loss being below the detection limit.

Table 5-13: Results of the tests performed by immersion in water at 85 °C for 1000 h show reversible and irreversible flux losses (%).

Batch	Reversible flux loss [%]	Irreversible flux loss [%]	Rusting
MQP S/PA12	1	0	Low
MQP S/PA12 CA	0.6	0	Low
MQP S/PA12*	0.6	0	Low
MQP S*/PA12*	1.4	0	Low

Table 5-14: Bulk corrosion test results at 120 °C for 500 h show reversible and irreversible flux losses (%).

Batch	Reversible flux loss [%]	Irreversible flux loss [%]	Rusting

MQP S/PA12	2.8	0.5	Low
MQP S/PA12 CA	3.6	0.4	Low
MQP S/PA12*	2.5	0.1	Low
MQP S*/PA12*	2.3	0.4	Low

This finding suggests that despite the inherently higher porosity of the FDM-printed samples compared to magnets produced using alternative formative manufacturing technologies, the former can find industrial applications in environments where exposure to water solutions at elevated temperatures is expected. Similarly, Table 5-14 illustrates the flux loss after the BCT. In this case, as well, the magnets exhibited minimal flux loss, indicating their resistance to hygrothermal corrosion. The consistently low or zero irreversible flux loss observed after both tests underscores the potential of FDM technology in rapid prototyping. Additionally, minimal surface rust was observed after both tests, affirming the material's durability.

5.4 Conclusions

This research has demonstrated the effectiveness of FDM technology in fabricating Nd–Fe–B magnets bonded with polyamide 12, utilizing plasma treatments to improve the adhesion between inorganic magnetic and organic polymer powder. The utilisation of low-pressure radio frequency plasma for Nd–Fe–B and low-pressure microwave plasma for PA12 has enhanced the mechanical strength of FDM-printed magnets without compromising their magnetic performance. Key findings include the achievement of material densities ranging from 92% to 94% of theoretical values, with magnetic remanence across batches reaching 85% to 89% of theoretical predictions. Tensile strength values were consistently reported between 5.5 to 6.9 MPa across all treatments, highlighting the uniform resilience of the materials under tension. Flexural testing further illustrated the impact of processing techniques on material properties. The dual plasma-treated batch showcased the highest flexural strength at 15.4 ± 0.4 MPa, with a strain of 5.3 ± 0.5%, indicating a significant enhancement in material strength while maintaining rather adequate flexibility.

Environmental stability assessments underscored the materials' resistance to hygrothermal corrosion, with both reversible and irreversible flux losses remaining remarkably low or negligible (below the detection limit) after 1000 h of immersion in deionized water at 85 °C. Bulk corrosion tests supported these findings, demonstrating minimal flux loss and indicating superior durability and resistance of the plasma-treated magnets to environmental stressors.

The integration of plasma treatments with FDM printing technology offers a promising pathway to produce Nd–Fe–B/PA12 polymer-bonded magnets, achieving advancements in mechanical strength and magnetic properties without deterioration of environmental stability. This study underlines the potential of specific plasma treatments in optimizing the performance of FDM-printed magnetic materials, paving the way for their application in a variety of demanding environments.

Despite these promising results, there are some limitations to consider. Firstly, the FDM process results in materials with lower density and increased porosity compared to conventional technologies like injection moulding. This may limit the suitability of FDM for applications requiring fully dense materials. Additionally, the manufacturing of printable filament remains challenging and may require further optimisation for large-scale applications. While this study has demonstrated significant advancements in mechanical strength and magnetic properties, further research is needed to address these limitations

and explore scalable and versatile manufacturing solutions for advanced magnetic applications.

Chapter 6

Conclusions

This dissertation has rigorously tested and validated the central hypothesis that specialized surface treatments can significantly enhance the mechanical strength, magnetic properties, and environmental resilience of polymer-bonded Nd–Fe–B magnets. Through targeted experiments designed to test specific hypotheses, this research has confirmed the effectiveness of these treatments, offering promising approaches for enhancing the functionality of Nd–Fe–B magnets in various applications.

The first publication provided robust evidence supporting hypothesis 1 that surface modifications using phosphatisation, TEOS, and APTES can enhance the properties of Nd–Fe–B magnets. The treated magnets demonstrated superior mechanical properties with a tensile strength increase of 62%, an elongation at break improvement of 16.7%, and an elastic modulus enhancement of 19.9%. Additionally, these magnets showed exceptional environmental stability, with less than 5% flux loss under severe conditions, thus validating the hypothesis that surface treatments can enhance both mechanical and environmental performance without compromising magnetic properties.

Addressed in the second publication, hypotheses 2 and 4 were explored through the utilisation of organo-titanate coupling agents and the selection of gas-atomised magnetic particles for FDM printing. The findings showed that filaments made with gas-atomized particles not only had superior flowability but also resulted in printed magnets with a higher density and lower porosity. These magnets displayed a remanence (B_r) of 426 mT and an energy product (BH_{max}) of 29 kJ/m^3, compared to those made with melt-spun powders, which achieved a remanence of 456 mT and an energy product of 35 kJ/m^3. The robust performance of these magnets, particularly their enhanced corrosion resistance and thermal stability, directly supports the hypothesis that the material and processing adjustments can significantly impact the quality and functionality of printed magnets.

The third publication focused on applying plasma treatments to enhance the adhesion between magnetic powders and the polymer matrix in FDM-printed magnets. The treated batches exhibited impressive mechanical properties with an elastic modulus of 578 MPa and increased ductility at 21%. These enhancements, along with maintaining excellent magnetic properties with a remanence up to 89% of theoretical values, conclusively support the hypothesis that plasma treatments can significantly improve mechanical and magnetic properties without compromising environmental stability.

The confirmation of these hypotheses through detailed experimental work highlights the scientific relevance of this dissertation. Each of the tested strategies not only proved its effectiveness but also contributed significantly to advancing the technology of Nd–Fe–B polymer-bonded magnets. This research has broadened the potential applications of these magnets, particularly in demanding environments, and paves the way for more sustainable manufacturing practices within the field. The successful implementation of these innovative

surface treatments and processing techniques substantiates the dissertation's contribution to enhancing the performance and sustainability of rare earth magnets, marking a significant step forward in the application and development of advanced magnetic materials.

References

[1] U. Enz, “Magnetism and magnetic materials: Historical developments and present role in industry and technology,” *Handbook of ferromagnetic materials*, pp. 1–36, Jan. 1982, doi: https://doi.org/10.1016/s1574-9304(05)80087-2.

[2] D. Jiles, Introduction to Magnetism and Magnetic Materials, Third Edition. Boca Raton: Chapman and Hall/CRC, 2015.

[3] J. D. Livingston, “The history of permanent-magnet materials,” *JOM*, vol. 42, no. 2, pp. 30–34, Feb. 1990, https://doi.org/10.1007/bf03220870.

[4] J. J. Croat and J. Ormerod, “The history of permanent magnets,” in *Modern Permanent Magnets*, Elsevier, 2022, pp. 1–30.

[5] J. M. D. Coey, Y. Otani, H. Sun and D. P. F. Hurley, "Magnetic Properties of Interstitial Compounds $Sm(Fe_{11}Ti)X_{1-\partial}$ (X=N,C)," *IEEE Transl. J. Magn. Jpn*, vol. 7, no. 8, pp. 613-617, Aug. 1992, doi: 10.1109/TJMJ.1992.4565464.

[6] J. M. D. Coey, *Magnetism and Magnetic Materials,* Cambridge, UK: Cambridge University Press, 2009.

[7] B. D. Cullity and C. D. Graham, *Introduction to Magnetic Materials*, 2nd ed., Hoboken, NJ, USA: John Wiley & Sons, 2011.

[8] R. E. Roskill, *Rare Earths: Outlook to 2030,* Roskill Information Ltd Press London, 2021.

[9] S. J. Collocott *et al.*, “Applications of rare-earth permanent magnets in electrical machines: from motors for niche applications to hybrid electric vehicles,” in *Proc. China Magn. Symp.* , vol. 315, pp. 77–83, [Online] Available: http://www.ime.pw.edu.pl/zme/dyd/mater/bme/ApplicationsOfRareEarthPermanentMagnetsInElectricalMachinesFrommotorsForNicheApplicationsToHybridElectricVehicles.pdf

[10] A. D. Hansen, “Generators and power electronics for wind turbines,” *Wind power in power systems*, pp. 73–103,2012.https://doi.org/10.1002/9781119941842.ch5

[11] A. R. Jha, *Rare Earth Materials: Properties and Applications*, 1st ed. CRC Press, 2014. [Online]. Available: https://www.taylorfrancis.com/books/9781466564039

[12] J. Cui *et al.*, “Manufacturing Processes for Permanent Magnets: Part I—Sintering and Casting,” *JOM*, Springer, 2022. doi: 10.1007/s11837-022-05156-9.

[13] W. Xi, W. Liu, R. Hu, Y. Yin, and M. Yue, “Property enhancement of bonded Nd-Fe-B magnets by composite adhesive design,” *Mater. Des.*, vol. 192, Jul. 2020, doi: 10.1016/j.matdes.2020.108767.

[14] M. Grönefeld, "Review on bonded magnets," in *Bonded Magnets: Proceedings of the NATO Advanced Research Workshop on Science and Technology of Bonded Magnets Newark, USA 22–25 August 2002*, Springer, 2003, pp. 1–12.

[15] J. Liu and M. Walmer, "Process and magnetic properties of rare-earth bonded magnets," in *Handbook of Advanced Magnetic Materials*, Y. Liu, D. J. Sellmyer, and D. Shindo, Eds., Boston, MA, USA: Springer US, 2006, pp. 1008–1044. doi: 10.1007/1-4020-7984-2_24.

[16] T. D. Ngo, A. Kashani, G. Imbalzano, K. T. Q. Nguyen, and D. Hui, "Additive manufacturing (3D printing): A review of materials, methods, applications and challenges," *Compos B Eng*, vol. 143, no. December 2017, pp. 172–196, 2018, doi: 10.1016/j.compositesb.2018.02.012.

[17] ISO/ASTM, "ISO/ASTM 52900: ASTM52900-15 standard terminology for additive manufacturing—general principles—terminology.," *International Standard*, vol. 5, pp. 1–26, 2015, [Online]. Available: https://www.astm.org/Standards/ISOASTM52900.htm

[18] R. Singh *et al.*, "Powder bed fusion process in additive manufacturing: An overview," in *Mater. Today: Proc.*, Elsevier Ltd, 2019, pp. 3058–3070. doi: 10.1016/j.matpr.2020.02.635.

[19] J. Jaćimović *et al.*, "Net shape 3D printed NdFeB permanent magnet," *Adv. Eng. Mater*, vol. 19, no. 8, 2017, doi: 10.1002/adem.201700098.

[20] J. Wu, N. T. Aboulkhair, M. Degano, I. Ashcroft, and R. J. M. Hague, "Process-structure-property relationships in laser powder bed fusion of permanent magnetic Nd-Fe-B," *Mater Des*, vol. 209, p. 109992, 2021, doi: 10.1016/j.matdes.2021.109992.

[21] F. Bittner, J. Thielsch, and W. G. Drossel, "Laser powder bed fusion of Nd–Fe–B permanent magnets," *Prog. Addit. Manuf.*, vol. 5, no. 1, pp. 3–9, 2020, doi: 10.1007/s40964-020-00117-7.

[22] K. Schäfer, T. Braun, S. Riegg, J. Musekamp, and O. Gutfleisch, "Polymer-bonded magnets produced by laser powder bed fusion: Influence of powder morphology, filler fraction and energy input on the magnetic and mechanical properties," *Mater. Res. Bull.*, vol. 158, Feb. 2023, doi: 10.1016/j.materresbull.2022.112051.

[23] J. Huang, K. C. Yung, and D. T. C. Ang, "Magnetic properties of $SmCo_5$ alloy fabricated by laser sintering," *J. Mater. Sci. Mater. Electron.*, vol. 30, no. 12, pp. 11282–11290, Jun. 2019, doi: 10.1007/s10854-019-01475-x.

[24] J. A. B. Engerroff *et al.*, "Additive manufacturing of Sm-Fe-N magnets," *J. Rare Earths*, vol. 37, no. 10, pp. 1078–1082, 2019, doi: 10.1016/j.jre.2019.04.012.

[25] A. Lores, N. Azurmendi, I. Agote, and E. Zuza, "A review on recent developments in binder jetting metal additive manufacturing : materials and process characteristics," *Powder Metall.*, vol. 0, no. 0, pp. 1–30, 2019, doi: 10.1080/00325899.2019.1669299.

[26] M. Molitch-Hou, "Overview of additive manufacturing process," in *Additive Manufacturing: Materials, Processes, Quantifications and Applications*, Elsevier, 2018, pp. 1–38. doi: 10.1016/B978-0-12-812155-9.00001-3.

[27] M. Ziaee and N. B. Crane, "Binder jetting : A review of process, materials, and methods," *Addit. Manuf.*, vol. 28, no. December 2018, pp. 781–801, 2019, doi: 10.1016/j.addma.2019.05.031.

[28] M. P. Paranthaman *et al.*, "Binder Jetting : A Novel NdFeB Bonded Magnet Fabrication Process," *JOM*, vol. 68, no. 7, pp. 1980–1987, 2016, doi: 10.1007/s11837-016-1883-4.

[29] L. Li *et al.*, "A novel method combining additive manufacturing and alloy infiltration for NdFeB bonded magnet fabrication," *J Magn. Magn. Mater.*, vol. 438, pp. 163–167, 2017, doi: 10.1016/j.jmmm.2017.04.066.

[30] O. Gülcan, K. Günaydın, and A. Tamer, "The state of the art of material jetting—a critical review," *Polymers*, vol. 13, no. 16, Aug. 2021. doi: 10.3390/polym13162829.

[31] H. Song, J. Spencer, A. Jander, J. Nielsen, J. Stasiak, and V. Kasperchik, "Inkjet printing of magnetic materials with aligned anisotropy Inkjet printing of magnetic materials with aligned anisotropy," *Appl. Phys. Lett.*, vol. 308, pp. 3–6, 2014, doi: 10.1063/1.4863168.

[32] A. R. Kokkinis, D. Schaffner, and M. Studart, "Multimaterial magnetically assisted 3D printing of composite materials," *Nat. Commun.*, vol. 6, no. 1, pp. 1–10, 2015. doi: 10.1038/ncomms9643.

[33] A. J. Aguilera, A. F. E., Nagarajan, B., Fleck, B. A., & Qureshi, "Ferromagnetic particle structuring in material jetting-Manufacturing control system and software development.," *Procedia Manuf.*, vol. 34, pp. 545–551, 2019, doi: 10.1016/j.promfg.2019.06.218.

[34] F. Yang, X. Zhang, Z. Guo, S. Ye, Y. Sui, and A. A. Volinsky, "3D printing of NdFeB bonded magnets with SrFe12O19 addition," *J. Alloys Compd.*, vol. 779, pp. 900–907, 2019. doi: 10.1016/j.jallcom.2018.11.335..

[35] G. H. Loh, E. Pei, J. Gonzalez-Gutierrez, and M. Monzón, "An overview of material extrusion troubleshooting," *Appl. Sci. (Switzerland)*, vol. 10, no. 14, Jul. 2020. doi: 10.3390/app10144776.

[36] L. Li et al., "Fabrication of highly dense isotropic Nd-Fe-B nylon bonded magnets via extrusion-based additive manufacturing," *Addit. Manuf.*, vol. 21, pp. 495–500, May 2018. doi: 10.1016/j.addma.2018.04.001.

[37] A. Damnjanović and N. Kovačević, "Influence of Magnet Particle Shape on Magnetic and Environmental Stability of FDM Polymer-Bonded Magnets," *Materials*, vol. 16, no. 8, Apr. 2023, doi: 10.3390/ma16082993.

[38] A. Damnjanović, G. Primc, R. Zaplotnik, M. Mozetič, and N. Kovačević, "The Impact of Plasma Surface Treatments on the Mechanical Properties and Magnetic Performance of FDM-Printed NdFeB/PA12 Magnets," *Materials*, vol. 17, no. 10, p. 2275, May 2024, doi: 10.3390/ma17102275.

[39] J. Slapnik, I. Pulko, R. Rudolf, I. Anžel, and M. Brunčko, "Fused filament fabrication of Nd-Fe-B bonded magnets: Comparison of PA12 and TPU

matrices," *Addit. Manuf.*, vol. 38, p. 101745, Feb. 2021. doi: 10.1016/J.ADDMA.2020.101745.

[40] M. P. Paranthaman et al., "Additive manufacturing of isotropic NdFeB PPS bonded permanent magnets," *Materials*, vol. 13, no. 15, pp. 1–10, 2020. doi: 10.3390/ma13153319.

[41] L. Pigliaru et al., "3D printing of high-performance polymer-bonded PEEK-NdFeB magnetic composite materials," *Funct. Compos. Mater.*, vol. 1, no. 1, Dec. 2020. doi: 10.1186/s42252-020-00006-w.

[42] L. Pigliaru *et al.*, "Long Term Storage Issues of NdFeB magnets: coatings and PEEK/ NdFeB composites as alternative approaches", in *Proc. 69th International Astronautical Congress (IAC)*, Bremen, Germany, Oct. 1-5, 2018.

[43] KK. von Petersdorff-Campen et al., "3D printing of functional assemblies with integrated polymer-bonded magnets demonstrated with a prototype of a rotary blood pump," *Appl. Sci. (Switzerland)*, vol. 8, no. 8, Aug. 2018. doi: 10.3390/app8081275.https://www.sciencedirect.com/science/article/pii/S2214860418307012

[44] A. Roschli et al., "Designing for Big Area Additive Manufacturing," *Additive Manufacturing*, vol. 25, pp. 275–285, Jan. 2019, doi: https://doi.org/10.1016/j.addma.2018.11.006.

[45] L. Li *et al.*, "Big Area Additive Manufacturing of High Performance Bonded NdFeB Magnets," *Sci. Rep.*, vol. 6, Oct. 2016, doi: 10.1038/srep36212.

[46] B. Podmiljšak et al., "Additive-manufactured anisotropic magnets for harsh environments," *J. Magn. Magn. Mater.*, vol. 586, Nov. 2023. doi: 10.1016/j.jmmm.2023.171165.

[47] M. Suppan *et al.*, "In-situ alignment of anisotropic hard magnets of 3D printed magnets," *arXiv preprint arXiv:2201.07111*, 2022.

[48] K. Sonnleitner et al., "3D printing of polymer-bonded anisotropic magnets in an external magnetic field and by a modified production process," *Appl. Phys. Lett.*, vol. 116, no. 9, Mar. 2020. doi: 10.1063/1.5142692.

[49] K. Gandha, I. C. Nlebedim, V. Kunc, E. Lara-Curzio, R. Fredette, and M. P. Paranthaman, "Additive manufacturing of highly dense anisotropic Nd–Fe–B bonded magnets," *Scripta Mater.*, vol. 183, pp. 91–95, 2020. doi: 10.1016/j.scriptamat.2020.03.012.

[50] E. Isotahdon, E. Huttunen-Saarivirta, S. Heinonen, V. T. Kuokkala, and M. Paju, "Corrosion mechanisms of sintered Nd-Fe-B magnets in the presence of water as vapour, pressurised vapour and liquid," *J Alloys Compd*, vol. 626, pp. 349–359, 2015, doi: 10.1016/j.jallcom.2014.12.048.

[51] L. Schultz, A. M. El-Aziz, G. Barkleit, and K. Mummert, "Corrosion behaviour of Nd-Fe-B permanent magnetic alloys," *Materials Science and Engineering A*, vol. 267, no. 2, pp. 307–313, 1999, doi: 10.1016/S0921-5093(99)00107-0.

[52] G. Barkleit, A. M. El-Aziz, F. Schneider, and K. Mummert, "Characterisation of electrochemical interactions between single phases of Nd-Fe-B permanent magnets, ''. *Materials and Corrosion,* vol. 52(3), pp. 193-200, 2001.

[53] S. Fafenrot, N. Grimmelsmann, M. Wortmann, and A. Ehrmann, "Three-dimensional (3D) printing of polymer-metal hybrid materials by fused deposition modeling," *Materials*, vol. 10, no. 10, Oct. 2017. doi: 10.3390/ma10101199.

[54] A. Gardocki, D. Drummer, and E. Schmachtenberg, "Improving the stability of magnetic fillers in plastics during processing," *Int. Polym. Sci. Technol.*, vol. 38, no. 10, pp. 219–223, 2011.

[55] D. Sojer, I. Skulj, S. Kobe, J. Kovač, and P. J. McGuiness, "Protection of $Nd_2Fe_{14}B$-based melt-spun ribbons using nanoscale sol-gel derived films of SiO_2 and Al_2O_3," *Surf. Coat. Technol.*, vol. 232, pp. 123–130, Oct. 2013. doi: 10.1016/j.surfcoat.2013.04.062.

[56] A. Saliba-Silva, R. N. Faria, M. A. Baker, and I. Costa, "Improving the corrosion resistance of NdFeB magnets: An electrochemical and surface analytical study," *Surf. Coat. Technol.*, vol. 185, no. 2–3, pp. 321–328, Jul. 2004. doi: 10.1016/j.surfcoat.2003.12.015.

[57] A. Gardocki, "Investigation of the thermo-oxidative degradation of plastic bonded rare-earth magnets during the injection molding process," in *2011 1st Int. Electr. Drives Prod. Conf.*, 2011, pp. 162–166. doi: 10.1109/EDPC.2011.6085535.

[58] X. Zhang et al., "Effect of silane coupling agents on flowability and compressibility of compound for bonded NdFeB magnet," *J. Rare Earths*, vol. 40, no. 5, pp. 772–777, May 2022. doi: 10.1016/j.jre.2021.05.013.

[59] J. Hu, X. Liu, J. Zhang, and C. Cao, "Corrosion protection of Nd–Fe–B magnets by silanization," *Prog. Org. Coat.*, vol. 55, pp. 388–392, 2006. doi: 10.1016/j.porgcoat.2006.01.001.

[60] J. Xiao and J. U. Otaigbe, "Polymer bonded magnets. II. Effect of liquid crystal polymer and surface modification on magneto-mechanical properties," *Polym. Compos.*, vol. 21, no. 2, pp. 332–342, 2000. doi: 10.1002/pc.10190.

[61] K. Weissenbach and H. Mack, "Silane coupling agents," in *Functional fillers for Plastics*, pp. 57–83, 2005.

[62] H. Chen, J. Zheng, X. Cheng, W. Cai, L. Qiao, and S. Che, "Surface modification and refinement of Nd–Fe–B magnetic powder using ITDT and phosphoric acid," *JOM*, vol. 73, no. 12, pp. 3941–3949, Dec. 2021. doi: 10.1007/s11837-021-04850-4.

[63] D. Hegemann, H. Brunner, and C. Oehr, "Plasma treatment of polymers for surface and adhesion improvement," in *Nuclear Instruments and Methods in Physics Research, Section B: Beam Interactions with Materials and Atoms*, Aug. 2003, pp. 281–286. doi: 10.1016/S0168-583X(03)00644-X.

[64] S. J. Monte, "Titanate coupling agents," in *Functional Fillers for Plastics*, 2010, pp. 91–114. doi: https://doi.org/10.1002/9783527629848.ch5 .

[65] U. Cvelbar *et al.*, "White paper on the future of plasma science and technology in plastics and textiles," *Plasma Processes and Polymers*, vol. 16, no. 1, pp. 1–37, 2019, doi: 10.1002/ppap.201700228.

[66] P. K. Chu, J. Y. Chen, L. P. Wang, and N. Huang, "Plasma-surface modification of biomaterials." *Mater. Sci. Eng. R*, vol. 36, pp. 143–206, 2002.

[67] C. Ochoa-Putman and U. K. Vaidya, "Mechanisms of interfacial adhesion in metal-polymer composites: Effect of chemical treatment," *Compos. Part A Appl. Sci. Manuf.*, vol. 42, no. 8, pp. 906–915, Aug. 2011. doi: 10.1016/j.compositesa.2011.03.019.

[68] A. Almansoori et al., "Surface modification of the laser sintering standard powder polyamide 12 by plasma treatments," *Plasma Process. Polym.*, vol. 15, no. 7, p. 1800032, 2018.

[69] M. Sachs, J. Schmidt, W. Peukert, and K. E. Wirth, "Treatment of polymer powders by combining an atmospheric plasma jet and a fluidized bed reactor," *Powder Technol.*, vol. 325, pp. 490–497, 2018, doi: 10.1016/j.powtec.2017.11.016.

[70] O. Gutfleisch, M. A. Willard, E. Brück, C. H. Chen, S. G. Sankar, and J. P. Liu, "Magnetic materials and devices for the 21st century: Stronger, lighter, and more energy efficient," *Adv. Mater.*, vol. 23, no. 7, pp. 821–842, 2011. doi: 10.1002/adma.201002180.

[71] J. M. D. Coey, "Perspective and prospects for rare earth permanent magnets," *Eng.*, vol. 5, pp. 39–48, 2019. doi: 10.1016/j.eng.2018.11.034.

[72] K. Binnemans and P. T. Jones, "Rare earths and the balance problem," *J. Sustain. Metall.*, vol. 1, no. 1, pp. 29–38, 2015. doi: 10.1007/s40831-014-0005-1.

[73] K. Binnemans and P. T. Jones, "Rare Earths and the Balance Problem," *Journal of Sustainable Metallurgy*, vol. 1, no. 1, pp. 29–38, 2015, doi: 10.1007/s40831-014-0005-1.

[74] J. R. Riba, C. López-Torres, L. Romeral, and A. Garcia, "Rare-earth-free propulsion motors for electric vehicles: A technology review," *Renew. Sustain. Energy Rev.*, vol. 57, pp. 367–379, 2016. doi: 10.1016/j.rser.2015.12.121.

[75] K. Noguchi, C. Mishima, M. Yamazaki, H. Matsuoka, H. Mitarai, and Y. Honkura, "Development of dy-free NdFeB anisotropic bonded magnet (New MAGFINE)," in *2011 1st Int. Electr. Drives Prod. Conf.*, 2011, pp. 181–186. doi: 10.1109/EDPC.2011.6085539.

[76] L. Li, B. Post, V. Kunc, A. M. Elliott, and M. P. Paranthaman, "Additive manufacturing of near-net-shape bonded magnets: Prospects and challenges," *Scripta Mater.*, vol. 135, pp. 100–104, Jul. 2017. doi: 10.1016/j.scriptamat.2016.12.035.

[77] H. Wang, T. N. Lamichhane, and M. P. Paranthaman, "Review of additive manufacturing of permanent magnets for electrical machines: A prospective on wind turbine," *Mater. Today Phys.*, vol. 24, May 2022. doi: 10.1016/j.mtphys.2022.100675.

[78] M. Grönefeld, "Review on bonded magnets," in *Bonded Magnets*, G. C. Hadjipanayis, Ed., Dordrecht, Netherlands: Springer, 2003, pp. 1–12.

[79] D. Brown, B. M. Ma, and Z. Chen, "Developments in the processing and properties of NdFeB-type permanent magnets," *J. Magn. Magn. Mater.*, vol. 248, no. 3, pp. 432–440, Aug. 2002. doi: 10.1016/S0304-8853(02)00334-7.

[80] W. Xi, W. Liu, R. Hu, Y. Yin, and M. Yue, "Property enhancement of bonded Nd-Fe-B magnets by composite adhesive design," *Mater Des*, vol. 192, Jul. 2020, doi: 10.1016/j.matdes.2020.108767.

[81] J. Hemrick, E. Lara-Curzio, K. Liu, and B.-M. Ma, "Mechanical properties of thermally cycled nylon bonded Nd-Fe-B permanent magnets," *Journal of Materials Science*, vol. 39, no. 21, pp. 6509-6514, 2004.

[82] J. Xiao and J. U. Otaigbe, "Polymer-bonded magnets III. Effect of surface modification and particle size on the improved oxidation and corrosion resistance of magnetic rare earth fillers," *J. Alloys Compd.*, vol. 309, no. 1–2, pp. 100–106, 2000. doi: 10.1016/S0925-8388(00)01060-4.

[83] M. G. Garrell, A. J. Shih, B.-M. Ma, E. Lara-Curzio, and R. O. Scattergood, "Mechanical properties of nylon bonded Nd-Fe-B permanent magnets," in *Proc. 2003 Conf. Compos. Mater.*, 2003.

[84] M. G. Garrell, B. M. Ma, A. J. Shih, E. Lara-Curzio, and R. O. Scattergood, "Mechanical properties of polyphenylene-sulfide (PPS) bonded Nd-Fe-B permanent magnets," *Mater. Sci. Eng. A*, vol. 359, no. 1–2, pp. 375–383, Oct. 2003. doi: 10.1016/S0921-5093(03)00400-3.

[85] S. Tsutsumi, Y. Kato, K. Namba, and H. Yamamoto, "Functional composite material design using Hansen solubility parameters," *Results Mater.*, vol. 4, Dec. 2019. doi: 10.1016/j.rinma.2019.100046.

[86] B. Indumathy, P. Sathiyanathan, G. Prasad, M. S. Reza, A. A. Prabu, and H. Kim, "A comprehensive review on processing, development and applications of organofunctional silanes and silane-based hyperbranched polymers," *Polymers*, vol. 15, no. 11, Jun. 2023. doi: 10.3390/polym15112517.

[87] J. U. Otaigbe, J. Xiao, H. Kim, and S. Constantinides, "Influence of filler surface treatments on processability and properties of polymer-bonded Nd-Fe-B magnets," *J. Mater. Sci. Lett.*, vol. 18, no. 4, pp. 329–332, 1999. doi: 10.1023/A:1006651810847.

[88] J. Xiao, J. U. Otaigbe, and D. C. Jiles, "Modeling of magnetic properties of polymer bonded Nd-Fe-B magnets with surface modifications," *J. Magn. Magn. Mater.*, vol. 218, no. 1, pp. 60–66, 2000. doi: 10.1016/S0304-8853(00)00047-0.

[89] W. Qin, J. He, and W. Zhao, "Research on compound powder of bonded NdFeB magnets from injection molding," in *Adv. Mater. Res.*, 2011, pp. 841–846. doi: 10.4028/www.scientific.net/AMR.228-229.841.

[90] W. Liu, Y. Yang, Y. Meng, and J. Wu, "The effects of surface modification on the properties of bonded NdFeB magnets," *Mater. Trans.*, vol. 44, no. 6, pp. 1159–1162, 2003. doi: 10.2320/matertrans.44.1159.

[91] Magnequench, *Safety Data Sheet MQP-S-11-9; Part No.20001-070*, Aug. 2016. [Online].Available:https://mqitechnology.com/wp-content/uploads/2017/09/mqp-s-11-9-20001-070-r07-ce-2016-08-15.pdf.

[92] K. Shigeoka and N. Katayama, "Surface treated rare earth magnetic powder, bonded magnet resin composition that includes the rare earth magnetic powder, and bonded magnet," *Japan Pat. No. JP2011191887A*, Sep. 2011.

[93] ISO, *Plastics—Determination of flexural properties*, ISO 178, *ISO Geneva, Switzerland*, 2019.

[94] ISO, *ISO 527-2 Plastics—Determination of tensile properties—Part 2: Test conditions for molding and extrusion plastics*, ISO, 1996.

[95] C. W. Cheng, H. C. Man, and F. T. Cheng, "Magnetic and corrosion characteristics of Nd-Fe-B magnet with various surface coatings," *Mater. Sci. Eng. A*, vol. 308, no. 5, pp. 3910–3912, 1997.

[96] S. Hirosawa, S. Mino, and H. Tomizawa, "Improved corrosion resistance and magnetic properties of Nd-Fe-B-type sintered magnets with Mo and Co," *J. Appl. Phys.*, vol. 69, no. 8, pp. 5844–5846, 1991. doi: 10.1063/1.347845.

[97] ASTM, *Standard Test Method for Corrosion Test for Engine Coolants in Glassware*, ASTM D1384-05, 2019.

[98] H. Chen, J. Zheng, L. Qiao, Y. Ying, L. Jiang, and S. Che, "Surface modification of $NdFe_{12}N_x$ magnetic powder using silane coupling agent KH550," *Adv. Powder Technol.*, vol. 26, no. 2, pp. 618–621, 2015. doi: 10.1016/j.apt.2015.01.011.

[99] X. Rao, A. Abou Hassan, C. Guyon, M. Zhang, S. Ognier, and M. Tatoulian, "Plasma polymer layers with primary amino groups for immobilization of nano- and microparticles," *Plasma Chem. Plasma Process.*, vol. 40, no. 2, pp. 589–606, Mar. 2020. doi: 10.1007/s11090-019-10056-z.

[100] D. Brown, B. M. Ma, and Z. Chen, "Developments in the processing and properties of NdFeB-type permanent magnets," *J. Magn. Magn. Mater.*, vol. 248, no. 3, pp. 432–440, 2002. doi: 10.1016/S0304-8853(02)00334-7.

[101] J. Liu, M. Walmer, "Process and magnetic properties of rare-earth bonded magnets," in *Handbook of Advanced Magnetic Materials*, Y. Liu, D. J. Sellmyer, and D. Shindo, Eds., Boston, MA: Springer US, 2006, pp. 1008–1044. doi: 10.1007/1-4020-7984-2_24.

[102] D. Rahmatabadi, I. Ghasemi, M. Baniassadi, K. Abrinia, and M. Baghani, "3D printing of PLA-TPU with different component ratios: Fracture toughness, mechanical properties, and morphology," *J. Mater. Res. Technol.*, vol. 21, pp. 3970–3981, Nov. 2022. doi: 10.1016/j.jmrt.2022.11.024.

[103] M. Moradi, A. Aminzadeh, D. Rahmatabadi, and A. Hakimi, "Experimental investigation on mechanical characterization of 3D printed PLA produced by fused deposition modeling (FDM)," *Mater. Res. Express*, vol. 8, no. 3, p. 035304, 2021.

[104] M. Moradi, A. Aminzadeh, D. Rahmatabadi, and S. A. Rasouli, "Statistical and experimental analysis of process parameters of 3D nylon printed parts

by fused deposition modeling: Response surface modeling and optimization," *J. Mater. Eng. Perform.*, vol. 30, no. 7, pp. 5441–5454, 2021.

[105] C. Huber et al., "3D print of polymer bonded rare-earth magnets, and 3D magnetic field scanning with an end-user 3D printer," *Appl. Phys. Lett.*, vol. 109, no. 16, Oct. 2016. doi: 10.1063/1.4964856.

[106] E. M. Palmero et al., "Magnetic-polymer composites for bonding and 3D printing of permanent magnets," *IEEE Trans. Magn.*, vol. 55, no. 2, Feb. 2019. doi: 10.1109/TMAG.2018.2863560.

[107] A. Shen, X. Peng, C. P. Bailey, S. Dardona, and A. W. K. Ma, "3D printing of polymer-bonded magnets from highly concentrated, plate-like particle suspensions," *Mater. Des.*, vol. 183, p. 108133, Dec. 2019. doi: 10.1016/J.MATDES.2019.108133.

[108] B. M. Ma, J. W. Herchenroeder, B. Smith, M. Suda, D. Brown, and Z. Chen, "Recent development in bonded NdFeB magnets," *J. Magn. Magn. Mater.*, vol. 239, no. 1–3, pp. 418–423, Feb. 2002. doi: 10.1016/S0304-8853(01)00609-6.

[109] Y. L. Fan and K. S. Hwang, "Properties of metal injection molded products using titanate-containing binders," *Mater. Trans.*, vol. 48, no. 3, pp. 544–549, Mar. 2007. doi: 10.2320/matertrans.48.544.

[110] S. S. M. Nor, M. M. Rahman, F. Tarlochan, B. Shahida, and A. K. Ariffin, "The effect of lubrication in reducing net friction in warm powder compaction process," *J. Mater. Process. Technol.*, vol. 207, no. 1–3, pp. 118–124, Oct. 2008. doi: 10.1016/J.JMATPROTEC.2007.12.081.

[111] A. Xenopoulos and B. Wunderlich, "Thermodynamic properties of liquid and semicrystalline linear aliphatic polyamides," *J. Polym. Sci. B Polym. Phys.*, vol. 28, no. 12, pp. 2271–2290, Nov. 1990. doi: 10.1002/polb.1990.090281209.

[112] ASTM, *Standard Test Method for Evaluating Hygrothermal Corrosion Resistance of Permanent Magnet Alloys*, ASTM A1071/A1071M-11, 2015.

[113] IEC, *Environmental testing—Part 2: Tests—Test Z/AD: Composite temperature/humidity cyclic test (IEC 60068-2-38:2009)*, 2009.

[114] M. Leonowicz, W. Kaszuwara, S. Wojciechowski, and H. A. Davies, "Irreversible losses of magnetisation in Fe-Nd-B type magnets," *J. Magn. Magn. Mater.*, vol. 157–158, pp. 45–46, May 1996. doi: 10.1016/0304-8853(95)01128-5.

[115] J. Ormerod, A. Karati, A. P. S. Baghel, D. Prodius, and I. C. Nlebedim, "Sourcing, refining and recycling of rare-earth magnets," *Sustainability*, vol. 15, no. 20, p. 14901, Oct. 2023. doi: 10.3390/su152014901.

[116] S. Massari and M. Ruberti, "Rare earth elements as critical raw materials: Focus on international markets and future strategies," *Resour. Policy*, vol. 38, no. 1, pp. 36–43, Mar. 2013. doi: 10.1016/j.resourpol.2012.07.001.

[117] C. Huber, G. Mitteramskogler, M. Goertler, I. Teliban, M. Groenefeld, and D. Suess, "Additive manufactured polymer-bonded isotropic NdFeVB magnets by stereolithography and their comparison to fused filament

fabricated and selective laser sintered magnets," *Materials*, vol. 13, no. 8, Apr. 2020, doi: 10.3390/MA13081916.

[118] L. Pigliaru, L. Paleari, M. Bragaglia, F. Nanni, T. Ghidini, and M. Rinaldi, "Poly-ether-ether-ketone – Neodymium-iron-boron bonded permanent magnets via fused filament fabrication," *Synth. Met.*, vol. 279, Sep. 2021. doi: 10.1016/j.synthmet.2021.116857.

[119] A. Damnjanović, I. Milošev, and N. Kovačević, "Enhanced mechanical properties and environmental stability of polymer bonded magnets using three-step surface wet chemical modifications of Nd–Fe–B magnetic powder," *Heliyon*, vol. 10, no. 2, p. e26024, Feb. 2024. doi: 10.1016/j.heliyon.2024.e26024.

[120] C. Arpagaus, "Plasma treatment of polymer powders—from laboratory research to industrial application," *Plasma Process. Polym.*, vol. 15, no. 9, Sep. 2018. doi: 10.1002/ppap.201800133.

[121] A. Vesel, G. Primc, R. Zaplotnik, and M. Mozetič, "Applications of highly non-equilibrium low-pressure oxygen plasma for treatment of polymers and polymer composites on an industrial scale," *Plasma Phys. Control. Fusion*, vol. 62, no. 2, 2020. doi: 10.1088/1361-6587/ab5b50.

[122] H. Šourková and P. Špatenka, "Plasma activation of polyethylene powder," *Polymers (Basel)*, vol. 12, no. 9, Sep. 2020. doi: 10.3390/POLYM12092099.

[123] Evonik, "VESTOSINT®1111 Natural Color," 2011. [Online]. Available: https://www.vestosint.com/en/polyamide-12-nylonpowders/product-overview-vestosint-polyamide-12-nylon-powders-141941.html . [Accessed: Mar. 10, 2021].

[124] H. J. Šourková, Z. Weberová, J. Antoň, and P. Špatenka, "Wettability and adhesion of polyethylene powder treated with non-equilibrium various gaseous plasma in semi-industrial equipment," *Materials*, vol. 15, no. 2, Jan. 2022. doi: 10.3390/ma15020686.

[125] H. Šourková, G. Primc, and P. Špatenka, "Surface functionalization of polyethylene granules by treatment with low-pressure air plasma," *Materials*, vol. 11, no. 6, May 2018. doi: 10.3390/ma11060885.

[126] A. Vesel and M. Mozetič, "Low-pressure plasma-assisted polymer surface modifications," in *Printing on Polymers: Fundamentals and Applications*, Elsevier Inc., 2015, pp. 101–121. doi: 10.1016/B978-0-323-37468-2.00007-5.

[127] G. Primc, "Surface modification of polyamides by gaseous plasma—Review and scientific challenges," *Polymers*, vol. 12, no. 12, Dec. 2020. doi: 10.3390/polym12123020.

[128] S. J. Monte, "Titanate coupling agents," in *Functional Fillers for Plastics*, 2010, pp. 91–114.

[129] A. Y. Al-maharma, "Effects of porosity on the mechanical properties of additively manufactured components: A critical review," *Results Mater.*, vol. 4, no. 2, 2020.

[130] S. Wang, L. Capoen, D. R. D'hooge, and L. Cardon, "Can the melt flow index be used to predict the success of fused deposition modelling of commercial

poly (lactic acid) filaments into 3D printed materials?," *Plast. Rubber Compos.*, vol. 47, no. 1, pp. 9–16, 2018.

[131] T. N. A. T. Rahim, A. M. Abdullah, H. M. Akil, D. Mohamad, and Z. A. Rajion, "The improvement of mechanical and thermal properties of polyamide 12 3D printed parts by fused deposition modelling," *Express Polym. Lett.*, vol. 11, no. 12, pp. 963–982, Dec. 2017. doi: 10.3144/expresspolymlett.2017.92.

Bibliography

Publications Related to the Thesis

Journal Articles

Damnjanović, A., & Kovačević, N. (2023). Influence of magnet particle shape on magnetic and environmental stability of FDM polymer-bonded magnets. Materials, 16(8), 2993.

Damnjanović, A., Milošev, I., & Kovačević, N. (2024). Enhanced mechanical properties and environmental stability of polymer bonded magnets using three-step surface wet chemical modifications of Nd–Fe–B magnetic powder. Heliyon.

Damnjanović, A., Primc, G., Zaplotnik, R., Mozetič, M., & Kovačević, N. (2024). The Impact of Plasma Surface Treatments on the Mechanical Properties and Magnetic Performance of FDM-Printed NdFeB/PA12 Magnets. Materials, 17(10), 2275.

Biography

Ana Damnjanović holds a Bachelor's degree in Inorganic Technology from the Technical Faculty Bor, University of Belgrade, Serbia, which she completed in 2012. She was later awarded the prestigious European Commission Erasmus Mundus scholarship to pursue her International Master of Science in Environmental Technology and Engineering (IMETE), graduating in 2018. Her Master's program, conducted at three leading European universities (Ghent University, IHE Delft, and the University of Chemistry and Technology, Prague), focused on environmental technologies, specifically wastewater treatment.

Professionally, Ana has held positions as Technology and Product Safety Manager at a mineral water plant, ensuring compliance with HACCP and other safety standards, and as Head of Quality Control at a calcite mineral processing factory. She transitioned into research as an Early Career Researcher at Kolektor Mobility, where she worked on the EU project MaMi, focusing on polymer-bonded magnets based on Nd–Fe–B. Her research in optimizing surface treatments and enhancing adhesion properties led to the publication of three peer-reviewed scientific articles, where Ana served as the main author.

Author's Contribution to the Publications

I Writing – original draft, Validation, Methodology, Investigation, Formal analysis, Conceptualisation.

II Conceptualisation, methodology, validation, formal analysis, investigation, resources, data curation, writing – original draft preparation, visualisation.

III Conceptualisation, methodology, validation, formal analysis, investigation, writing – original draft preparation.

Permissions